Thesis

Oriented Magnetic Field Effects
in Quasi Two-Dimensional Superconductors

Graduate School of Science, Kyoto University
Eiji Ohmichi

January 20, 2000

Contents

4 Angle-Dependent Galvanomagnetic Effects and Quantum Oscillations

Chapter 1

Introduction

1.1 Effect of magnetic fields on electrons in metals

Electrons in metals are affected by a magnetic field. According to a semi-classical theory, the electronic state specified by a wave number vector $\boldsymbol{k}$ in a magnetic field is governed by the following equation of motion [1],

$$\hbar\frac{d\boldsymbol{k}}{dt} = -\frac{e}{c_0}\boldsymbol{v} \times \boldsymbol{H}, \tag{1.1}$$

$$\boldsymbol{v} = \frac{1}{\hbar}\frac{\partial\epsilon(\boldsymbol{k})}{\partial\boldsymbol{k}}, \tag{1.2}$$

where e is the electric charge, c_0 is the light velocity, $\boldsymbol{v}$ is the velocity of the electron, $\boldsymbol{H}$ is a magnetic field, and $\epsilon(\boldsymbol{k})$ is the energy dispersion. The electrons traverse trajectories called cyclotron orbits on the plane perpendicular to the applied field, keeping the electron motion along the magnetic field unchanged. Transport properties of metals in a magnetic field can be treated by applying the Bloch-Boltzmann equation to the electrons in the vicinity of the Fermi surface (FS) [1].

According to eq. (1.1), provided that the orbital motion within the plane is isotropic, the electron forms a cyclotron orbit with a radius of $|\boldsymbol{r}| = (c_0\hbar|\boldsymbol{k}|/e)H^{-1}$. With increasing H, the orbit shrinks in proportion to H^{-1}. This relation indicates that the electron motion is strongly directed in

4

the field direction in a high magnetic field, resulting in low-dimensionalization of the electron motion.

Meanwhile, in a strong magnetic field at low temperature, the semiclassical description is not satisfactory due to quantization of the electronic states. Due to the Sommerfeld quantization rule for periodic motion of an electron in the cyclotron orbit, the energy dispersion is discretized into Landau levels so that the electron motion in the plane perpendicular to the field direction is quantized keeping the electron dynamics in the direction parallel to the magnetic field unchanged. Such quantization leads to quantum oscillations in physical valuables as a function of an inverse magnetic field. Quantum oscillations in the magnetization and in the resistivity caused in this way are called de Haas-van Alphen (dHvA) and Shubnikov-de Haas (SdH) oscillations, respectively. The oscillation frequencies are connected to the FS extremal areas enclosed by corresponding cyclotron orbits.

1.2 Effect of magnetic fields on superconductivity

One of important effects of a magnetic field on superconductivity is a depairing effect of Cooper pairs into quasiparticles. According to the Bardeen-Cooper-Schrieffer (BCS) theory, two electrons with electronic states $(\boldsymbol{k}, \uparrow)$, $(-\boldsymbol{k}, \downarrow)$ are coupled to form a Cooper pair with spin singlet state. When a magnetic field is applied to superconductors, it works to prevent formation of Cooper pairs, affecting both orbital motion and spin.

Concerning the effect on the orbital motion, the electronic states $(\boldsymbol{k}, \uparrow)$, $(-\boldsymbol{k}, \downarrow)$ are forced to be shifted to $(\boldsymbol{k}-(e/c_0)\boldsymbol{A}, \uparrow)$, $(-\boldsymbol{k}+(e/c_0)\boldsymbol{A}, \downarrow)$ in a magnetic field $\boldsymbol{H}=\nabla\times\boldsymbol{A}$, respectively. Such displacement evidently works to destabilize Cooper pairs. By solving the linealized Ginzburg-Landau (GL)

equation,

$$\left(\frac{\nabla}{i} - \frac{2\pi \boldsymbol{A}}{\Phi_0}\right)^2 \psi = \frac{1}{\xi^2(T)}\psi, \tag{1.3}$$

the upper critical field by the orbital depairing effect, H_{c2}^{orb}, is obtained as

$$H_{c2}^{\text{orb}} = \frac{\Phi_0}{2\pi\xi^2(T)}, \tag{1.4}$$

where Φ_0 is the flux quantum and $\xi(T)$ is the coherence length of Cooper pairs.

On the other hand, total energy of the system in a magnetic field can be lowered with spin polarization of electrons, leading to the so-called Clogston-Chandrasekhar limit, or Pauli paramagnetic limit H_P [2, 3]. Provided that spin polarization is considered, superconductivity is destroyed when the polarization energy becomes equal to the condensation energy, that is,

$$\frac{1}{2}(\chi_n - \chi_s)H_P^2(T) = \frac{1}{8\pi}H_c^2(T), \tag{1.5}$$

where χ_n and χ_s are spin susceptibility in the normal and superconducting states, respectively, and H_c is the thermodynamic critical filed. For a simple BCS case, H_P at zero temperature,

$$H_P(0) = \frac{\sqrt{2}\Delta_0}{g\mu_B}, \tag{1.6}$$

is easily obtained where Δ_0 is the gap amplitude at zero temperature, g is the spin splitting factor, and μ_B is the Bohr magneton. With $g=2$ for free electrons, a convenient expression $\mu_0 H_P=1.84\ T_c$ ($\mu_0 H_P$ and T_c are given in a unit of Tesla and Kelvin, respectively) is derived to compare with an observed upper critical field H_{c2}.

In real materials, the observed H_{c2} is a result of both the spin effect and the orbital effect. Relative strength of these two depairing effects at zero temperature is evaluated by the following relation,

$$\frac{H_{c2}^{\text{orb}}}{H_P} \sim 1.05 \cdot \frac{g}{2} \cdot \frac{m^*}{m_0} \cdot \frac{1}{p_F\xi_0}, \tag{1.7}$$

where m^* is the effective mass, m_0 is the free electron mass, p_F is the Fermi momentum, and ξ_0 is the BCS coherence length. Since $\xi_0 \gg p_F^{-1} \sim a$ (a : lattice parameter) for usual superconductors, the orbital depairing effect is dominant ($H_P \gg H_{c2}^{orb}$).

1.3 Effect of oriented magnetic fields

Materials studied in this thesis are quasi two-dimensional (Q2D) supercon-ductors with a layered structure. The carriers in these materials can move rather freely within the conducting plane, while they have less conductivity in the inter-plane direction due to the insulating layers between the conduct-ing layers. As a result, the electronic structure becomes highly anisotropic. Typically, the FS of Q2D electronic systems is represented by a cylindrical FS with slight warping along the cylindrical axis for the simplest case, in contrast to a spherical one for three-dimensional (3D) case.

It should be noted that the effects of magnetic fields presented in Sec-tion 1.1 and 1.2 are based upon isotropic 3D cases. Thus, it is interesting to consider how the effect of magnetic fields can be modified in Q2D elec-tronic systems. In the following, examples of the interplay between magnetic fields and Q2D electronic systems are shown, paying attention to the low-dimensional structure. In contrast to the 3D case, significant roles of the field orientation in Q2D electronic systems are stressed.

In the normal state, it should be noted that cyclotron motion in Q2D electronic systems dramatically changes depending on the field orientation. When the field is applied along the cylindrical axis, all the cyclotron orbits are closed, similar to the 3D case. With field inclination toward the in-plane direction, however, there exist magic angles known as Yamaji angles, where the cross-sectional area of all the cyclotron orbits are identical. This fact indi-cates that the system can be regarded as pure 2D. Such dimensional crossover

from Q2D to 2D FS is known to give angle-dependent magnetoresistance oscillations (AMRO) [4, 5] or colossal quantum oscillations at Yamaji angles. Meanwhile, in the vicinity of the in-plane field orientation, there appear open orbits elongated along the axis, with the carriers moving back and forth in the inter-plane direction in the real space. In a strong magnetic field so that the amplitude of the carrier motion becomes less than the distance between adjacent layers, the carrier motion will be confined within the conducting plane, and coherence between conducting layers will be lost. As a result, the system can be regarded as a stack of 2D conducting sheets. These situation distinctly differs from the 3D case, in which all the cyclotron orbits are closed and rather insensitive with regard to the variation in field orientation.

In the superconducting state, attention should be paid to the relative strength of depairing effects represented by eq. (1.7). The spin depairing effect is rather isotropic, while the orbital depairing effect is highly anisotropic due to the large effective mass ratio. As a result, although $H_P \gg H_{c2}^{orb}$ is met for usual 3D superconductors, $H_P \leq H_{c2}^{orb}$ can be reached for Q2D superconductors under in-plane magnetic fields due to the large effective mass in the inter-plane direction. This relation indicates that the orbital effect is strongly suppressed in the field configuration and the spin depairing effect starts to play an essential role in H_{c2}. In such Pauli-limited situation, a new superconducting state called the Fulde-Ferrell-Larkin-Ovchinikov (FFLO) state [6, 7] with a spatially modulated order parameter has been theoretically proposed.

Another important effect of in-plane magnetic fields is proposed, especially for triplet Q2D superconductors free from the Pauli limit. Strong in-plane fields work to confine and to localize the orbital motion within the conducting plane. As a result, Cooper pairs formed in such situation are localized within the conducting plane and hence are no longer destroyed by the diamagnetic currents relevant to the orbital depairing effect. This

remarkable effect may bring about the restoration of superconductivity in Q2D superconductor under strong in-plane magnetic fields [8].

1.4　Purpose and scope of this thesis

In this thesis, the author has taken up Q2D organic superconductors and the Q2D oxide superconductor Sr_2RuO_4. In addition to the two-dimensionality, both materials possess common features advantageous to measurements: first, the quality of the crystals are extremely high enough for the demonstration of clear quantum oscillations. Research of the intrinsic nature is possible by using only such high quality samples. Second, the superconducting transition temperature T_c is rather low, typically less than 10 K. The magnetic field required for measurements can be lowered to a field range accessible by a static magnetic field due to the low T_c. These two features are quite contrary to high-T_c superconductors realized by carrier doping.

Therefore, these Q2D materials provide an ideal opportunity to investigate the phenomena presented in the previous section. These phenomena can be called as oriented magnetic field effects, since the role of the field orientation is essential for the appearance. In this thesis, the author presents a set of experimental evidence for oriented magnetic field effects in Q2D electronic systems, paying attention to the following points.

The present study covers both the normal state and the superconducting state of Q2D superconductors. In the normal state, the author has paid attention to the dimensional crossover caused by the field inclination. Angle-dependent galvanomagnetic effects and quantum oscillations in Q2D superconductors are purposed in the chapter. In particular, those techniques were applied to Sr_2RuO_4 as the first attempt in layered oxide conductors. Much more detailed analysis became possible compared to the case in organic conductors, since a number of known band parameters through the previous

works were available.

In the superconducting state, the author has paid attention to the suppression of the orbital depairing effect leading to a dominant role of the spin effect. This motivated us to carry out experimental attempts to search for the new superconducting states in strong in-plane magnetic fields.

There have been many experimental reports of Q2D electronic systems in magnetic fields so far. In most cases, however, the field orientation can be regarded as one of parameters to derive the anisotropy of the system, and experimental studies in the viewpoint of novel electronic states realized in particular field directions are lacking. In this sense, the present study is distinct from those previous works.

It should be also noted that experimental devices that allowed us to control the field orientation were indispensable in this study. Therefore, the significance of the technical development of rotators in this study should be stressed. In fact, resolution of the order of $0.01°$ was required in the experiments of superconductivity recurrence. To our knowledge, there have been no other examples in which so much attention was paid to the field orientation as the present study.

The construction of this thesis is as follows: Chapter 2 provides theoretical descriptions of AMRO and quantum oscillations. Chapter 3 describes experimental methods and techniques. In Chapter 4, angle-dependent galvanomagnetic effects and quantum oscillations in the normal state are presented. Firstly, AMRO study of Sr_2RuO_4 are shown to derive the FS contour in Section 4.1, and then the effect of chemical potential on quantum oscillations in Sr_2RuO_4 is discussed based upon the temperature and angle dependence of the oscillations with the sum and difference frequencies in Section 4.2. With regard to a resistance peak in Sr_2RuO_4 observed under in-plane magnetic fields, the anisotropic behavior is discussed together with the transverse

magnetoresistance in Section 4.3. Based upon the anomalous angle dependence of quantum oscillations in κ-(BEDT-TTF)$_2$Cu$_2$(CN)$_3$, the existence of a 3D FS is discussed in Section 4.4. In chapter 5, superconductivity of Q2D superconductors under in-plane magnetic fields are studied. The results of anomalous high H_{c2} in κ-(BEDT-TTF)$_4$Hg$_{2.89}$Br$_8$ (Section 5.1) and the search for superconductivity recurrence in Sr$_2$RuO$_4$ (Section 5.2) are shown. The implication of experimental results are discussed. Finally, a summary is given in Chapter 6.

1.5 Materials and their Fermi surfaces studied in this thesis

The materials studied in this this are briefly described here. They are categorized into two groups : (1) BEDT-TTF based organic superconductors and (2) the oxide superconductor Sr$_2$RuO$_4$, both of which are of a layered structure possessing two-dimensional character.

1.5.1 BEDT-TTF based organic conductors

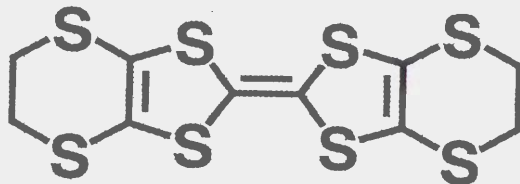Figure 1.1: BEDT-TTF molecule

BEDT-TTF (bisethylenedithia-tetrathiafulvalene, C$_{10}$H$_8$S$_8$) (Fig. 1.1) is an organic molecule giving the highest T_c among organic superconductors [9, 10]. BEDT-TTF molecules form a family of charge transfer complexes (BEDT-TTF)$_m$X$_n$ with an anion X. Typical chemical formula is (BEDT-TTF)$_2X$, in which the valence of BEDT-TTF molecule is formally +0.5, that

is, the highest occupied molecular orbital (HOMO) is 3/4-filled. An anion X can take several types of the shape such as linear and polymeric one.

BEDT-TTF molecules are condensed by van der Waals force so that they construct a 2D network of the conducting plane sandwiched by layers consisting of the anion X. Therefore, the electronic states of organic conductors are quite anisotropic and low-dimensional. Among them, the BEDT-TTF salts studied in this thesis are the so-called κ-type salts, κ-(BEDT-TTF)$_2$Cu$_2$(CN)$_3$ [11, 12], κ-(BEDT-TTF)$_2$Cu(NCS)$_2$ [13], and κ-(BEDT-TTF)$_4$Hg$_{2.89}$Br$_8$ [14]. The crystal structure of these salts are illustrated in Figs. 1.2-1.4, in which BEDT-TTF molecules are packed as a checker-flag pattern yielding rather two-dimensionality within the conducting plane. Polymeric anions Cu$_2$(CN)$_3^-$, and Cu(NCS)$_2^-$ form a 2D network and 1D chain of the anion layer, respectively, while Hg$_{2.89}$Br$_8^{2-}$ anion exhibits incommensurate periodicity to BEDT-TTF stacking, leading to two supperlattices with different lattice parameters for κ-(BEDT-TTF)$_4$Hg$_{2.89}$Br$_8$.

Band structure of organic conductors is usually calculated by the extended Hückel tight binding method, whose validity has been confirmed by quantum oscillations and AMRO [17]. In Fig. 1.5, the cross-section of the FS of κ-(BEDT-TTF)$_2$Cu$_2$(CN)$_3$ [11, 18] and κ-(BEDT-TTF)$_2$Cu(NCS)$_2$ [19, 20, 21, 22] are illustrated. The FS consists of two parts: one-dimensional electron-like sheet along k_c direction and two-dimensional hole-like pocket α. The large closed orbit β connecting 1D and 2D sheets appears, when the carriers go across a tiny gap between them in a strong magnetic field. The calculated FS of κ-(BEDT-TTF)$_4$Hg$_{2.89}$Br$_8$ is not available at present.

The characteristics of these salts are summarized in Table 1.1. Although these three salts are of a similar structure, the conducting behavior is quite different: κ-(BEDT-TTF)$_2$Cu$_2$(CN)$_3$ is semiconducting at ambient pressure, and exhibits a nonmetal-metal transition, followed by a superconducting
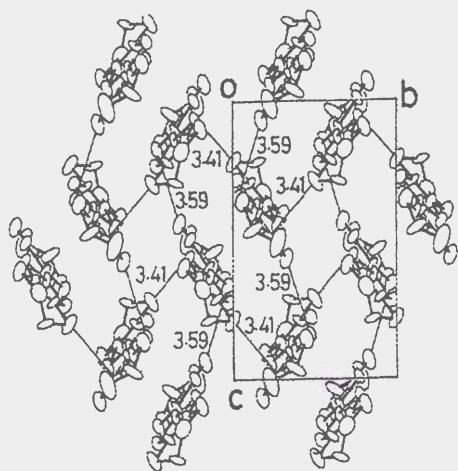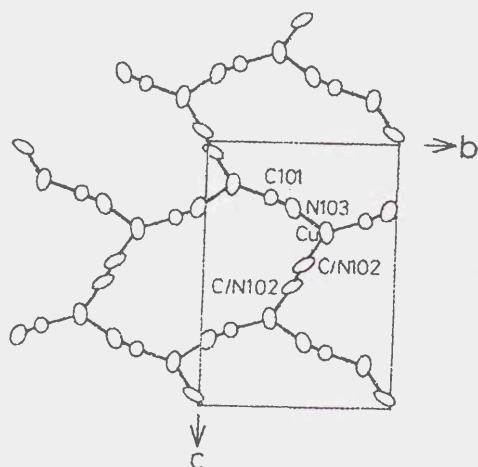
Figure 1.2: (a) BEDT-TTF layer and (b) $Cu_2(CN)_3$ layer of κ-(BEDT-TTF)$_2$Cu$_2$(CN)$_3$ viewed along the a^*-axis [12].
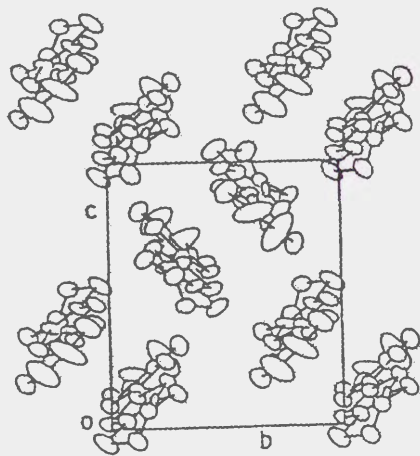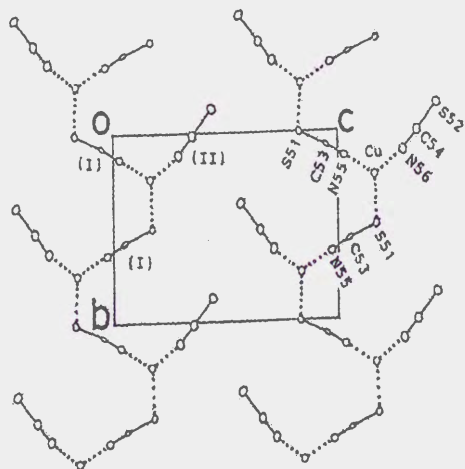
Figure 1.3: (a) BEDT-TTF layer and (b) $Cu(NCS)_2$ layer of κ-(BEDT-TTF)$_2$Cu(NCS)$_2$ viewed along the a^*-axis [15].
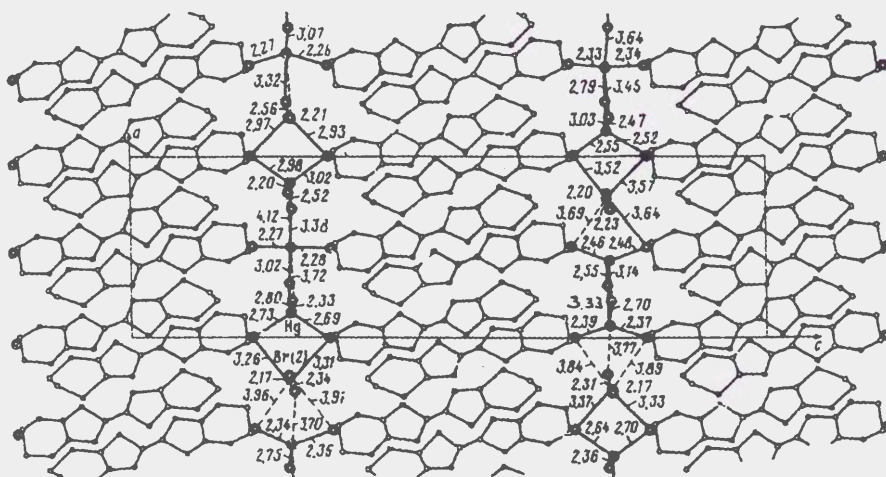
Figure 1.4: Crystal structure of κ-(BEDT-TTF)$_4$Hg$_{2.89}$Br$_8$ viewed along the b-axis [16]. The BEDT-TTF layers alternate with the anion layers ($\bullet$−Hg, $\circ$−Br).

(a)
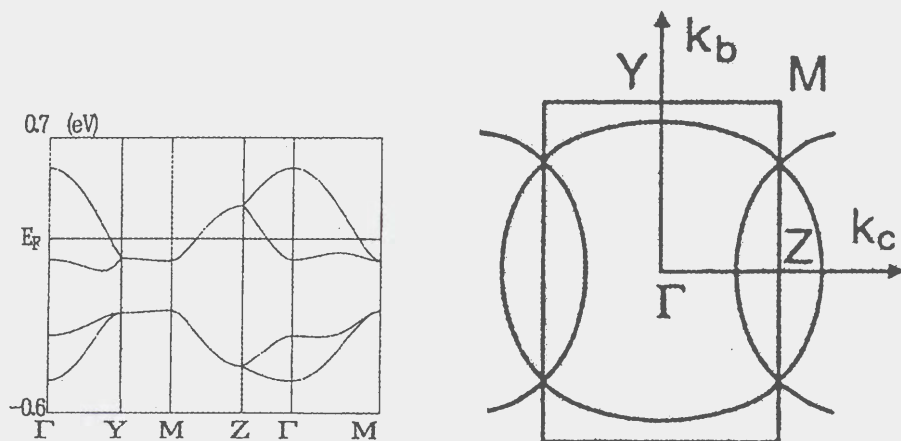
(b)
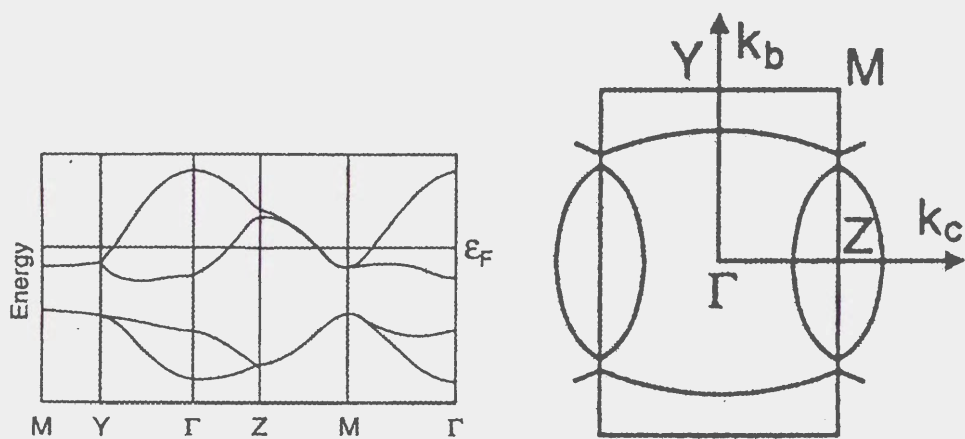
Figure 1.5: Band structure and Fermi surface of (a) κ-(BEDT-TTF)$_2$Cu$_2$(CN)$_3$ [18] and (b) κ-(BEDT-TTF)$_2$Cu(NCS)$_2$ [19] based upon the extended Hückel tight binding method.

	κ-(BEDT-TTF)$_2$Cu$_2$(CN)$_3$	κ-(BEDT-TTF)$_4$Hg$_{2.89}$Br$_8$ (Hg sublattice)	κ-(BEDT-TTF)$_2$Cu(NCS)$_2$
crystal structure	monoclinic	monoclinic	monoclinic
crystal symmetry	$P2_1/c$	$I2/c$ ($I2$)	$P2_1$
a (nm)	1.6117	1.1219 (0.3877)	1.6248
b (nm)	0.85858	0.8706 (0.8706)	0.8440
c (nm)	1.3397	3.7105 (3.7105)	1.3124
$\beta(°)$	113.42	90.97 (87.30)	110.30
$\rho(T)$ ($P{=}0$)	semiconducting	metallic	semiconducting ($T \geq 90$ K) metallic ($T \leq 90$ K)
T_c (K)	3.8 (0.6 kbar)	4.3	10.4
$-dT_c/dP$ (K/kbar)	2~3 [18]	~ -1 ($P \leq 2.5$ kbar) [23] ~ 0.1 ($P \geq 2.5$ kabr)	1.3~2 [24, 25]

Table 1.1: Crystal data and characteristics of the electrical conduction for κ-(BEDT-TTF)$_2$Cu$_2$(CN)$_3$, κ-(BEDT-TTF)$_4$Hg$_{2.89}$Br$_8$, and κ-(BEDT-TTF)$_2$Cu(NCS)$_2$.

transition under moderate pressure. The behavior of κ-(BEDT-TTF)$_2$Cu(NCS)$_2$ at ambient pressure is similar to that of κ-(BEDT-TTF)$_2$Cu$_2$(CN)$_3$ under pressure exhibiting a resistance hump at $\sim$90 K, but T_c of $\sim$10 K is much high than that of κ-(BEDT-TTF)$_2$Cu$_2$(CN)$_3$. κ-(BEDT-TTF)$_4$Hg$_{2.89}$Br$_8$ is metallic in the whole temperature region and undergoes a superconducting transition at $T_c \sim$4 K.

1.5.2   Sr$_2$RuO$_4$

As shown in Fig. 1.6, the crystal structure of Sr$_2$RuO$_4$, the first layered perovskite superconductor without copper [26], is of K$_2$NiF$_4$-type with tetragonal crystal symmetry represented by $I4/mmm$, similar to high-T_c cuprates La$_{2-x}$Sr$_x$CuO$_4$. The lattice parameters are a=0.386 nm and c=1.273 nm, and the inter-plane layer distance is $c/2$=0.64 nm. In Sr$_2$RuO$_4$, RuO$_2$ layers play a role of the conducting sheet, in contrast to high-T_c cuprates in which the CuO$_2$ plane is the highly conducting layer. The tetragonal symmetry is kept down to low temperatures, according to neutron diffraction experiments at low temperatures [27].

The band structure is calculated by local density approximation (LDA). The obtained FS [28, 29] shown in Fig. 1.7 consists of three nearly-cylinder, assigned as the α, β, and γ branches. All the FS branches have been experimentally observed by quantum oscillations [30, 31, 32]. The effective masses derived by quantum oscillations were by a factor of three enhanced than the calculated, indicating that Sr$_2$RuO$_4$ can be regarded as a strongly correlated electronic system. This is also suggested by the fact the sister compound Ca$_2$RuO$_4$ [33, 34] is a Mott insulator.

The electric resistivity shown in Fig. 1.8 is anisotropic reflecting the two-dimensionality of the crystal structure. The in-plane resistivity ρ_{ab} and the inter-plane resistivity ρ_c are $\sim$120 $\mu\Omega$cm and $\sim$40 mΩcm at room temper-
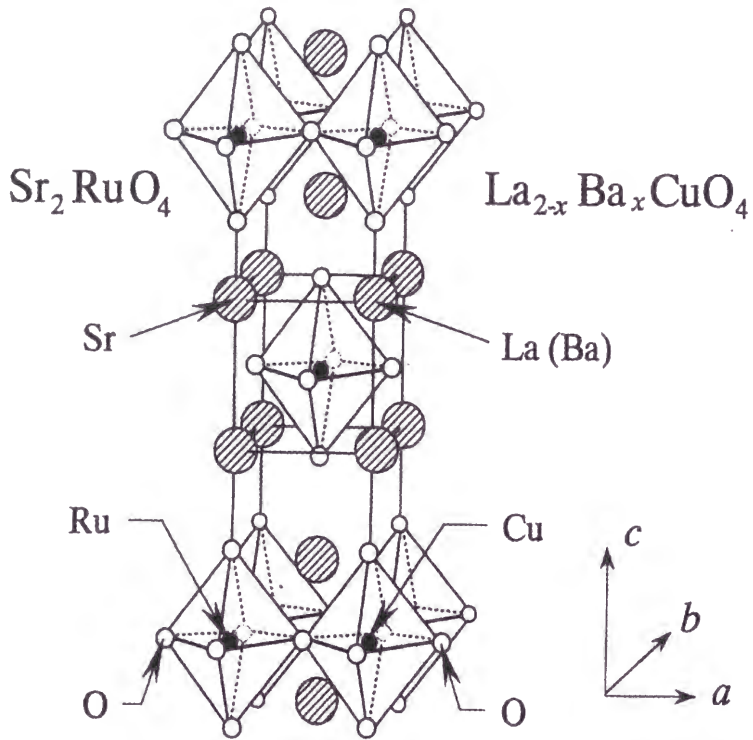
Figure 1.6: Crystal structure of the layered oxide superconductors Sr_2RuO_4 and $La_{2-x}Ba_xCuO_4$. The ab plane is parallel to the layers, while the c axis is perpendicular to the layers. Note that crystal structure of Sr_2RuO_4 is tetragonal with $a=b$.
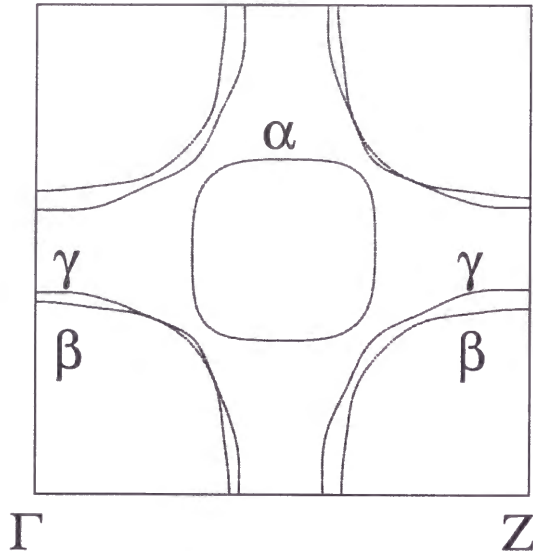
Figure 1.7: Calculated cross-section of the Fermi surface of Sr_2RuO_4 [28] in the plane normal to the k_z direction. Among the three nearly-cylindrical Fermi surface branches, the α branch is the hole pocket, while the β and γ branches are the electron pockets.
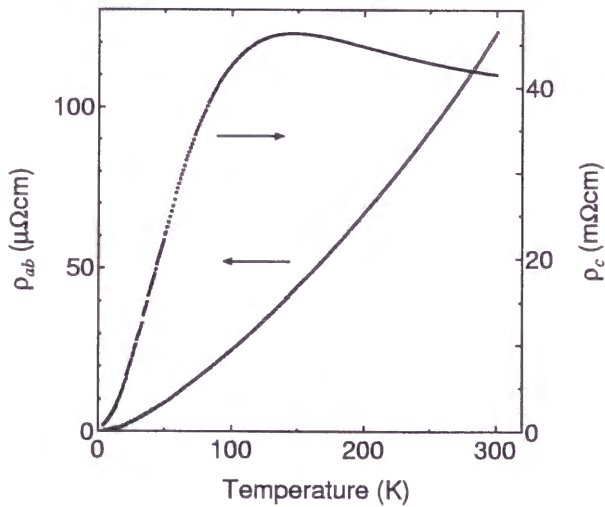
Figure 1.8: Temperature dependence of the in-plane resistivity ρ_{ab} and the inter-plane resistivity ρ_c. Note that ρ_c exhibits a hump around 130 K in contrast to ρ_{ab}.

ature, respectively. ρ_{ab} is metallic in the whole temperature region while ρ_c shows a resistance hump around 130 K. Below 20 K, both resistivities shows T^2-dependence with a constant ratio of $\rho_c/\rho_{ab} \simeq 1000$-4000, indicating anisotropic Fermi liquid nature of Sr_2RuO_4 below 20 K [35].

Concerning the superconductivity of Sr_2RuO_4, its intrinsic T_c is 1.5 K, rather low compared to high-T_c cuprates. Triplet superconducting symmetry of the Cooper pair is being confirmed by a number of experimental results such as nuclear magnetic resonance (NMR) measurements [36], impurity effects on superconductivity [37, 38], and a muon spin rotation (μSR) study [39]. This indicates that in Sr_2RuO_4, Cooper pairs are formed so that the total spin moment of a Cooper pair becomes $S=1$, in contrast to singlet pairing ($S=0$).

Chapter 2

Theories for Angle-Dependent Magnetoresistance Oscillations and Quantum Oscillations

2.1 Angle-dependent magnetoresistance oscillations (AMRO)

A remarkable phenomenon called angle-dependent magnetoresistance oscillation (AMRO) has been observed in organic conductors [4, 5]. This effect was first explained by Yamaji [40] on the basis of nearly cylindrical FS with slight warping and is found to be useful to get a diameter of Q2D FS.

The energy dispersion $\epsilon\,(\boldsymbol{k})$ for Q2D FS can be approximately represented by the following equation,

$$\epsilon(\boldsymbol{k}) = \frac{\hbar^2}{2m^*}(k_x^2 + k_y^2) - 2t_\perp \cos(dk_z), \qquad (2.1)$$

where m^* is the effective mass, $t_\perp$ ($\ll \epsilon_F$: the Fermi energy) is the inter-plane transfer energy, and d is the characteristic length relevant to the modulation of Q2D FS in the k_z direction.

In the presence of a magnetic field $\boldsymbol{H}$, each electronic state specified by wave number vector $\boldsymbol{k}$ in the reciprocal space is affected by the Lorenz force according to the following equation [1],

$$\hbar \frac{d\boldsymbol{k}}{dt} = -\frac{e}{c_0}\boldsymbol{v} \times \boldsymbol{H}, \qquad (2.2)$$

$$v = \frac{1}{\hbar}\frac{\partial\epsilon(\boldsymbol{k})}{\partial\boldsymbol{k}}. \tag{2.3}$$

Yamaji [40] calculated the cross-sectional area S_k enclosed by a cyclotron motion under a magnetic field tilted by θ from the direction perpendicular to the conducting plane and derived the following relation,

$$S_k \cos\theta = \pi k_{\mathrm{F}}^2 + 4\pi m^* t_\perp \cos(k_z^{(0)}d)J_0(dk_{\mathrm{F}}\tan\theta) + O(t_\perp^2), \tag{2.4}$$

where k_{F} is the Fermi wave number, $k_z^{(0)}$ is the intersection between the enclosed plane by the cyclotron motion and the k_z axis, and J_0 is the Bessel function of 0-th order. Due to three-dimensionality introduced by $t_\perp$, the second term appears. The higher order term $O(t_\perp^2)$ can be neglected because $t \ll \epsilon_{\mathrm{F}}$. Using the relation $J_0(z) \sim \sqrt{\frac{2}{\pi z}}\cos(z - \pi/4)$, the second term in eq. (2.4) becomes zero when

$$dk_{\mathrm{F}}\tan\theta_n = \pi\left(n - \frac{1}{4}\right) \ (n : \text{integer}). \tag{2.5}$$

This relation means that S_k is almost identical irrespective of $k_z^{(0)}$ and the system can be regarded as complete 2D at such angles θ_n, where the local resistance maxima are expected to appear in the angle dependence of the magnetoresistance. Although this scenario is based upon the topological consideration of the FS shape, experimental results with the $\tan\theta$ periodicity of the oscillations are explained.

The inter-plane conductivity tensor σ_{zz} was calculated by Yagi et $al.$ [41] based upon the Shockley tube integral [1] given by

$$\sigma_{zz} = \frac{e^2}{4\pi^3\hbar^2}\int_{-\frac{\pi}{d}}^{\frac{\pi}{d}} dk_z^{(0)}\left\{\frac{\cos\theta}{1 - e^{-2\pi/\omega_c\tau}}\int_0^{2\pi}d\varphi\int_0^{2\pi}d\varphi'\ v_z(\varphi)v_z(\varphi - \varphi')\frac{m^*}{\omega_c}e^{-\varphi'/\omega_c\tau}\right\}, \tag{2.6}$$

where ω_c $(=eH/m^*c_0)$ is the cyclotron frequency of each orbit, τ is the scattering time, φ, φ' are the phase variables of the closed orbit which increase

22
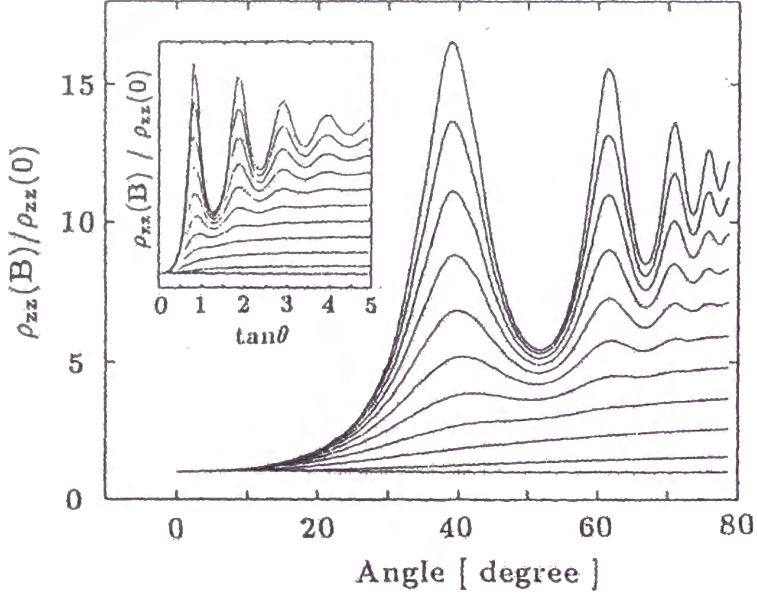
Figure 2.1: Calculated angle dependence of the zz component of the resistivity tensor, ρ_{zz}, for different magnetic fields with $t_\perp/\epsilon_F=1/100$ and $m^*t_\perp d^2/\hbar^2=0.045$ [41]. From bottom to top, the value of $\omega_c\tau$ varies from 0 to 4 with an increment of 0.4. The inset shows the replot against $\tan\theta$.

by 2π in completing each cyclotron motion.

The inter-plane conductivity tensor σ_{zz} is analytically derived from eq. (2.6) as

$$\sigma_{zz} = \sigma_{zz}^0 \left\{ J_0^2(dk_F \tan\theta) + 2\sum_{\nu=1}^{\infty} \frac{J_\nu^2(dk_F \tan\theta)}{1 + (\omega_c\tau\nu\cos\theta)^2} \right\}, \qquad (2.7)$$

where J_ν is the Bessel function of ν-th order, and

$$\sigma_{zz}^0 = \frac{2e^2 m^* t_\perp^2 d\tau}{\pi\hbar^4}. \qquad (2.8)$$

Figure 2.1 demonstrates that the above result reproduces whole angle dependence of the magnetoresistance except for the region near $\theta=90°$

The physical meaning of the above calculation is as follows. The averaged

velocity over a closed orbit, $\bar{v}_z$, is calculated as

$$\bar{v}_z = \oint v_z d\varphi = \frac{2t_\perp d}{\hbar} J_0(dk_\mathrm{F} \tan\theta) \sin(dk_z^{(0)}) \tag{2.9}$$

where

$$v_z = \frac{1}{\hbar}\frac{\partial\epsilon}{\partial k_z} = \frac{2t_\perp d}{\hbar}\sin(dk_z). \tag{2.10}$$

At the angles satisfying eq. (2.5), the value of $\bar{v}_z$ becomes zero for all the cyclotron orbits and hence the magnetoresistance exhibits a local resistance maximum at such angles as a result of dimensional crossover from Q2D to 2D. This is consistent with the invariance of the peak positions irrespective of the applied field strength.

2.2 Landau quantization and quantum oscillations

In a strong magnetic field, quantization of the electronic states becomes significant. This effect induces an oscillatory phenomenon in physical valuables as a function of an inverse magnetic field $1/H$ [42]. Here, the origin of the oscillations and its relevance to the FS properties are briefly described.

Similar to the Bohr-Sommerfeld correspondence principle, the electron momentum $\boldsymbol{p}$ in a magnetic field is quantized as

$$\oint \boldsymbol{p} d\boldsymbol{q} = (n+\gamma)2\pi\hbar, \tag{2.11}$$

where n is a positive integer, γ is a phase constant, typically $1/2$ for free electrons, and

$$\boldsymbol{p} = \left(\hbar\boldsymbol{k} - \frac{\hbar e}{c_0}\boldsymbol{A}\right). \tag{2.12}$$

From eq. (2.11), it is shown that magnetic flux Φ in the area enclosed by a cyclotron orbit is quantized as

$$\Phi = H a_n = (n+\gamma)\frac{2\pi\hbar c_0}{e}, \tag{2.13}$$

where a_n is the enclosed area by a cyclotron orbit in the real space. Since the area in the real space, a_n, is converted to the area in the reciprocal space, S_n, by multiplying a scaling factor $(eH/c_0\hbar)^2$, the Onsager relation [43] is derived as

$$S_n = (n + \gamma)\frac{2\pi e}{c_0 \hbar}H. \tag{2.14}$$

Evidently this relation restricts the permissible value of S_n in the reciprocal space, and hence $\boldsymbol{k}$ values in a magnetic field, resulting in quantization of the energy of the electrons. With use of the relation,

$$(\Delta\epsilon)_{\Delta n=1} = \left(\frac{\partial \epsilon}{\partial S}\right)(\Delta S)_{\Delta n=1} = \hbar\omega_c, \tag{2.15}$$

the energy levels are represented as

$$\epsilon = \left(n + \frac{1}{2}\right)\hbar\omega_c + \frac{\hbar^2}{2m_\parallel^*}k_\parallel^2, \tag{2.16}$$

where the symbol $\parallel$ indicates the component parallel to $\boldsymbol{H}$, and γ is assumed to be 1/2 [44].

Given that n-th Landau level crosses the FS at a certain field value H_n, the following relation,

$$S_{\mathrm{F}}\left(\frac{1}{H_{n+1}} - \frac{1}{H_n}\right) = \frac{2\pi e}{c_0 \hbar}, \tag{2.17}$$

is derived from eq. (2.14) where S_{F} is the cross-sectional area of the FS. This relation indicates that Landau levels traverses the FS by a certain increment of $1/H$. Such periodicity causes oscillatory phenomena in physical valuables as a function of $1/H$. These oscillations are called quantum oscillations and the oscillation frequency F is combined with the FS cross-sectional area S_{F} by the relation,

$$F = \frac{1}{\Delta\left(\frac{1}{H}\right)} = \frac{c_0 \hbar}{2\pi e}S_{\mathrm{F}}. \tag{2.18}$$

In particular, quantum oscillations in the thermodynamic quantities are called de Haas-van Alphen (dHvA) oscillations, while the oscillations in the resistivity are called Shubnikov-de Haas (SdH) oscillations. Note that the experimentally observed oscillations are associated with the extremal cross-sectional area of the FS as mentioned in the next section.

For the observation of quantum oscillations, Landau levels should be clearly separated without being smeared out by temperature or impurities: the spacing between adjacent Landau levels $\hbar\omega_c$ must be greater than energy uncertainty of $k_{\mathrm{B}}T$ or $\hbar/\tau$.

2.3 Lifshitz-Kosevich (LK) formula

The analytical treatment of quantum oscillations was made by Landau and Lifshitz [45]. According to them, the calculated grandcanonical potential $\tilde{\Omega}$ at $T=0$ without any damping effect, assuming a parabolic energy dispersion, is given by

$$\tilde{\Omega} = \left(\frac{eH}{c_0}\right)^{5/2} \frac{V}{4\pi^4 m^* \hbar^{1/2}} \sum_{p=1}^{\infty} \frac{1}{p^{5/2}} \cos\left[2\pi p\left(\frac{F}{H} - \frac{1}{2}\right) - \frac{\pi}{4}\right], \qquad (2.19)$$

where V is the total volume of the sample. This relation is obtained by integrating the contributions from thin 2D slabs, in which process, only the contribution from the closed orbit with an extremal area remains to be non-zero. Therefore, F in eq. (2.19) represents the oscillation frequency corresponding to such an orbit.

The magnetic moment $\tilde{M}$ is obtained by the field differentiation of $\tilde{\Omega}$ for a constant chemical potential μ as

$$\tilde{M} = -(\nabla_H \tilde{\Omega})_\mu, \qquad (2.20)$$

or

$$\tilde{M}_{\parallel} = -\left(\frac{\partial \tilde{\Omega}}{\partial H}\right)_{\mu}, \tag{2.21}$$

$$\tilde{M}_{\perp} = -\frac{1}{H}\left(\frac{\partial \tilde{\Omega}}{\partial \theta}\right)_{\mu,H} = -\frac{1}{F}\frac{\partial F}{\partial \theta}\tilde{M}_{\parallel}. \tag{2.22}$$

$\tilde{M}_{\parallel}$ is the longitudinal component of $\tilde{\boldsymbol{M}}$ while $\tilde{M}_{\perp}$ is the transverse component which is relevant to torque measurements. Here the analytical formula for $\tilde{M}_{\parallel}$ [42, 45] is given by

$$\tilde{M}_{\parallel} = -\frac{3}{2^{5/2}\pi}N_0\beta_0\left(\frac{H}{F}\right)^{1/2}\left\{\sum_{p=1}^{\infty}\frac{R_T R_D R_S}{p^{3/2}}\sin\left[2\pi p\left(\frac{F}{H}-\frac{1}{2}\right)-\frac{\pi}{4}\right]\right\}, \tag{2.23}$$

where $\beta_0 = e\hbar/m^*c_0$, $N_0 = (V/3\pi^2)(2m^*\mu/\hbar^2)^{3/2}$, p denotes p-th harmonics of the fundamental frequency, and R_T, R_D, R_S are damping factors associated with temperature, impurity, and spin, respectively.

Here, the damping factors are given as

$$R_T = \frac{2\pi^2 p k_B T/\beta_0 H}{\sinh(2\pi^2 p k_B T/\beta_0 H)}, \tag{2.24}$$

$$R_D = \exp(-2\pi^2 k_B T_D/\beta_0 H), \tag{2.25}$$

$$R_S = \cos\left(\frac{1}{2}p\pi g(m^*/m_0)\right), \tag{2.26}$$

where k_B is the Boltzmann constant, T_D is the so-called Dingle temperature [46] , and g is the spin-splitting factor.

The temperature reduction factor R_T determines the temperature dependence of the oscillation amplitude. R_T approaches 1 for $2\pi^2 p k_B T/\beta_0 H \ll 1$ while for $2\pi^2 p k_B T/\beta_0 H > 1$, R_T is approximately given from eq. (2.24) as

$$R_T = \frac{4\pi^2 p k_B T}{\beta_0 H}\exp(-2\pi^2 p k_B T/\beta_0 H), \tag{2.27}$$

or

$$R_T = 29.4p\left(\frac{m^*}{m_0}\right)\left(\frac{T}{\mu_0 H}\right)\exp(-14.7p(m^*/m_0)T/\mu_0 H), \tag{2.28}$$

where T and $\mu_0 H$ are given in a unit of Kelvin and Tesla, respectively. Therefore, a plot of $\ln(A/T)$ (A : oscillation amplitude) versus T enables us to evaluate the effective mass m^*.

With given m^*, the Dingle reduction factor R_D determines the field dependence of the oscillation amplitude. T_D given by

$$T_D = \frac{\hbar}{2\pi k_B \langle \tau \rangle} \tag{2.29}$$

is related to the sample quality where $\langle \tau \rangle$ is the averaged scattering time over a cyclotron orbit. The lower T_D, the better quality of the sample. T_D is typically less than 1 K in organic conductors. Technical difficulties are sometimes met to evaluate T_D due to the existence of beating of the oscillations.

The oscillations are cancelled out between the carriers with up-spin and those with down-spin, since the Landau levels for both cases are shifted each other due to the Zeeman energy splitting of $\pm\frac{1}{2}g\mu_B H$. Such mechanism leads to the spin reduction factor R_S. For Q2D FS, since the effective mass m^* approximately varies with θ as

$$m^*(\theta) = \frac{m^*(\theta = 0°)}{\cos\theta}, \tag{2.30}$$

with eqs. (2.26) and (2.30), g value is derived by

$$N = \frac{g\mu_B}{2} \cdot \frac{1}{\cos\theta_N} + \frac{1}{2}, \tag{2.31}$$

where the angles θ_N are the so-called spin-splitting zeros corresponding to the minimum of the oscillation amplitude.

For the FS with more than two extremal orbits, the total magnetic moment $\tilde{M}$ is obtained simply by summing up each oscillation amplitude $\tilde{M}_i$:

$$\tilde{M} = \sum_i \tilde{M}_i = \sum_i \left(-\frac{\partial \tilde{\Omega}_i}{\partial H} \right)_\mu . \tag{2.32}$$

28

As is mentioned in Section 4.2, it should be noted that the LK formula is derived assuming that the chemical potential μ is constant. It has been shown that the LK formula provides correct results as long as the system is three-dimensional. For the system with two 2D FS, however, such assumption is no longer valid and the chemical potential oscillations (CPO) becomes significant as described in Section 4.2.

In contrast to the calculation of the thermodynamic properties, that of the conductivity $\tilde{\sigma}$ is not so straightforward. $\tilde{\sigma}$ is combined with the oscillations of the density of states, $\tilde{N}(H)$, as approximated by the following relation,

$$\tilde{\sigma} = \sigma_0 \frac{\tilde{N}(H)}{N_0},$$

(2.33)

where σ_0 and N_0 are the conductivity and the density of states without a field, respectively. $\tilde{N}(H)$ is found to be proportional to $d\tilde{M}_{\parallel}/dH$, and hence the same analysis based upon fore-mentioned damping factors is possible. If there are more than one orbit in the FS, however, a great care must be taken : the magnetization is additive while the observed resistivity ρ is the inverse of the total conductivity, that is,

$$\tilde{\rho} = \frac{1}{\sum_i \tilde{\sigma}_i}.$$

(2.34)

Therefore, the analysis of SdH oscillations with more than two extremal areas based upon the oscillation amplitude requires careful treatment.

Chapter 3

Experimental Methods

3.1   Experimental setup

3.1.1   Sample preparation : BEDT-TTF based superconductors

The samples of BEDT-TTF based organic superconductors are synthesized electrochemically. Typically, BEDT-TTF molecules and supporting electrolytes are dissolved into solvents in a glass cell and then two platinum electrodes, through which constant current of the order of a few μA is applied, are settled in the cell. In a few weeks, some small crystals grows at the anode.

The organic superconductors studied in this thesis, κ-(BEDT-TTF)$_2$Cu$_2$(CN)$_3$, κ-(BEDT-TTF)$_4$Hg$_{2.89}$Br$_8$, and κ-(BEDT-TTF)$_2$Cu(NCS)$_2$ were grown by Komatsu *et al.*, Lyubovskaya *et al.*, and Anzai *et al.*, respectively. The condition for the crystal growth are summarized in Table 3.1. The dimensions of samples were typically $\sim 1 \times 1 \times 0.03$-$0.1$ mm^3, with the shortest dimension along the inter-plane direction. The orientation of the crystals were determined by the crystal habit and/or by FS measurements.

	κ-$(ET)_2Cu_2(CN)_3$ [18]	κ-$(ET)_4Hg_{2.89}Br_8$ [47]	κ-$(ET)_2Cu(NCS)_2$ [13]
electrolyte	KCN CuCN 18-crown-6 ether	Bu$_4$NHgBr$_3$ HgBr$_2$	KSCN CuSCN 18-crown-6 ether
solvent	benzonitrile ethanol H$_2$O	trichloroethane	trichloroethane ethanol
shape	rhombus	rhombus	distorted hexagonal
dimensions (mm^3)	$\sim$1$\times$1$\times$0.02	$\sim$1$\times$1$\times$0.05	$\sim$0.5$\times$0.5$\times$0.05

Table 3.1: Condition for crystal growth and crystal shape for κ-$(BEDT$-$TTF)_2Cu_2(CN)_3$, κ-$(BEDT$-$TTF)_4Hg_{2.89}Br_8$, and κ-$(BEDT$-$TTF)_2Cu(NCS)_2$.
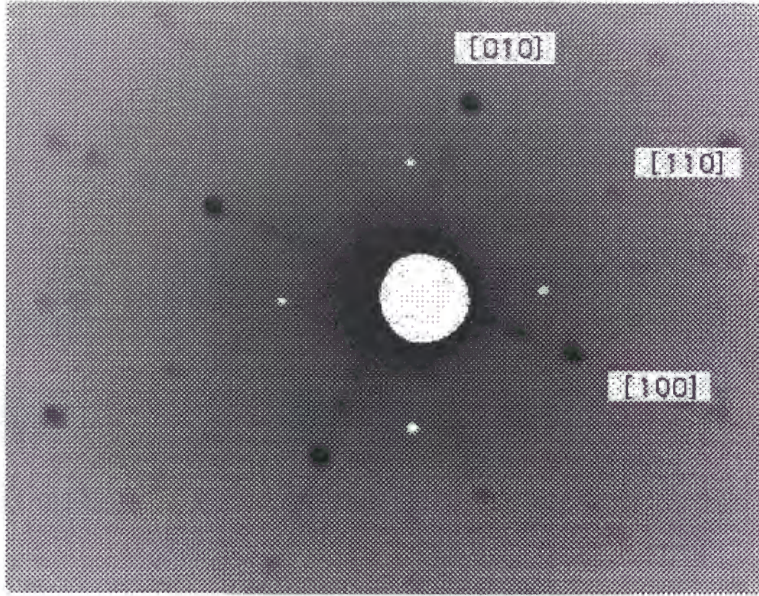
Figure 3.1: Laue pattern of Sr_2RuO_4.

3.1.2 Sample preparation : Sr_2RuO_4

Two single crystal rods, C62 and C113, of Sr_2RuO_4 studied in this work were grown by Adachi *et al.* and by Mao *et al.*, respectively by a floating-zone method [38]. In the process of single-crystal growth, polycrystalline feed rods containing a 15% excess of Ru were melted in the mixture of 10% O_2 + 90% Ar with total pressure of 3 bar. The crystals were grown at the feed speed of 4.5 cm/h. According to ac susceptibility measurements, the T_c for C113 was 1.45 K, while the initial T_c of 1.19 K for C62 increased drastically up to 1.43 K by annealing in air for 72 h. The crystal axes were determined by the Laue diffraction method (Fig. 3.1). The samples were polished to be parallelpiped after being cut by a diamond saw. Typical dimensions for the inter-plane resistivity and the in-plane resistivity were $\sim 1 \times 1 \times 0.5$ mm^3 and ~ 2-$4 \times 0.5 \times 0.06$ mm^3, respectively, with the shortest dimension along the inter-plane axis. In all the measurements except for those of superconductivity recurrence (Section 5.2), samples cut out of C62

were used.

3.1.3 Pressure cells

We developed two clamp-type pressure cells, rotatable in a narrow space. One is for a 1.5-K cryostat with a bore diameter of 49 mm and the other is for a 0.3-K cryostat with a bore diameter of 38 mm. The dimensions were $\phi25\text{mm}\times40$ mm and $\phi12\text{mm}\times30$ mm, respectively. Both pressure cells were of a similar structure as shown in Fig. 3.2. Daphne 7373 oil was used for a pressure medium. Electrical leads for the measurements were sealed by epoxy resin. The pressure value was evaluated by dividing a pressure load by the area of the piston inside the pressure cell. The large cell was found to be useful up to $\sim$12 kbar at room temperature while the small cell up to $\sim$8 kbar.

On cooling, it is well known that pressure values decrease due to thermal contraction of the pressure medium. For the large cell, pressure at low temperature is evaluated by the temperature-pressure relation, previously calibrated with use of a standard InSb pressure gauge. The pressure was estimated by T_c reduction with pressure for the small cell. For example, $-dT_c/dP \sim$2-3 kbar was reported for κ-(BEDT-TTF)$_2$Cu(NCS)$_2$ [24, 25]. A great care should be taken when temperature passes by the solidification point of the pressure medium around 200 K, depending on pressure values, in order to avoid inhomogeneous pressure associated with rapid cooling.

3.1.4 Magnetic field and cryostats

The cryostats mainly used in this study were a ^{4}He cryostat ($T \geq 1.4$ K), a ^{3}He cryostat ($T \geq 0.27$ K), and a dilution refrigerator ($T \geq 0.04$ K), combined with 9/11-T, 15/17-T, and 17/19-T superconducting magnets. The numbers separated by / denote the maximum filed value without/with a
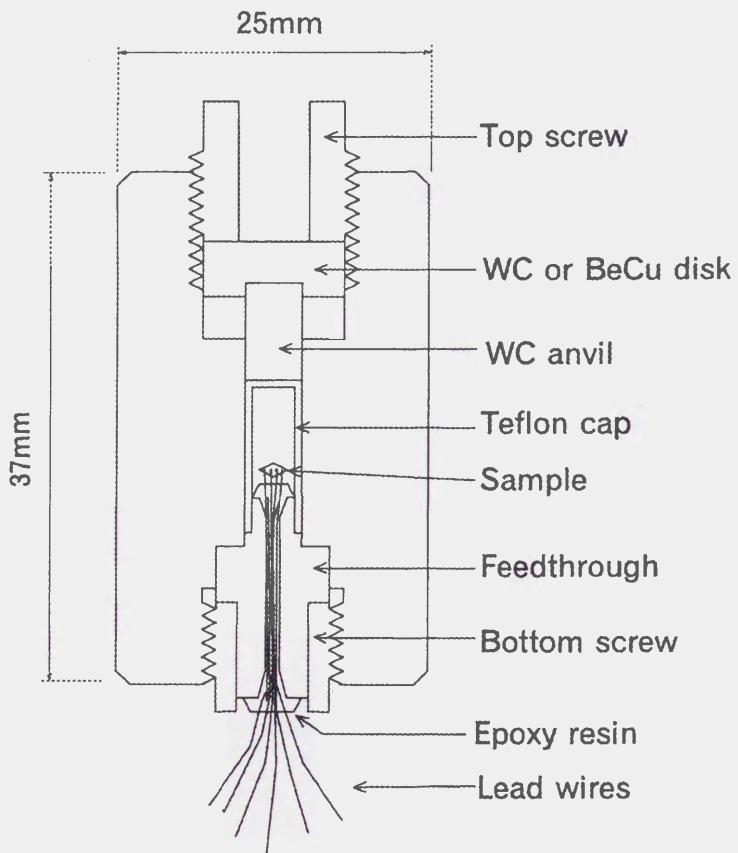
Figure 3.2: Structure of the pressure cell (the large cell).

lamdba refrigerator. For a ^{4}He cryostat, the lowest temperature of $\sim$1.4 K was obtained by evacuating liquid ^{4}He with a rotary pump. Temperature was monitored by combination of a carbon-glass resistor (CGR) and a platinum resistor or by a cernox resistor, and was controlled by a manostat below 4.2 K and by a temperature controller ITC503 (Oxford Instruments) above 4.2 K if necessary.

For a ^{3}He cryostat, liquid ^{3}He, condensed by a 1K pot, was evacuated by a cryosorption pump. The lowest temperature was $\sim$0.27 K. It was possible to re-condense ^{3}He within 30 minutes. Temperature was monitored by ITC503 with a cernox resistor and a ruthenium oxide resister.

For a dilution refrigerator, the lowest temperature was 37 mK measured by a ^{60}Co nuclear orientation thermometer. The temperature was monitored by combination of a ruthenium oxide resistor ($T \leq 7$ K) and a cernox resistor ($T \geq 1.5$ K). Below 1 K, temperature, measured by an AVS47 resistance bridge (RV-Electroniikka Oy), was controlled with a temperature controller TS530 (RV-Electroniikka Oy) while ITC503 was used in high temperature region. The operation system was controlled either manually or automatically with LabVIEW software (National Instruments).

The most remarkable characteristics of the ^{3}He refrigerator and the dilution refrigerator used in this study was the so-called top-loading system. This enabled us to exchange samples keeping the system at low temperature and to carry out measurements very efficiently. The procedure of the operation was as follows : when we install a probe, the probe was first placed on a vacuum lock to pumped out a space inside the probe down to 10^{-2} Torr so that ^{3}He gas or ^{3}He-^{4}He mixture was not contaminated by air. Then, after opening a gate valve at the vacuum lock the probe was inserted slowly, keeping a sample chamber in a condensed state. It was possible to cool down samples with any cooling rate. After being cooled by a 1K pot, the probe

was settled to the final position. On the other hand, for the probe extraction from the cryostat, the probe was pulled up gradually keeping the pressure inside as low as possible in order to reduce a loss of ^{3}He gas or ^{3}He-^{4}He mixture. Then, the gate valve was closed at the initial position of the probe so that air was vented into the sample space.

A part of experiments in Section 5.1 and 5.2 were carried out at the High Magnetic Field Laboratory, Institute for Material Research (IMR), Tohoku University and the National High Magnetic Field Laboratory (NHMFL), in Florida, U.S.A., respectively.

At IMR, a hybrid magnet (HM1), combination of a superconducting magnet and a resistive magnet, was used. The maximum field attained was 27 T and the lowest temperature of $\sim$0.5 K was obtained by a ^{3}He refrigerator. Samples could be rotated uniaxially using an ac-motor. The relative angle was evaluated by the resistance value of a potentio-meter.

At NHMFL, a 33-T resistive magnet (Cell 12) combined with a dilution refrigerator was used. The lowest temperature of $\sim$50 mK was attained. Due to narrowness of the sample space with a diameter of 13 mm, a rotator using piezoelectric crystals was adopted as described in the next section.

3.2   Control of field orientation

3.2.1   Definition of field orientation

For materials with low-dimensional electronic structure, it is essential to specify the orientation of an applied magnetic field. In the present study, a great care was taken to field orientation against the crystallographic axes of samples.

In this study, the field orientation is specified by angles θ and ϕ as shown in Fig. 3.3; the polar angle θ represents the one measured from the normal to the 2D plane and the azimuthal angle ϕ represents the one measured from
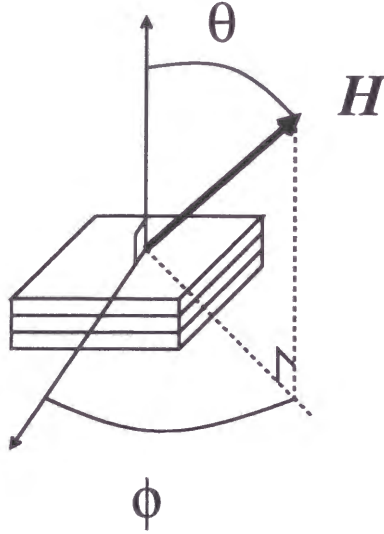
Figure 3.3: Definition of the polar angle θ and the azimuthal angle ϕ. Note that ϕ represents a tilt from the crystallographic axis within the conducting plane.

the crystallographic axis within the conducting 2D plane. For Sr_2RuO_4, ϕ represents the angle from the a axis, while for κ-$(BEDT\text{-}TTF)_2Cu_2(CN)_3$ and κ-$(BEDT\text{-}TTF)_4Hg_{2.89}Br_8$, ϕ represents the angle from the long-diagonal axis of the crystal (the c axis and the a axis for κ-$(BEDT\text{-}TTF)_2Cu_2(CN)_3$ and κ-$(BEDT\text{-}TTF)_4Hg_{2.89}Br_8$, respectively). The notation such as [110] or [100] were also used for Sr_2RuO_4 in case of need, corresponding to (θ=90°, ϕ=45°), (θ=90°, ϕ=0°), respectively.

3.2.2 Double-axis rotator

In order to orient a magnetic field to a required direction, rotation associated with two axes are necessary. In the present study two types of double-axis rotator were used.

In the first case a system with a pulley and a stainless wire was used in a ^{4}He cryostat. In order to control the polar angle θ, the sample holder was rotated by a stepping motor via a stainless wire. Relatively large sample
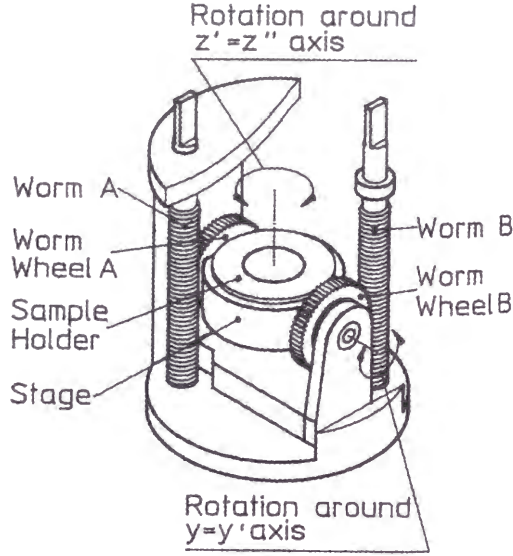
Figure 3.4: View of the double-axis rotator [48].

space was available in this case. In addition, heating by the rotation was little because no gear mechanism was set near the sample space. The backlash was relatively small but the play on the reverse of rotation was rather large: it was typically 5-15° depending on wire tension. The stepping motor was controlled by a computer, enabling the angle resolution of ~0.01°. ϕ was changed manually by rotating the sample holder using a fork-like piece with an accuracy of ~1°.

The second one (Fig. 3.4) was designed by Oxford Instruments for a ^{3}He cryostat and a dilution refrigerator, after the design by Settai *et al.* [48]. The angles θ and ϕ was rotatable independently. Rotation of two stepping motors (Θ, Φ) was related to θ and ϕ by the following equation,

$$\theta = \Theta, \tag{3.1}$$

$$\phi = \Theta - \Phi. \tag{3.2}$$

The accuracy of ~0.01° was realized for both rotations. Successive rotation at low temperature generated considerable heating caused by friction.

3.2.3 Piezoelectric rotator

Although sample rotation with the above-mentioned methods in a very narrow space is difficult in general, it becomes possible to incline a sample holder in a limited angle region, *e.g.* by $\pm 10°$ with use of a piezoelectric rotator. This device was developed by Unisoku. The schematic drawing is illustrated in Fig. 3.5. Two piezoelectric crystals with dimensions of $3 \times 3 \times 3.5$ mm^3, de-
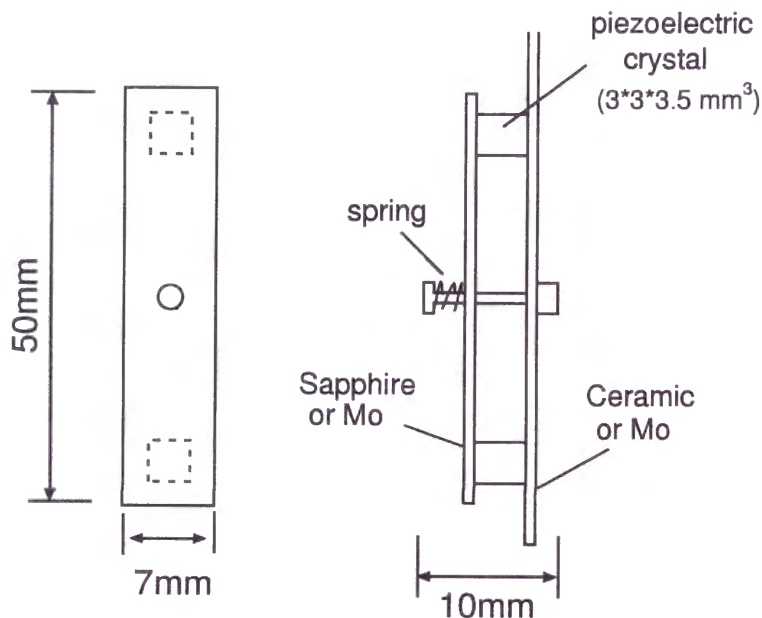
Figure 3.5: Schematic drawing of the rotator with piezoelectric crystals.

vices used for a low-temperature scanning tunneling microscopy (STM), were placed on the base of a rotator. The base part and the moving plate were made of molybdenum metal. When a series of saw-tooth pulses were applied to the piezoelectric crystals, they were distorted with shear strain. Then, the sample holder was shifted. In the decreasing duration of the pulse, due to quick restoration of the piezoelectric crystals the sample holder remained at the same position because of the inertia. By repeating the process, a sample holder was derived forward.

The angular resolution of $\sim 0.01°$ was attained and heating by rotation

was found to be rather weak compared with the above-mentioned methods. The absolute value of the tilt angle was evaluated by using a small Hall sensor THS118 (Toshiba). It was possible to incline the sample holder by $\pm10°$ in a space with a diameter of 13 mm.

This device requires only two electrical leads for applying a saw-tooth pulse, and therefore the structure becomes compact and simple. Moreover, this is suitable for experiments at very low temperature or in a strong magnetic field, since the parts can be replaced with nonmetallic materials such as ceramics or sapphire. However, there remains some room for improvements as below: (1) torque is not strong because a sample holder is driven by friction. As a result, moving speed is not sometimes uniform or is different between clockwise and anticlockwise directions. (2) Since there is no reliable small Hall sensor available in a strong magnetic field, one should find an appropriate means to evaluate the angle.

3.3 Measurements

3.3.1 Electrical resistance

For measurements in organic conductors, four contacts were placed on the same side for in-plane resistance measurements while a pair of contacts were placed on both sides for inter-plane resistance measurements, as displayed in Fig. 3.6. Such configurations were adopted for materials with high anisotropy of the conductivity between the in-plane and the inter-plane direction. Electrical leads of 10-μm or 20-μm platinum wire were attached by a conducting carbon paste (Fujikura Kasei) and the contact resistance was typically less than 50 Ω.

For Sr_2RuO_4, electrical leads of 20-μm gold wire were attached using Dupont silver paint 6838 by heating at 500°C for 8 minutes in air. Typical contact resistance was estimated to be $\sim$0.1 Ω. For in-plane resistance
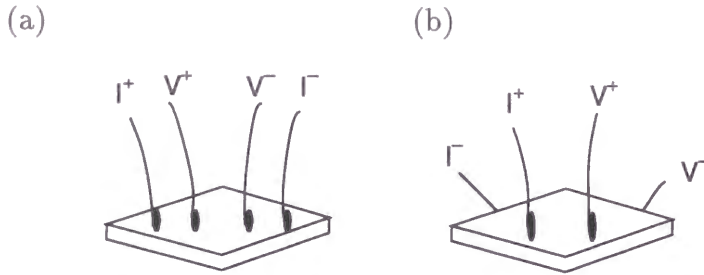
Figure 3.6: Contact configurations for measurements of (a) the in-plane resistance and (b) the inter-plane resistance of organic superconductors.

measurements of Sr_2RuO_4, two current contacts covered the opposite ends totally to ensure a homogeneous current flow and two voltage contacts were attached to shorten along all the RuO_2 layers, as displayed in Fig. 3.7. For the inter-plane resistance case, contacts were attached in the same manner as organic conductors.
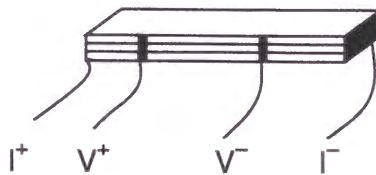
Figure 3.7: Contact configuration for measurements of the in-plane resistivity of Sr_2RuO_4.

The electric resistance was measured using an ac four-probe method with a typical current of 10-1000μA, depending on temperature and resistance values. Measuring frequency was 137 Hz for usual cases, but 11-17 Hz for measurements at NHMFL to reduce a noise associated with a resistive magnet. A high precision preamplifier (NF Electronic Instruments, model SA-400F3) was used for very small resistance measurements.

3.3.2 Torque magnetometry

For the observation of quantum oscillations in magnetization (de Haas-van Alphen effect) a capacitive torque device (Oxford Instruments) was taken up

in this study. The structure of the torque-meter is shown in Fig. 3.8. A pair of etched silicon plates, on which a gold pad was evaporated, forms a capacitance with a gap distance of ∼0.1 mm. A sample was placed on one of the capacitance plate with a tiny amount of grease. The sample stage could be rotated uniaxially by 360° with an angular resolution of 0.1°.

(a)

To current source I$^+$

To current source I$^-$

To capacitance bridge (AH2500)

Lower capacitance electrode

Cantilever/upper capacitance electrode

Sample

Current loop

(b)

H

m

0.1 mm

Cantilever dimensions 7.5*5 mm^2
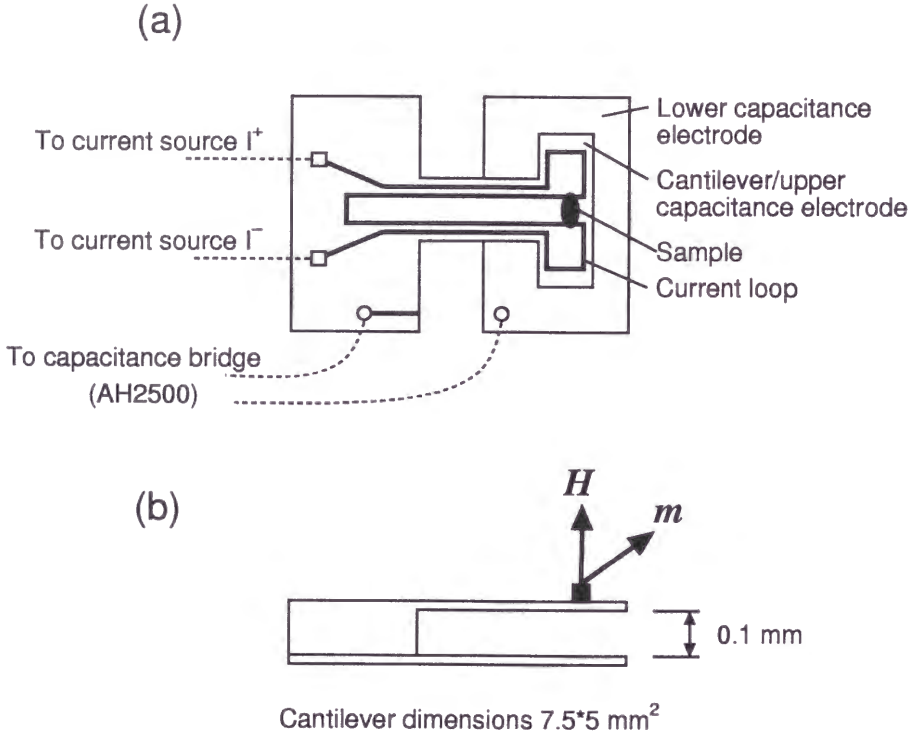
Figure 3.8: (a) Top view and (b) side view of the capacitive torque-meter.

When a magnet field is applied, magnetic torque $\tau = m \times H$, generated by a magnetization component perpendicular to the applied filed, is detected by a deflection Δd of the thin capacitance plate as a change in the capacitance value ΔC. In the region where the deflection Δd is much smaller than the gap distance d (i.e. $d \gg \Delta d$), ΔC is proportional to torque $|\tau|$. Therefore, magnetization m is obtained as

$$m = \frac{k \Delta C}{H \sin \theta_0},$$

(3.3)

where k is a coefficient, and θ_0 is the angle between $\boldsymbol{m}$ and $\boldsymbol{H}$. If $\Delta C/C_0$ (C_0 : capacitance value without a magnetic field) exceeds a certain value, non-linear response causing the torque interaction in quantum oscillations can appear.
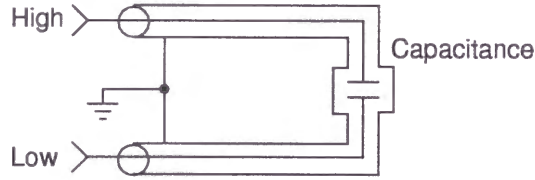
Figure 3.9: Three terminal method for capacitance measurements.

This torque-meter was equipped with a single current loop, which generated a magnetic moment represented by $m = IS$ where I is the current and S is the enclosed area by the loop. This current loop enabled us to calibrate the absolute value of torque easily. The capacitance was measured with a usual three-terminal method (Fig. 3.9) using a high precision capacitance bridge AH2500 (Andeen Hagerling) with a fixed measuring frequency of 1 kHz. Below 1.5 K, heating associated with dielectric loss of the capacitance was not negligible and it was necessary to optimize the measuring voltage of the bridge.

Chapter 4

Angle-Dependent Galvanomagnetic Effects and Quantum Oscillations

4.1   Introduction

For Q2D electronic systems such as organic superconductors, the FS has been extensively studied by means of both angle-dependent magnetoresistance oscillations (AMRO) and quantum oscillations [17].

As a result of Landau quantization by a strong magnetic field, the energy dispersion is discretized into Landau levels, leading to quantum oscillations. In the analysis of quantum oscillations, the oscillation frequency with $1/H$ periodicity provides knowledge of the extremal cross-sectional area of the FS, which enables us to investigate the topology as a function of the polar angle.

A cylindrical FS in Q2D electronic systems is also treasury of new phenomena in quantum oscillations: colossal quantum oscillations or the magnetic breakdown (MB) effect has been observed in these systems [17]. In addition, not only the oscillatory components corresponding to the cross-sectional area of the constituent FS branches but also those with the sum and difference frequencies have been sometimes found. The origin of this finding can be attributed to the MB effect appearing in a high magnetic field, the magnetic interaction (MI) effect, or chemical potential oscillations

(CPO).

On the other hand, for a Q2D cylindrical FS with slight warping along the axis, there exist certain orientations known as Yamaji angles [40, 41], where the cross-sectional areas of all the cyclotron orbits become identical within a deviation of the order of $(t_\perp/\epsilon_F)^2$, In such situation, the FS acts as being purely two-dimensional, and hence the inter-plane resistivity exhibits the maximum of the angle-dependent magnetoresistance oscillations (AMRO). From the period of the oscillations in AMRO, the Fermi wave number for a certain direction in the 2D plane can be obtained so as to map out the FS contour as explained in Section 2.1. In this sense, AMRO can be an important supplementary method to dHvA and SdH effects.

In addition, a resistance peak has been observed in the angle-dependent magnetoresistance for organic conductors in magnetic fields applied parallel to the conducting plane. Such peaks were first observed by Kartsovnik *et al.* [49]. It is noteworthy that with increasing the field strength, the peak structure becomes more prominent but the peak width of 4~5° is not influenced by the field strength. This indicates that the phenomenon is ascribed to a topological effect of the FS, similar to AMRO.

Q2D electronic systems exhibit a rich variety of semiclassical and quantum phenomena as shown above. However, there remain not a few subjects to be clarified. First of all, it should be noted that almost all these phenomena have been observed in organic conductors. It is interesting to know whether or not similar phenomena can be observed in Q2D oxide conductors. Then we applied the above-mentioned techniques to Sr_2RuO_4, whose quantum oscillations have been reported. The former part of this chapter (Section 4.2-4.4) is devoted to this attempt, in which successful observation of the angle-dependent galvanomagnetic effects and new quantum oscillatory phenomena are discussed. We also compare experimental results of Sr_2RuO_4

to those of organic conductors.

Meanwhile, slow quantum oscillations, which cannot be ascribed to the calculated band calculation, have been sometimes observed in organic conductors. This phenomenon is anomalous, since according to the angle dependence of the oscillation frequency, they behave as if they are three-dimensional (3D) FS. In Section 4.5, the anomalous behavior is discussed in relation to the origin based upon the experimental results of κ-(BEDT-TTF)$_2$Cu$_2$(CN)$_3$.

4.2 Angle-dependent magnetoresistance oscillations (AMRO) in Sr$_2$RuO$_4$

4.2.1 Fermi surface topology of Sr$_2$RuO$_4$

According to the band calculation [28, 29] , the FS of Sr$_2$RuO$_4$ is Q2D and consists of three cylindrical branches: one hole branch (α) around the X point and two electron branches (β and γ) around the Γ point, as displayed in Section 1.4.

Measurements of quantum oscillations by SdH and dHvA effects [30, 31, 32] have provided FS parameters consistent with the calculation, except for the enhanced masses. Moreover, the Hall coefficient [50, 51] and the specific heat [35] were fairly consistent with the results derived from the quantum oscillations [52]. On the other hand, the angle-resolved photoemission spectroscopy (ARPES) measurements [53, 54, 55] gave an inconsistent result; one sheet of the FS is assigned as an electron branch, and the other two sheets as hole branches. Although it has been clarified that the quantum oscillations have provided the correct FS of the bulk electronic states for Sr$_2$RuO$_4$ [56], these techniques can bring about only the cross-sectional areas of the FS. Further investigation of the FS by alternative techniques, especially by those which can map out the FS contour is desirable. In the following section,

the first results of AMRO measurements in Sr_2RuO_4 are reported and are compared with the calculated band structure.

4.2.2   Results and discussion

When tilting the field direction from $\theta=0°$, a series of peaks in the inter-plane magnetoresistance were clearly observed at 1.5 K under a magnetic field of 15 T, as shown in Fig. 4.1. Two-fold symmetry with respect to θ and four-fold symmetry with respect to ϕ were identified in the oscillations. As shown in Fig. 4.2, the oscillatory structure appeared above 5 T and became more prominent with increasing field strength, but the peak position was not influenced by the magnetic field. In addition, a pronounced peak structure was observed when the field was applied parallel to the conducting plane ($\theta=\pm90°$). The origin and its implication are discussed in Section 4.4.

The observed $\tan\theta$ periodicity, which is demonstrated in Fig. 4.3, confirms that the oscillations are due to AMRO. The peaks were assigned well by assuming only one series of $\tan\theta_n$ versus $n\mp1/4$ plot for all ϕ. The AMRO pattern was not changed even if the sample was cooled down to 0.1 K. Slight deviation from $\tan\theta$ periodicity observed in a higher angle region ($|\theta|\geq75°$) for $\phi\simeq45°$ is ascribable to the assumption of a simple energy dispersion in the derivation of eq. (2.4).

In order to derive a FS contour, we analyze the data according to the model by Kartsovnik $et\ al.$ [57], which is an extension of Yagi's results [41] to the FS with arbitrary cross-sectional shape, taking the crystal structure into account. By introducing a new hopping vector $\boldsymbol{u}=(u_x, u_y, d)$, the energy dispersion $\epsilon(\boldsymbol{k})$ represented by eq. (2.1) is replaced with the following one,

$$\epsilon(\boldsymbol{k}) = \epsilon_{2D}(k_x, k_y) - 2t_\perp \cos(k_z d + k_x u_x + k_y u_y), \qquad (4.1)$$

where ϵ_{2D} is the in-plane energy dispersion. The above energy dispersion corresponds to that for materials with rather low crystal symmetry such as
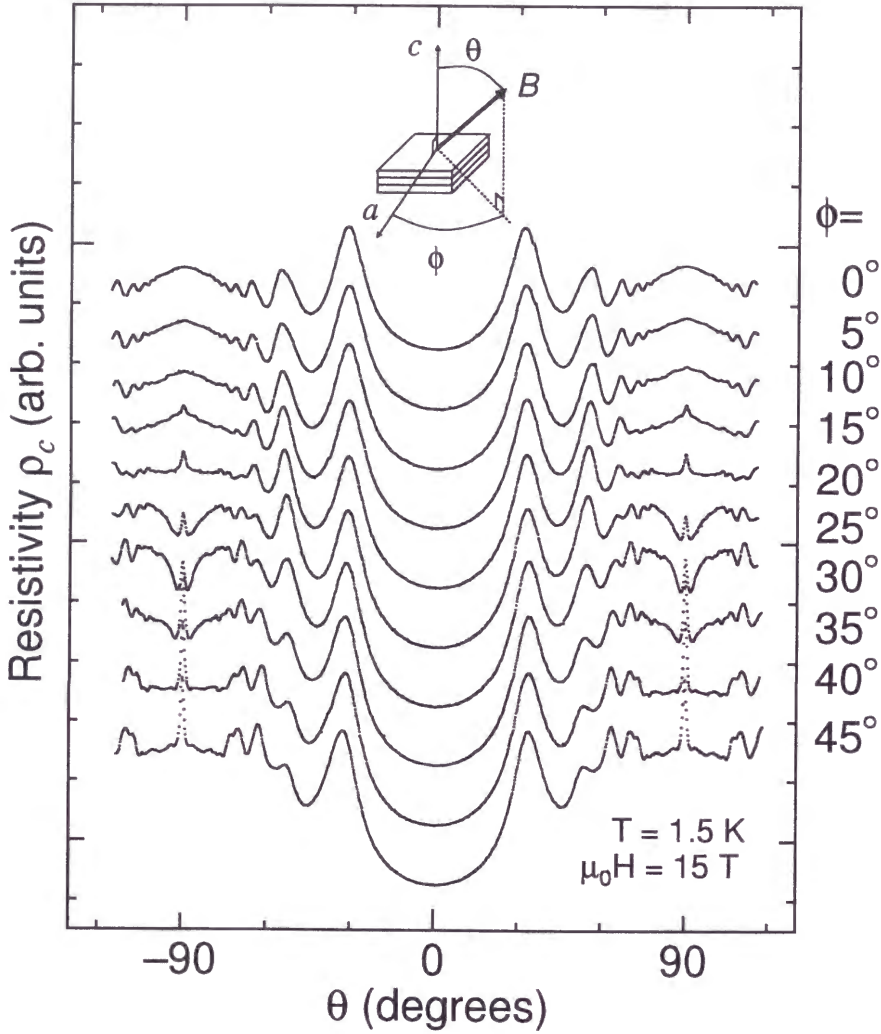
Figure 4.1: AMRO observed in the inter-plane resistivity of Sr_2RuO_4 at 1.5 K under a magnetic field of 15 T for various ϕ values. The field orientation is defined by the polar angle θ and azimuthal angle ϕ as shown in the inset. The θ dependence of the resistivity for different ϕ is presented in arbitrary units by shifting with each other in the vertical direction.

Figure 4.2: AMRO at different magnetic fields for $\phi=45°$ at 1.5 K.

Figure 4.3: Plot of $\tan\theta_n$ against $n \mp 1/4$ for $\phi=0°$, 15°, 30°, and 45°, derived from Fig. 4.1.

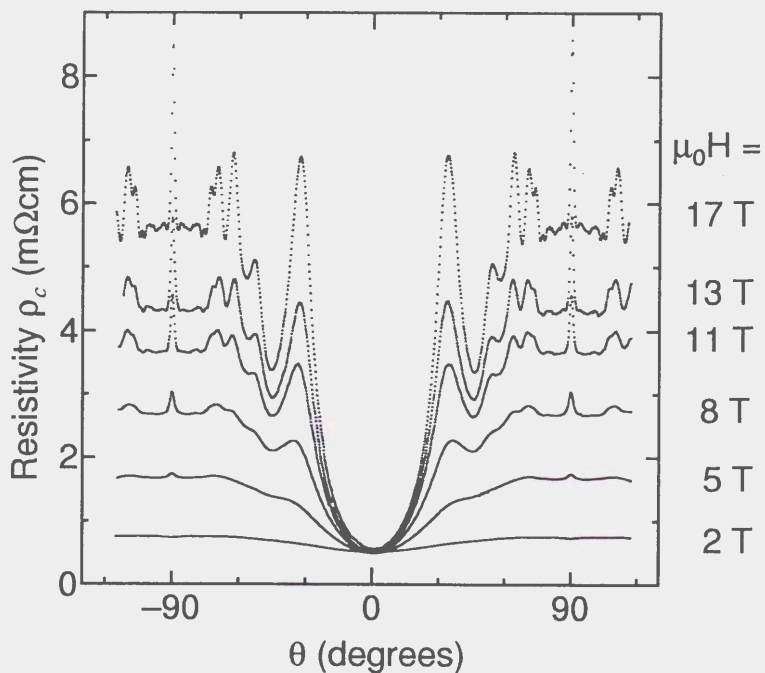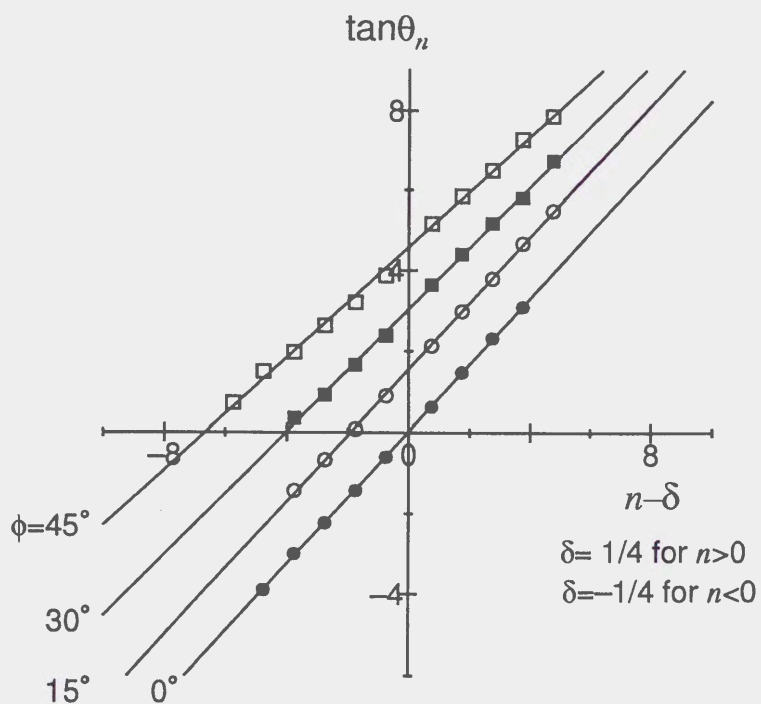organic conductors, in which molecules in the conducting layers are arranged so that the long axis of the molecule is tilted by $\sim20°$ from the inter-plane direction. The averaged velocity is obtained as

$$
\bar{v}_z(k_z^{(0)}) = \frac{1}{\hbar}\overline{\left(\frac{\partial\epsilon}{\partial k_z}\right)}
$$

$$
\propto \sin(k_z^{(0)}d)\cos\left(|k_H^{(\mathrm{max})}d\tan\theta - (\boldsymbol{k}_\parallel^{(\mathrm{max})}\cdot\boldsymbol{u})| - \frac{\pi}{4}\right) \quad (4.2)
$$

and the condition for AMRO is given as

$$
dk_H^{(\mathrm{max})}\tan\theta_n = \pi\left(n\mp\frac{1}{4}\right) + (\boldsymbol{k}_{\mathrm{F}\parallel}^{(\mathrm{max})}\cdot\boldsymbol{u}) \quad (4.3)
$$

where θ_n is the angle giving the n-th peak, signs $\mp$ correspond to positive and negative values of θ_n. As shown in Fig. 4.4, we introduce k_H as the component of in-plane Fermi wave-number vector $\boldsymbol{k}_{\mathrm{F}\parallel}$ along the in-plane projection of the field, and define $k_H^{(\mathrm{max})}$ as the maximum value of k_H for possible $\boldsymbol{k}_{\mathrm{F}\parallel}$ on the FS contour. $\boldsymbol{k}_{\mathrm{F}\parallel}^{(\mathrm{max})}$ is $\boldsymbol{k}_{\mathrm{F}\parallel}$ giving $k_H^{(\mathrm{max})}$. The FS contour is obtained as an envelope of the lines perpendicularly intersecting a line connecting the origin and $k_H^{(\mathrm{max})}$ at $k_H^{(\mathrm{max})}$ [57]. It is noteworthy that the FS obtained by the AMRO consists of $\boldsymbol{k}_{\mathrm{F}\parallel}$ averaged over the inter-plane direction. Equation (4.3) also indicates that the peak position is independent of the field strength. The experimental results are consistent with this. For materials with tetragonal symmetry such as Sr_2RuO_4, the in-plane hopping component $\boldsymbol{u}$ can be set to $\boldsymbol{u}=0$.

By employing the inter-plane lattice parameter ($c = 1.27$ nm) as d, an FS mapping can be derived in the 2D reciprocal space after the plot of $\tan\theta_n$ versus $n\mp1/4$ for various ϕ. The result is illustrated in Fig. 4.5. The solid circles represent $k_H^{(\mathrm{max})}$ obtained from eq. (4.3) with $d=1.27$ nm. The resultant contour of $\boldsymbol{k}_{\mathrm{F}\parallel}$ is depicted by the solid line. The dotted lines show the FS by the band calculation. The experimental result fits the calculated α branch. The SdH oscillations observed by a field sweep for $\theta=0°$ gave a
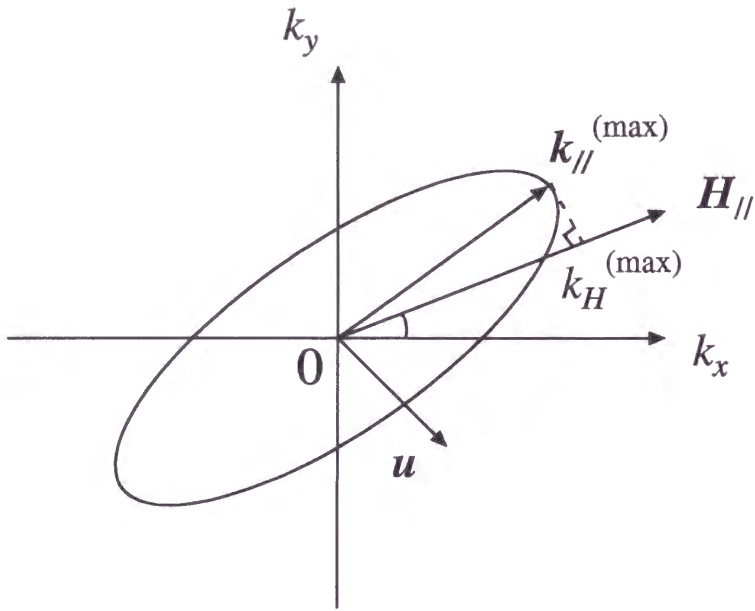
Figure 4.4: Cross-section of the Fermi surface within the $k_x k_y$ plane
. $\boldsymbol{H}_{\parallel}$ is the magnetic field component parallel to the conducting plane (xy-plane), $\boldsymbol{k}_{\parallel}^{(\mathrm{max})}$ is the in-plane component of the Fermi wave number whose projection in the direction to $\boldsymbol{H}_{\parallel}$ attains the maximum value of $k_H^{(\mathrm{max})}$, $\boldsymbol{u}$ is the in-plane component of the hopping vector.

Figure 4.5: The $k_H^{(max)}$ values obtained by AMRO (solid circles), Fermi surface contour derived from $k_H^{(max)}$ (solid line), and the calculated FS of Sr_2RuO_4 (dotted line) within the 2D reciprocal space.

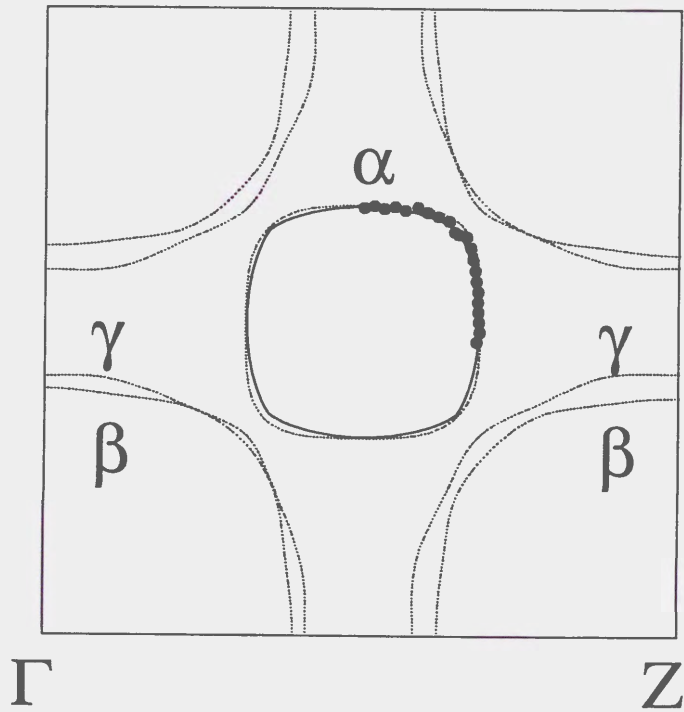value of $(2.85\pm0.08)\times10^{15}\mathrm{cm}^{-2}$ as the cross-sectional area of the α branch. The estimated FS cross-sectional area by AMRO, $3.0\times10^{15}\mathrm{cm}^{-2}$, is in good agreement with the result of the SdH oscillations. The result is also consistent with the size and shape of the observed α branch in ARPES measurements.

On the other hand, it is worth noting that the unit cell parameter c corresponds to twice of the distance between RuO_2 layers, which shift alternatively by $(a/2, a/2)$ (a : the in-plane lattice parameter) in the inter-plane direction (see Fig. 1.6). The calculated FS for the β branch exhibits a periodicity with $4\pi/c$, in contrast to the FS for the α branch, which exhibits a periodicity of $2\pi/c$ [58]. By adopting the value corresponding to $c/2$ rather than c for d in eq. (4.3), we find that the FS contour corresponding to the β branch can also be fitted fairly well, due to the fact that the FS contour of the β branch is of similar shape to that of the α branch with a diameter magnified by a factor of almost 2. In this case, the estimated FS cross-sectional area by AMRO, $1.2\times10^{16}\mathrm{cm}^{-2}$, is also in good agreement with the one obtained by quantum oscillations, $1.21\times10^{16}\mathrm{cm}^{-2}$ [30]. On the other hand, the β branch by the ARPES measurements is inconsistent with the present results. Thus the FS contour derived from the AMRO can be assigned well to both the α and β branches. Incidentally, the evaluated $\omega_c\tau$ value of 4.0 and 1.9 for the α and β branches, respectively, satisfies the condition of AMRO, $\omega_c\tau > 1$, in the constant mean-free-path approximation, where ω_c is the cyclotron frequency and τ is the relaxation time for scattering.

To clarify the origin of AMRO in Sr_2RuO_4, an interesting attempt has been carried out by Ishii $et\ al.$ [59]. They numerically calculated the Shockley tube integral (eq. (2.6)) with the calculated FS instead of a simple energy dispersion. The results are shown in Fig. 4.6. AMRO-like structure was confirmed in both the α and the β branches but it fails to explain the entire angle dependence of the magnetoresistance. This implies that the accuracy
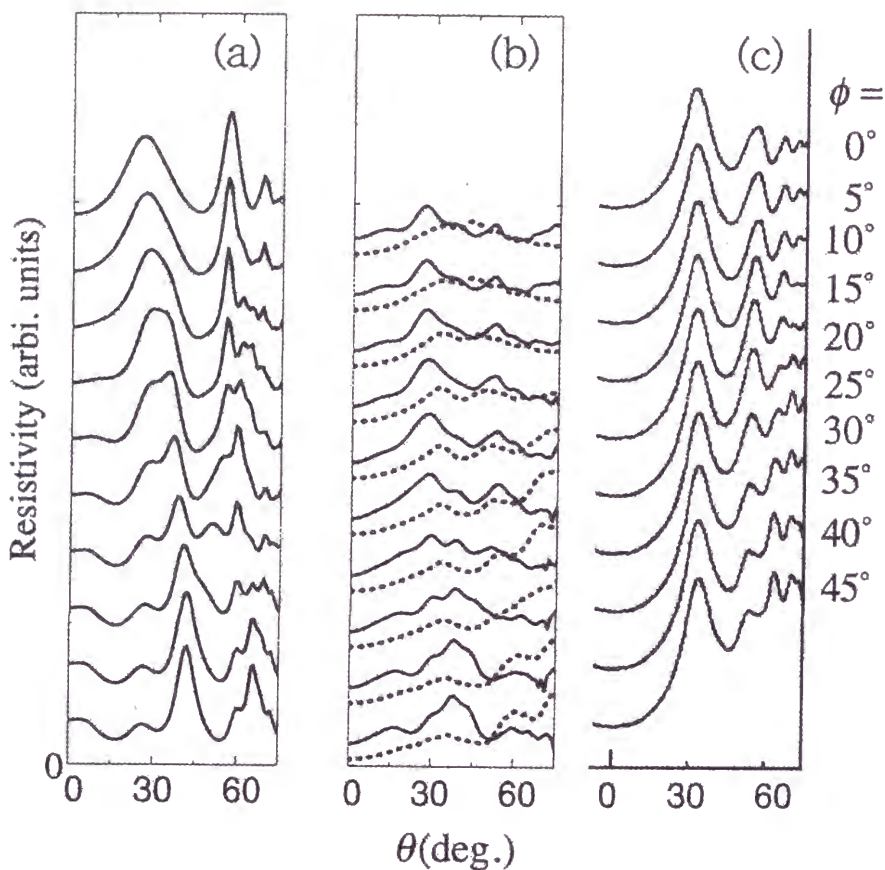
Figure 4.6: Calculated angle dependence of the inter-plane resistivity at each FS branch with constant τ [59]: (a) contributions from the α branch and (b) contributions form the β branch (solid curves) and from the γ branch (dotted curved). Experimental results [60] are shown in (c). The θ dependence of the resistivity for different ϕ is presented in arbitrary units by shifting with each other in the vertical direction.

of the band calculation in the inter-plane direction is not enough to reproduce the observed AMRO.

On the other hand, a detailed study on the FS topology of Sr_2RuO_4 by means of quantum oscillations was carried out recently by Bergemann et $al.$ [61]. They reproduced the observed angle dependence of dHvA frequencies by numerical simulation, from which most reasonable pattern and its amplitude for the inter-plane transfer energy were obtained. According to them, the β branch dominates ρ_c with a 86% share, compared with 8% for the α branch and 6% for the γ branch, implying that the AMRO is attributed to the β branch. These kinds of new approach will provide further insight into AMRO experiments.

Finally, I point out the significance of the present study of AMRO in Sr_2RuO_4. It has been widely recognized that the knowledge of the electronic structure is indispensable for thorough understanding of physical properties. However, in layered oxide conductors, ARPES measurements were the only way to elucidate FS topology and hence other techniques have been desired. This is because ARPES is a surface-sensitive technique and sometimes gave an inconsistent result, depending on materials or measuring conditions. In fact, in Sr_2RuO_4, the results by ARPES differed from that by quantum oscillations. Therefore, the observation of AMRO in Sr_2RuO_4 is substantial in that it is useful for the layered oxide conductors as well. Taking into account that semiclassical effects such as AMRO are less smeared out by temperature and/or impurity than quantum oscillations, this finding has opened up a new possibility of FS studies in layered oxide conductors.

4.3 Chemical potential oscillations (CPO) in Sr_2RuO_4

4.3.1 Frequency mixing in quantum oscillations

The electronic structure of Sr_2RuO_4, as revealed by quantum oscillations [30, 31, 32] and AMRO [60, 62], consists of the three cylindrical FS branches, α, β, and γ. The areas and their topology are in good agreement with the calculated cylindrical FS [28, 29]. According to the band calculation, the three branches are separated in the momentum space and can be treated as a multi-band system accompanying independent Q2D FSs. This situation differs from the case for organic conductors, in which two FS branches can form a typical magnetic breakdown (MB) network (α and β) in the high magnetic field region (see Fig. 1.5).

In this section, we present the sum and difference oscillatory components of SdH oscillations in Sr_2RuO_4 with frequencies $F_{\beta\pm\alpha} = F_\beta \pm F_\alpha$, which were notably enhanced at the so-called Yamaji angle , where F_α and F_β are the frequencies corresponding to the α and β branches, respectively. This unusual enhancement is attributable to the chemical potential oscillation (CPO) effect [63, 64] characteristic of 2D electronic systems, rather than the magnetic interaction (MI) effect, according to the temperature dependence of the oscillation amplitude.

Figure 4.7 displays a typical oscillatory component of SdH oscillations in Sr_2RuO_4, obtained at 0.1 K under a magnetic field oriented at $\theta=31°$, where θ denotes the angle between the field and the crystalline c axis. The inset shows the fast Fourier transform (FFT) spectrum, in which fundamental frequencies were observed as $F_\alpha=3.44$ kT, $F_\beta=14.54$ kT, and $F_\gamma=21.17$ kT for $\theta=31°$. In addition, it is noteworthy that FFT components corresponding to $F_{\beta\pm\alpha} = F_\beta \pm F_\alpha$ were clearly resolved.
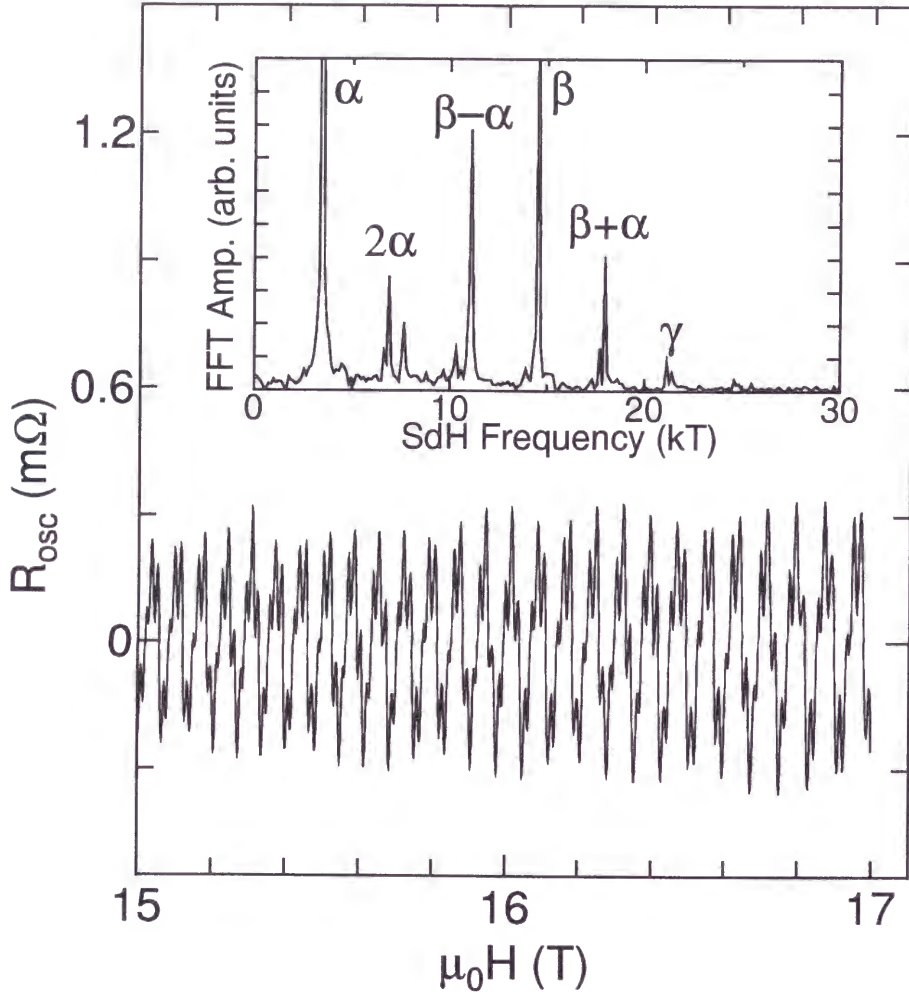
Figure 4.7: The oscillatory components of Shubnikov-de Haas oscillations observed in the inter-plane resistivity of Sr_2RuO_4 at 0.1 K and $\theta=31°$, where θ denotes the tilt angle measured from the c axis. The inset shows the FFT spectrum of the oscillations.

It is of great importance to see whether or not the same frequencies are observed in the thermodynamic properties such as magnetization. Figure 4.8 displays an oscillatory component of dHvA oscillations in Sr_2RuO_4 detected by a capacitive torque-meter at 0.3 K under the magnetic field at θ=24°. To avoid possible torque interaction (TI) effect producing combination frequencies, which is a kind of feedback effect of magnetic torque associated with a deflection of the cantilever, the sample mass of $(7 \pm 1)\mu g$ was adopted. The same oscillatory components of $F_{\beta\pm\alpha}$ were also clearly visible in dHvA oscillations, although the relative amplitude to the fundamental frequencies were small compared to that in SdH oscillations.

Figure 4.9(a) shows the polar-angle θ dependence of the FFT spectra. All of the observed SdH frequencies shift to higher values with increasing θ as $1/\cos\theta$, being consistent with the θ dependence of the cross-sectional area of a cylindrical FS. It should be noted that the components with frequencies of $F_{\beta\pm\alpha} = F_\beta \pm F_\alpha$ were also enhanced at θ=31°. The oscillation amplitude is represented as a function of θ in Fig. 4.9(b). The amplitude for F_α and F_β increased significantly in the narrow angle region centered at $\theta \sim$30°. Besides, those for the frequencies $F_{\beta\pm\alpha}$ emerged only in the angle region around $\theta \sim$30°. The amplitude for F_α showed a dip around θ=25°, which is attributable to the effect of the slight warping of the cylindrical FS [31].

The angle dependence is related to the AMRO discussed in the previous section. Figure 4.10 shows the AMRO in Sr_2RuO_4, observed at 1.5 K under a magnetic field of 15 T. It is noteworthy that the angle of the first AMRO peak appearing around θ=33° was close to the value where all of the SdH oscillation amplitude were most prominent as shown in Fig. 4.9(b). This indicates a close relationship between the oscillation amplitude and the two-dimensionality of the FS. At the Yamaji angles giving the AMRO peak, the FS becomes 2D and more carriers can fall in the extremal orbits related to
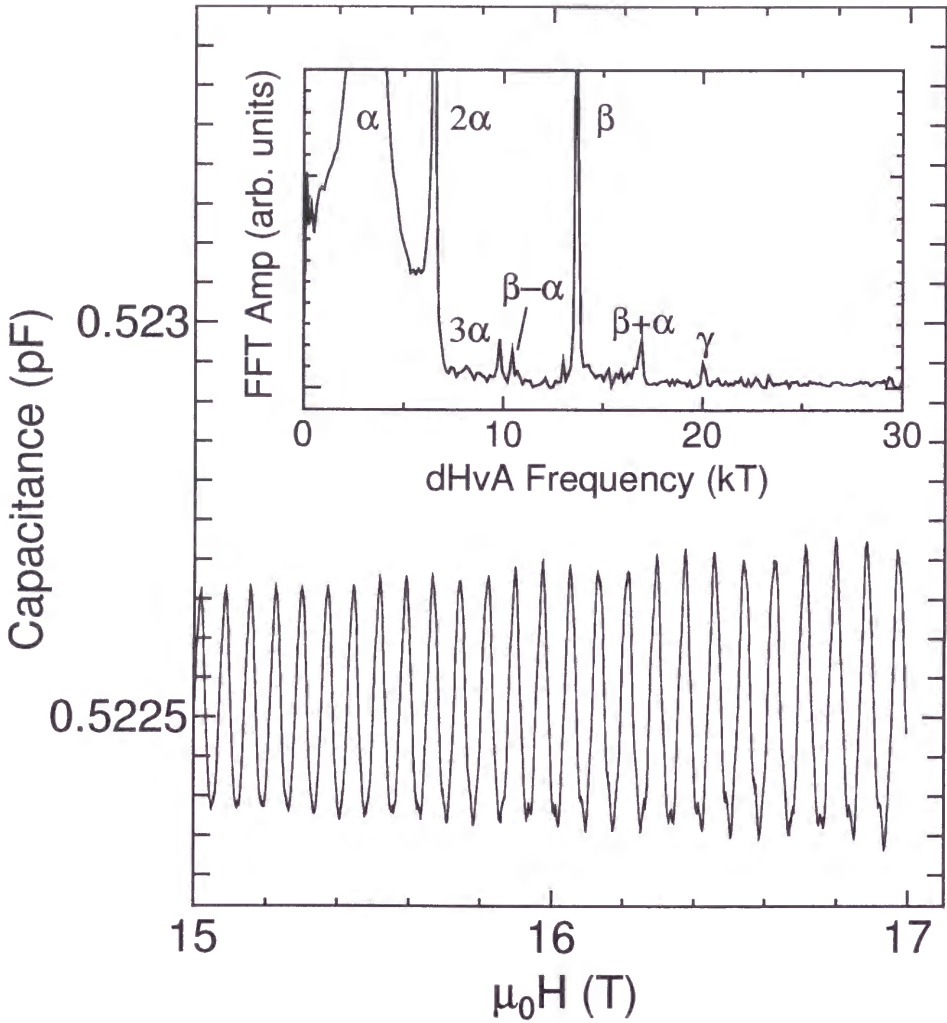
Figure 4.8: The oscillatory components of de Haas-van Alphen oscillations observed in the magnetic torque of Sr_2RuO_4 at 0.3 K and $\theta=24°$. The inset shows the FFT spectrum of the oscillations.
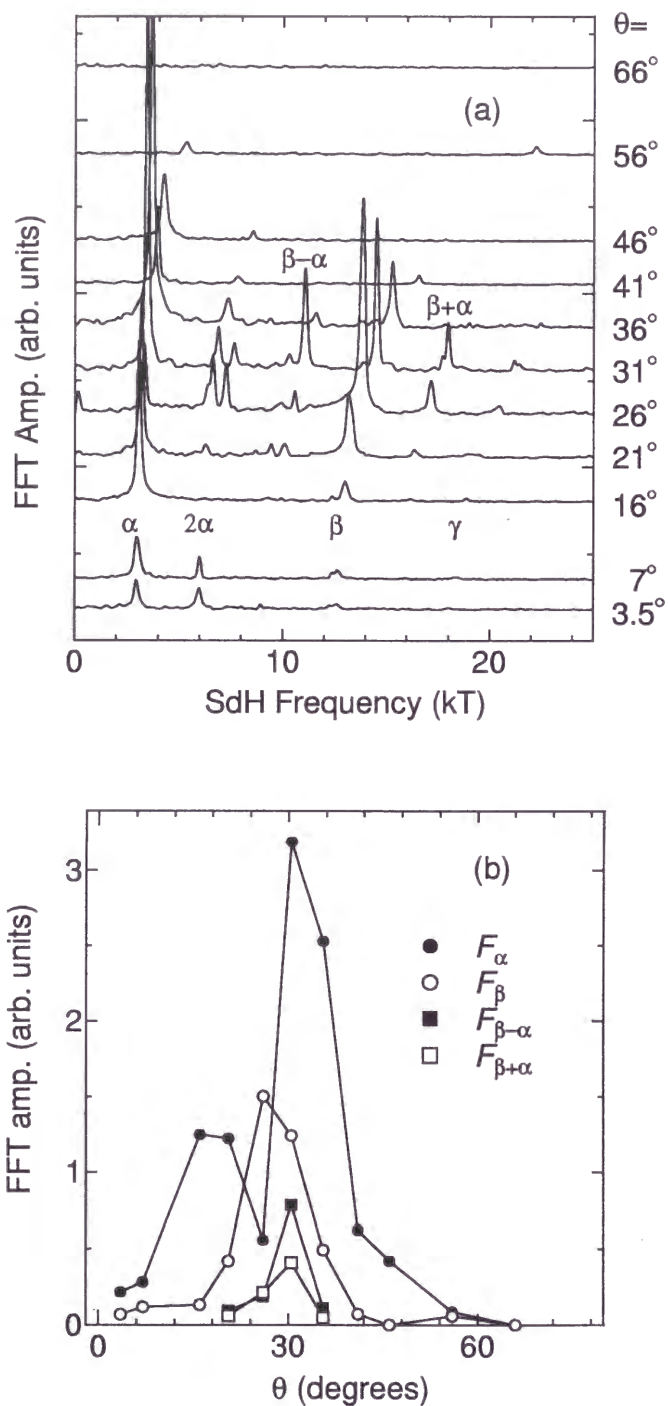
Figure 4.9: (a) FFT spectra of the oscillations for various θ values. Baselines of the curves are shifted vertically. (b) The angle dependence of the oscillation amplitude for the frequencies, F_α, F_β, $F_{\beta-\alpha}$ and $F_{\beta+\alpha}$, derived from Fig. 4.9(a).

Figure 4.10: Angle-dependent magnetoresistance oscillations observed in the inter-plane resistivity of Sr_2RuO_4 at 1.5 K under a magnetic field of 15 T.
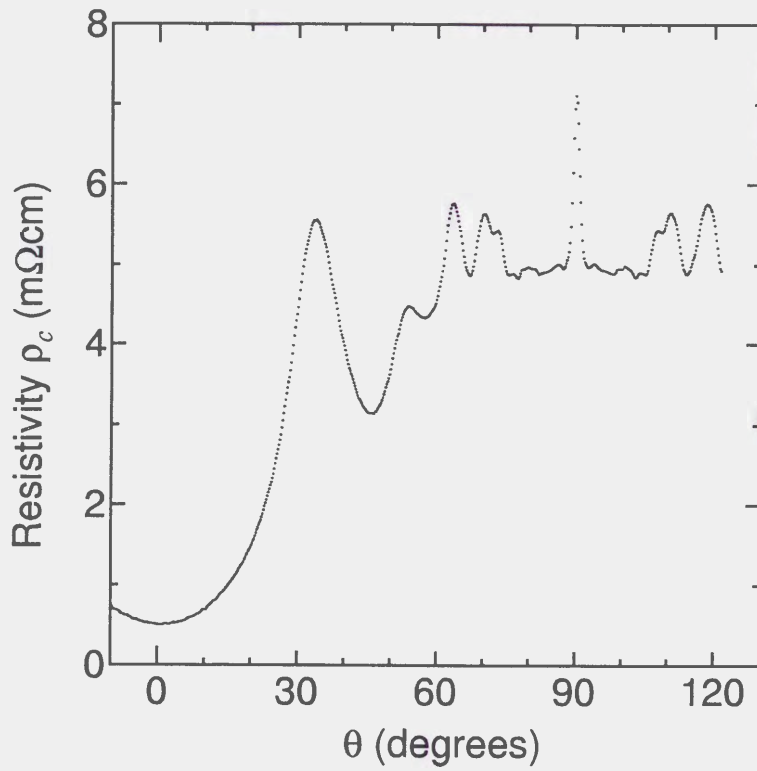
the oscillations. As a result, the oscillation amplitude for the frequencies F_α and F_β increases significantly. Such an enhancement in the oscillation amplitude of the fundamental frequencies near the first AMRO peak was reported previously [49]. The enhancement of the oscillatory components with $F_{\beta\pm\alpha}$ is the central issue of the present section.

The origin of $F_{\beta\pm\alpha}$ cannot be ascribed to the MB effect due to the following reasons. First, the closed orbit corresponding to $F_{\beta-\alpha}$ is prohibited in a MB process according to the theory of Falicov and Stachowiak [65] based upon the network model. In addition, even though $F_{\beta+\alpha}$ is allowed in the MB process, the carriers on a cyclotron orbit have to overcome a large energy gap in order to break through to the orbit on a different band. The criterion for the MB in this case is given by $\hbar\omega_c > E_g^2/\epsilon_F$, where ω_c is the cyclotron frequency and E_g is the energy gap between relevant bands. Since the α and β branches are completely isolated in the reciprocal space, however, the $\hbar\omega_c$ in the present study is in the order of the resolution of the band calculation and significantly smaller compared to the barrier height. Thus the MB effect is ruled out. The possibility of $F_{\beta\pm\alpha}$ due to the MI effect is also ruled out as discussed later based upon the temperature dependence of the oscillation amplitude for $F_{\beta\pm\alpha}$.

4.3.2 Chemical potential oscillations (CPO)

The thermodynamic potential Ω for a constant chemical potential μ and the free energy F for a constant electron number N are give by

$$\Omega \;=\; F - N\mu, \tag{4.4}$$

$$F \;=\; E - TS, \tag{4.5}$$

respectively, where E is the internal energy and S is the entropy of the system. The magnetization for each case is derived as

$$M(\mu, H) = -\left(\frac{\partial \Omega}{\partial H}\right)_\mu, \quad M(N, H) = -\left(\frac{\partial F}{\partial H}\right)_N. \qquad (4.6)$$

For constant-μ case, total magnetization from all the extremal orbits can be obtained simply by adding each contribution, that is,

$$M(\mu, H) = \sum_i M_i(\mu, H) = \sum_i \left(-\frac{\partial \Omega_i}{\partial H}\right)_\mu, \qquad (4.7)$$

where i denotes the i-th orbit, while for constant-N case, $M(N, H)$ cannot be obtained by such simple superposition, because $(\partial F_i / \partial H)$ for each band cannot be calculated independently. In metals like Sr_2RuO_4, the carrier number N is considered to be constant under a magnetic field and $M(N, H)$ should be calculated. However, due to the difficulty in deriving the analytical formulae, the calculation of quantum oscillations is usually carried out based upon an assumption of constant chemical potential μ to derive the Lifshitz-Kosevich (LK) formula [42].

The difference between $M(\mu, H)$ and $M(N, H)$ is found to be negligibly small for 3D FSs. Recently, however, it has been pointed out independently by Alexandrov and Bratkovsky [63] and by Nakano [64] that for a multi-band system with 2D cylindrical FSs, the oscillatory behavior calculated under constant-μ and constant-N can be different. In the calculation under constant-N new oscillatory components with frequencies of the sum and difference of fundamental frequencies will appear in addition to fundamental frequencies, even in the absence of the MB effect or the MI effect, while that under constant-μ, only fundamental frequencies will appear. These new frequencies are associated with a change in the chemical potential μ due to Landau quantization and is called the chemical potential oscillations (CPO): the carriers transfer between independent FSs so as to maintain a constant

N, and consequently the relevant density of states on the FS is notably modulated by the transferred electrons from other FSs. It should be noted that this effect becomes more pronounced when the system becomes purely 2D, otherwise the part of the FS not contributing to the oscillations behaves as a reservoir of the carriers, which serves to smear out the effect of the carrier exchange between the relevant bands.

For a Q2D electronic system, the energy dispersion $\epsilon_i(\boldsymbol{k})$ of a FS branch i is given by

$$\epsilon_i(\boldsymbol{k}) = \frac{\hbar^2}{2m_i^*}(k_x^2 + k_y^2) - 2t_{\perp,i}\cos(d_i k_z), \qquad (4.8)$$

where m_i^* is the effective mass, and $2\pi/d_i$ is a modulation period of the cylindrical FS in the k_z direction. When a magnetic field is applied, the energy level is discretized to each Landau level with a separation of $\hbar\omega_{c,i}$. Due to the existence of $t_{\perp,i}$, however, the cross-sectional area of the FS varies in the inter-plane direction, resulting in a broadening of each Landau level with $2t_{\perp,i}J_0(d_i k_{\mathrm{F},i}\tan\theta)$ depending on the field direction θ, where J_0 is Bessel function of 0-th order and $k_{\mathrm{F},i}$ is the Fermi wave number. The broadening of Landau level decreases with increasing θ, and the energy spectrum becomes perfectly 2D when $J_0(d_i k_{\mathrm{F},i}\tan\theta) = 0$; the angles satisfying this condition are called the Yamaji angles [40]. As shown in Section 4.1, the $d_i k_{\mathrm{F},i}$ value is almost the same for the α and β branches in Sr_2RuO_4 according to the band calculation [28], indicating the coincidence of the Yamaji angles for the α and β branches. This is consistent with the experimental observation that the oscillation amplitude of F_α and F_β are most prominent at similar angles around $\theta=30°$ as shown in Fig. 4.9(b). The simultaneous satisfaction of a pure 2D FS for the α and β branches realizes the preferred condition for the CPO. This fact is consistent with the observation of the enhanced oscillations with the sum and difference frequencies $F_{\beta\pm\alpha}$ around $\theta=30°$. The $t_\perp$'s evaluated by quantum oscillations [66] are 1.2 K and 17 K for the α and

β branches, respectively. On the other hand, the evaluated $\hbar\omega_{c,i}$ at 15 T and $\theta=0°$ are 5.8 K and 2.6 K for the α and β branches. This shows that for the α branch $\hbar\omega_{c,\alpha} > 2t_{\perp,\alpha}J_0(d_\alpha k_{F,\alpha})$ is achieved even at $\theta=0°$, while for the β branch $\hbar\omega_{c,\beta} < 2t_{\perp,\beta}J_0(d_\beta k_{F,\beta})$ at $\theta=0°$. In other words, for the β branch, the broadening of each Landau level cannot be neglected at $\theta \sim 0°$. Therefore, it is essential to orient the sample in the Yamaji angle direction to obtain prominent quantum oscillations with $F_{\beta\pm\alpha}$.

	β (electron)	α (hole)	γ (electron)
mass (m)	1	0.43	2
frequency (F)	1	0.24	–
k_F	1	0.49	–
$\Delta k_F/k_F$	1.3%	0.34%	–
d	$c/2$	c	–
Yamaji angle	30.5°	31°	–

Table 4.1: Ratios and values of band parameters of Sr_2RuO_4 adopted in the numerical calculation [67].

Recently, a numerical calculation of quantum oscillations, using realistic band parameters appropriate for Sr_2RuO_4 (Table 4.1) was carried out by Nakano [67]. First, chemical potential μ is obtained numerically from $N=-(\partial\Omega(\mu,H)/\partial\mu)_H$, and then it is inserted to the left equation of eq. (4.6) :

$$M(N,H) = M(\mu(N,H),H). \tag{4.9}$$

Note that instead of the standard LK formula (eq. (2.23)), $M_i(\mu,H)$ for Q2D model, represented by

$$M_i(\mu,H) = \sum_{p=1}^{\infty} 2(-1)^p R_T^i\, R_D^i\, R_S^i\, R_N^i\, \sin\left(2\pi p\left(\frac{F_i}{H}-\frac{1}{2}\right)\right), \tag{4.10}$$

$$R_N^i = \frac{\rho_0^i \epsilon_F^i \hbar e \cos\theta}{2\pi p m_i^*} \cdot J_0\left(2\pi p\frac{2t_{\perp,i}J_0(d_i k_F^i \tan\theta)}{\omega_i}\right), \tag{4.11}$$

is adopted, where R_X (X = T, D, S) are the same reduction factor as eqs. (2.24)-(2.26), ρ_0 is the density of states without a field, and R_N^i is a damp-
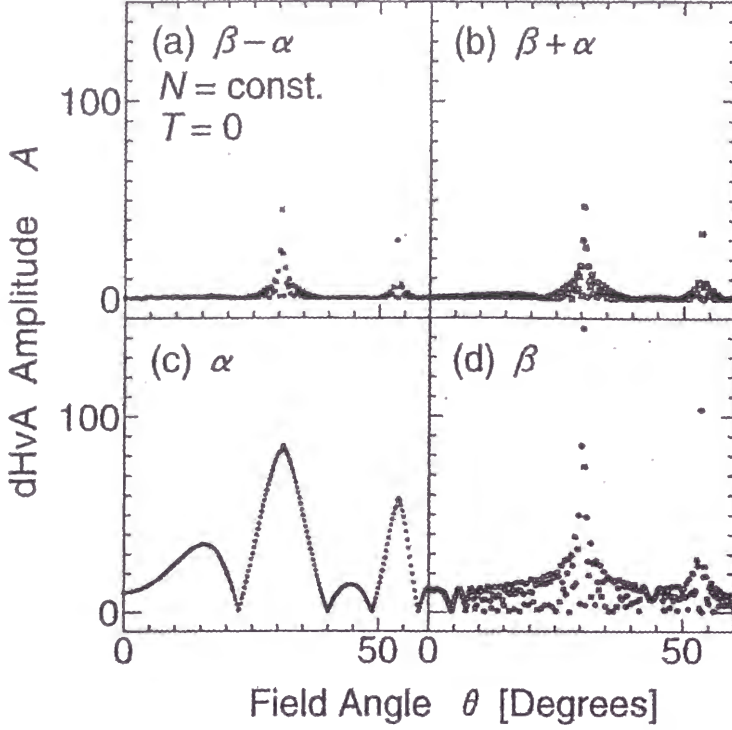
Figure 4.11: Calculated angle dependence of the oscillation amplitude for (a) $F_{\beta-\alpha}$, (b) $F_{\beta+\alpha}$, (c) F_{α}, and (d) F_{β} without any damping effect assuming that N is constant [67].

ing factor relevant to small warping of a Q2D FS. The α and β branches are quantized, while the γ branch is not quantized to be regarded as the background density of states, which works to smear out the effect of CPO. The calculated angle dependence of each oscillation amplitude without any damping effect is shown in Fig. 4.11. The results appear to be consistent with experimental results such as the emergence of $F_{\beta\pm\alpha}$ at $\theta \simeq 30°$. Although the second strongest intensity of $F_{\beta\pm\alpha}$ at $\theta \sim 55°$ was not observed experimentally, the intensity is considered to be smeared out by finite temperature and/or a certain amount of impurity in the real experiments.
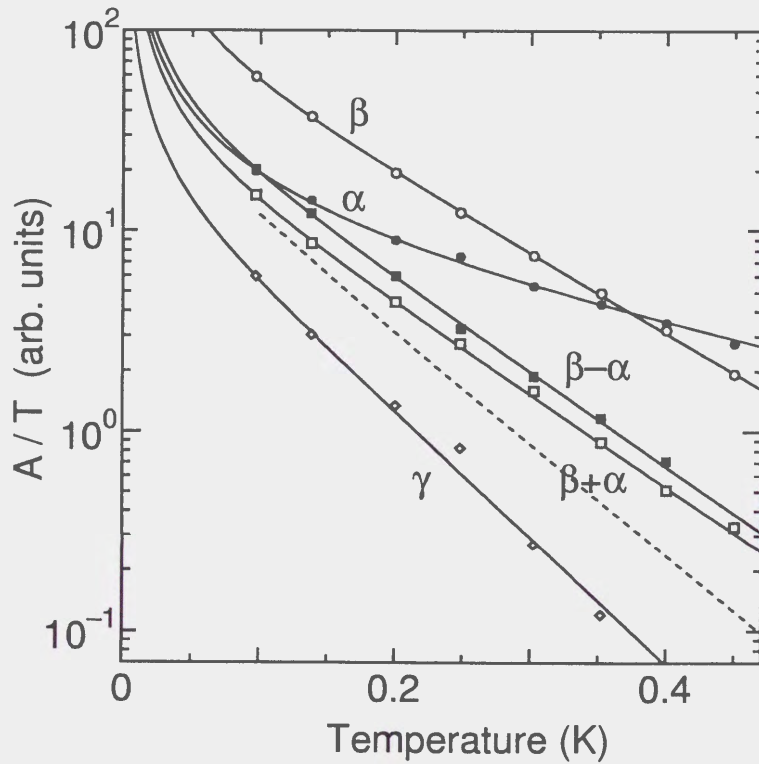
Figure 4.12: Temperature dependence of the oscillation amplitude (A) divided by temperature (T) for all the frequencies. Solid lines are curves fitted with the Lifshitz-Kosevich formula. The broken line curve is that obtained assuming an effective mass of $m_\beta + m_\alpha$. The slope in the higher temperature region is proportional to the effective mass.

4.3.3 Effective mass

Figure 4.12 shows the temperature dependence of the oscillation amplitude at $\theta=32°$. The slope in the higher temperature region is proportional to the effective mass according to the LK formula. The evaluated effective masses are $m_\alpha=4.2m_0$, $m_\beta=10.3m_0$, $m_\gamma=16.3m_0$, $m_{\beta-\alpha}=12.2m_0$ and $m_{\beta+\alpha}=11.9m_0$. It should be noted that $m_{\beta\pm\alpha}$ do not match the sum or difference of the effective masses of the α and β branches.

When the oscillations for the α and β branches are prominent, the MI effect [42] giving the oscillatory components with $F_{\beta\pm\alpha}$ can be promoted. This effect is brought about via a feedback effect of the magnetization M associated with the applied magnetic field H. In this case the effective mass of the oscillations with $F_{\beta\pm\alpha}$ will be given by $m_\beta + m_\alpha$, due to a multiplication factor for each temperature reduction factor. On the other hand, the apparent mass relevant to the CPO is not necessarily a simple sum of the masses of the constituent branches according to the calculated results [67]. The experimental results shown in Fig. 4.12 demonstrate that the sum of the masses of the α and β branches cannot explain the temperature dependence of the amplitude of the oscillations with $F_{\beta\pm\alpha}$. Instead, the results are in good agreement with the fore-mentioned calculation [67] using eq. (4.8) together with the band parameters appropriate for Sr_2RuO_4: the ratio of the effective masses are calculated to be $m_\beta^* : m_{\beta-\alpha}^* : m_{\beta+\alpha}^* = 1.00 : 1.20 : 1.14$ with a ratio of $m_\alpha/m_\beta = 0.43$, while those by the SdH effect are $m_\beta^* : m_{\beta-\alpha}^*$: $m_{\beta+\alpha}^* = 1.00 : 1.20 : 1.15$. This coincidence implies that the oscillations with $F_{\beta\pm\alpha}$ in Sr_2RuO_4 at the narrow angle region are ascribed to the CPO effect.

Finally, similar sum and difference frequencies observed in κ-(BEDT-TTF)$_2$Cu(NCS)$_2$ are mentioned. The field dependence of the inter-plane resistance of κ-(BEDT-TTF)$_2$Cu(NCS)$_2$ at 0.3 K is displayed in Fig. 4.13(a),
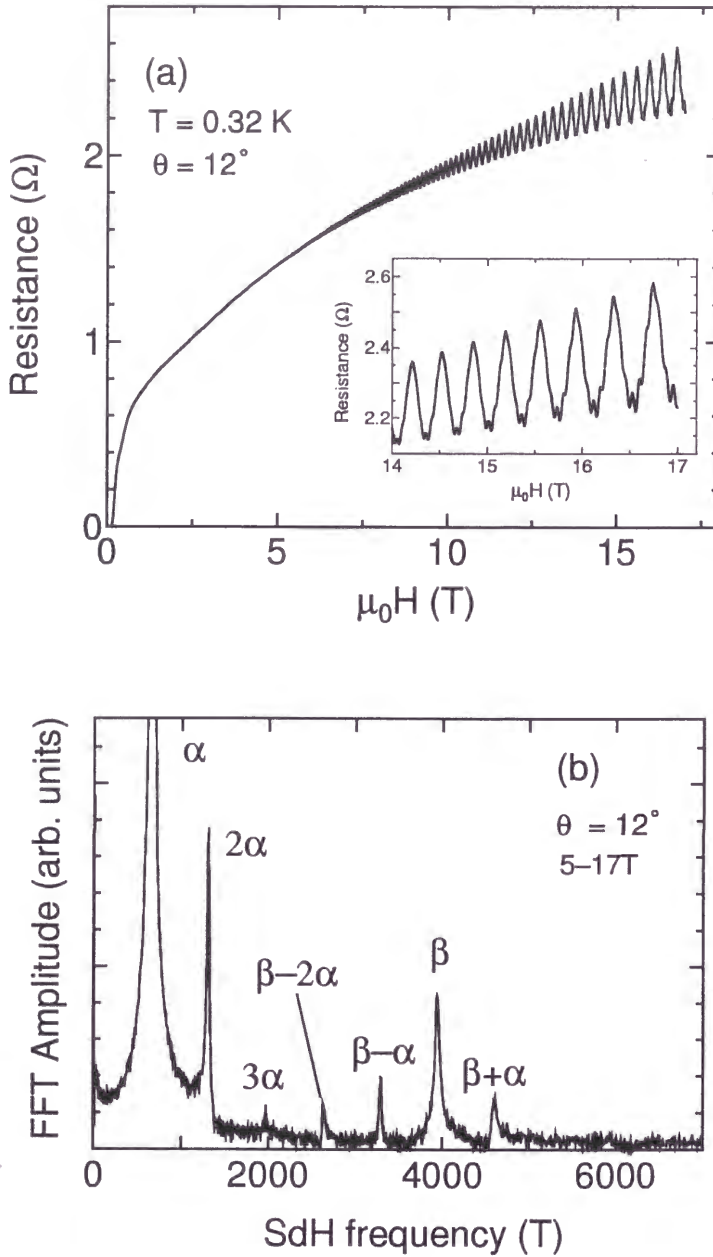
Figure 4.13: (a)Shubnikov-de Haas oscillations observed in the inter-plane resistance of κ-(BEDT-TTF)$_2$Cu(NCS)$_2$ at 0.32 K. The field direction is tilted by 12° from the normal direction to the conducting plane. The inset shows the high field behavior of the oscillations. Note that rapid oscillations due to the magnetic breakdown effect is visible above 14 T. (b)FFT spectrum derived from (a). In addition to the fundamental frequencies (F_α, F_β), combination frequencies ($F_{\beta-2\alpha}$, $F_{\beta\pm\alpha}$) are clearly recognized.

in which clear SdH oscillations are visible. In the FFT spectrum shown in Fig. 4.13(b), in addition to the fundamental frequencies of $F_\alpha = 659$ T and $F_\beta = 3940$ T, sum and difference frequencies are clearly recognized. Such combination frequencies have been reported in the dHvA effect [68, 69] and the SdH effect [70, 71, 72] in κ-(BEDT-TTF)$_2$Cu(NCS)$_2$ and the dHvA effect [73] in α-(BEDT-TTF)$_2$KHg(SCN)$_4$. Note that $F_{\beta+\alpha}$ is allowed but $F_{\beta-\alpha}$ is prohibited in the MB process. Therefore, it looks that $F_{\beta-\alpha}$ can be related to the CPO effect in a similar way as Sr$_2$RuO$_4$. However, the interpretation of $F_{\beta-\alpha}$ in organic conductors is not so straightforward: the effective mass of $F_{\beta-\alpha}$ is quite different between the dHvA effect and the SdH effect, indicating the different origin of $F_{\beta-\alpha}$.

For the FS of κ-(BEDT-TTF)$_2$Cu(NCS)$_2$ forming a MB network, the Stark quantum interference (SQI) effect [42, 74] giving $F_{\beta-\alpha}$ also becomes possible in transport measurements such as the SdH effect. The SQI effect occurs when there exists a possibility for the carries to take more than one path through the MB network to reach the same destination. The effective mass of $F_{\beta-\alpha}$ in the presence of the SQI effect is approximately given as $m^*_{\beta-\alpha} \sim m^*_\beta - m^*_\alpha$. This value is rather consistent with the effective masses of $m^*_\alpha = 2.7 m_0$, $m^*_\beta = 4.7 m_0$, and $m^*_{\beta-\alpha} = 2.9 m_0$, evaluated in the present study shown in Fig. 4.14 and those by others [71, 72]. Therefore, Harrison *et al.* [72] attempted to attribute the principal origin of $F_{\beta-\alpha}$ in the SdH effect of κ-(BEDT-TTF)$_2$Cu(NCS)$_2$ to the SQI effect rather than the CPO effect based on their numerical calculation. On the other hand, the effective mass of $F_{\beta-\alpha}$, derived by dHvA oscillations [69], is between m^*_β and $m^*_\beta + m^*_\alpha$, being consistent with the calculation assuming N is constant [75, 76]. Therefore, $F_{\beta-\alpha}$ in the dHvA effect seems to be due to the CPO effect. This view is also supported by the full-quantum-mechanical calculation with a realistic tight-binding model based on the band calculation [77, 78].
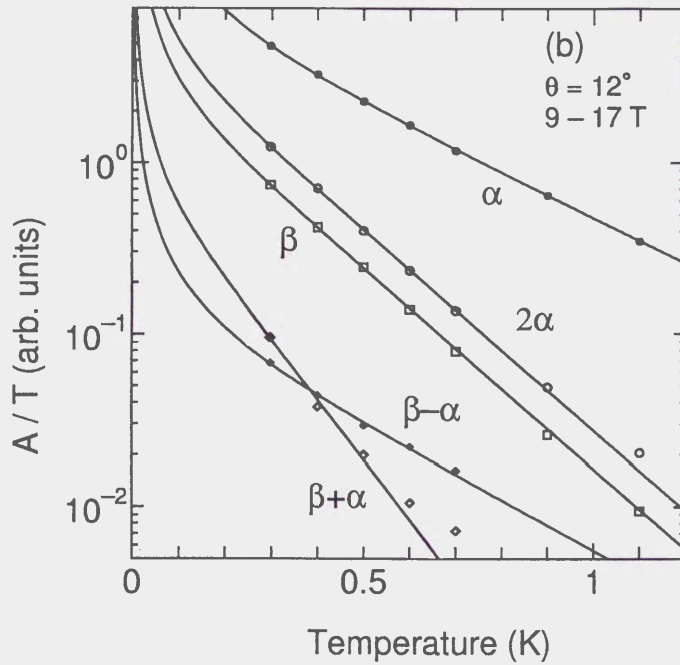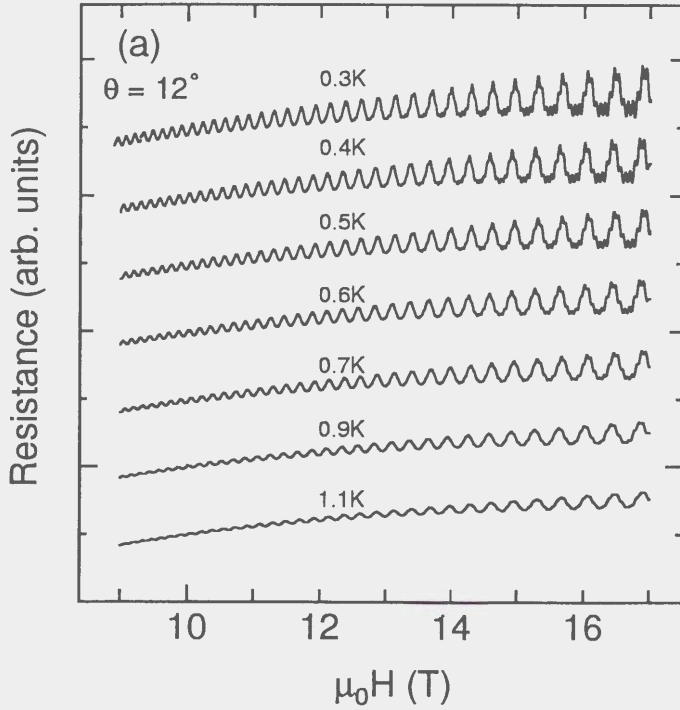
Figure 4.14: (a)the Shubnikov-de Haas oscillations in κ-(BEDT-TTF)$_2$Cu(NCS)$_2$ at different temperature. (b) Temperature dependence of the oscillation amplitude (A) divided by temperature (T). Solid lines are curves fitted according to the Lifshitz-Kosevich formula. The slope in the higher temperature region is proportional to the effective mass.

In contrast to κ-(BEDT-TTF)$_2$Cu(NCS)$_2$, Sr$_2$RuO$_4$ possesses isolated FSs in the reciprocal space. This situation makes it possible to discuss the results more clearly, since there is no possibility of the MB effect or the SQI effect. Moreover, another possibility of the MI effect can be ruled out according to the effective mass. To the best of our knowledge, the present results are the first demonstration of the clear CPO effect in Q2D conductors with independent cylindrical FSs.

4.4 Resistance peak under in-plane magnetic fields

4.4.1 Resistance peak in organic conductors

A resistance peak centered in the field direction parallel to the conducting plane was observed in organic conductors such as β-(BEDT-TTF)$_2$IBr$_2$ [57], κ-(BEDT-TTF)$_2$Cu$_2$(CN)$_3$ [79], and β-(BEDT-TTF)$_2$I$_3$ [80]. Although it was first attributed to the effect of open orbits [57], the origin has been found to be of topological one based upon the fact the peak width is invariant with the field strength. It should be also noted that the resistance peak exhibits anisotropy within the conducting plane, although the width of 4~5° is almost independent of the field orientation within the conducting plane as shown in Fig. 4.15. A numerical calculation assuming a simple energy band reproduced experimental features fairly well [80] but it was not able to explain the anisotropic behavior of the resistances peak within the conducting plane.

4.4.2 Resistance peak in Sr$_2$RuO$_4$

We found a similar peak in Sr$_2$RuO$_4$ in addition to the clear AMRO [60]. It exhibited more dramatic anisotropy within the conducting plane showing four-fold symmetry with regard to ϕ compared to that in organic conductors.
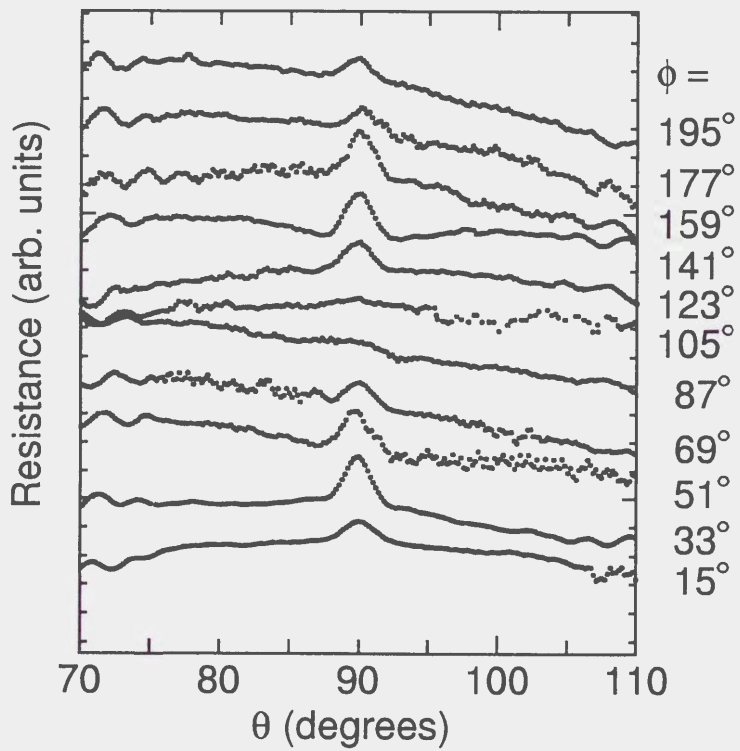
Figure 4.15: Polar-angle θ dependence of the resistance for κ-(BEDT-TTF)$_2$Cu$_2$(CN)$_3$ under 7.0 kbar for various ϕ values.

In this section, the resistance peak in Sr_2RuO_4 together with the transverse magnetoresistance are presented.

Figure 4.16 shows the angle dependence of the magnetoresistance in the vicinity of $\theta=90°$ for various ϕ values at 1.5 K and 15 T. The peak was most prominent in the direction of $\phi=45°$, while it becomes almost invisible near $\phi=0°$. The peak height increased with the field strength, but the peak width was invariant for the fixed ϕ, similar to the resistance peaks observed in the organic conductors [79, 57, 80].

The ϕ dependence of ρ_c values at the peak maximum ($\theta=90°$) and that at $\theta=88°$, away from the peak region, at 1.5 K under 15 T derived from Fig. 4.16 are shown in Fig. 4.17. The difference in the radial distance represents the peak height. The peak height at $\phi=45°$ reached 40% of the background magnetoresistance. The peak intensity varied drastically, exhibiting a four-fold symmetry with respect to ϕ.

It is interesting to know how ρ_c depends on the field strength at the peak positions. Figure 4.18 shows the field dependence of ρ_c for magnetic fields in the [110] ($\theta=90°,\phi=45°$) and [100] ($\theta=90°,\phi=0°$) directions, and that for a field tilted away from the [110] direction by 5° ($\theta=85°$, $\phi=45°$). The ratio $\Delta\rho_c/\rho_{c0}$ at 33 T ($\rho_{c0} \simeq 0.4$ mΩcm is the zero-field inter-plane resistivity at 1.5 K, and $\Delta\rho_c$ is the increment by the field) reached ~ 80 and ~ 20 under magnetic fields parallel to the [110] and [100] directions, respectively. The magnitude of the magnetoresistance as well as its anisotropy within the con-ducting plane, $\rho_c(H \parallel 110)/\rho_c(H \parallel 100) \sim 4$, was found to be huge compared to that of other layered conductors.

The temperature dependence of the magnetoresistance was negligible be-low 1.5 K, as demonstrated in Figs. 4.19(a) and 4.19(b). It remained almost constant under 10 and 20 T but showed a slight increase under 33 T toward zero temperature. These results imply that the increase in ρ_c with the in-
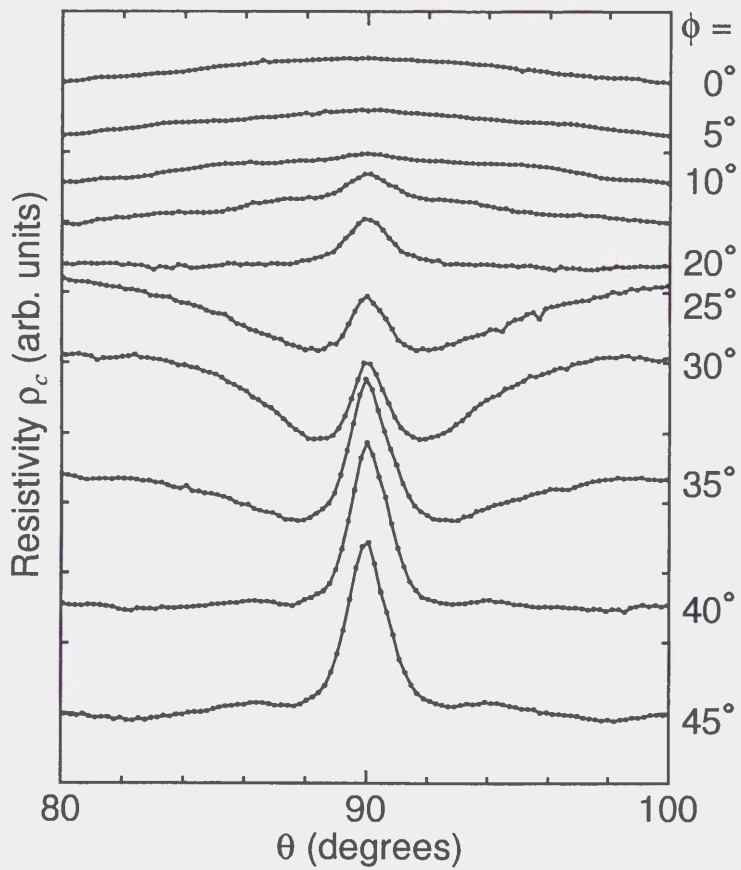
Figure 4.16: Angle dependence of the magnetoresistance in Sr_2RuO_4 in the vicinity of $\theta=90°$ for various ϕ values. The θ dependence of the resistivity for different ϕ is presented in arbitrary units by shifting with each other in the vertical direction.
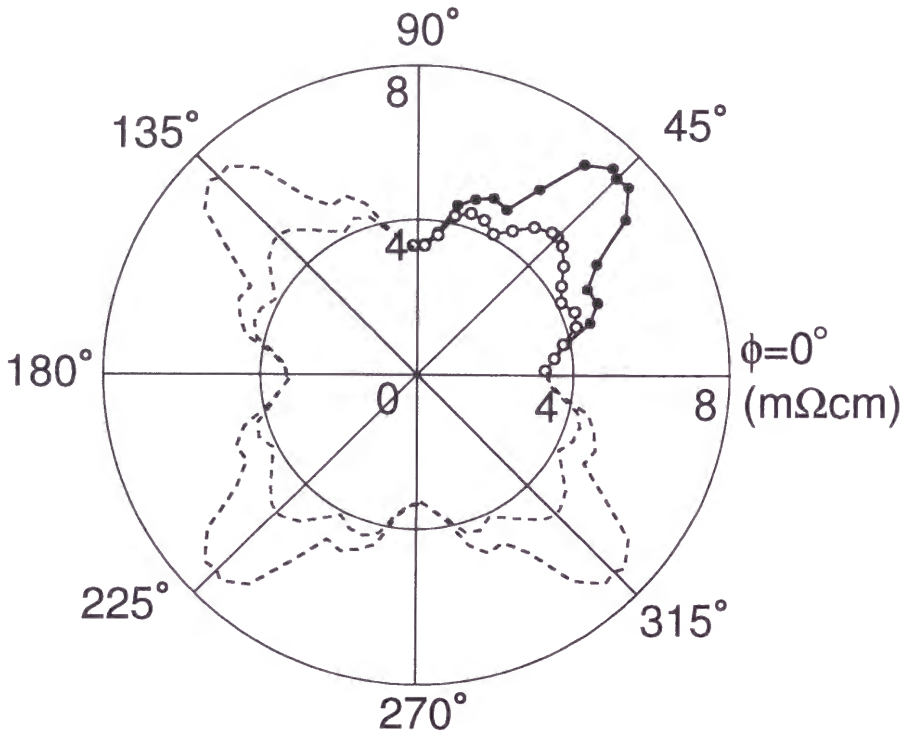
Figure 4.17: Polar plot of the ρ_c values at the peak maximum ($\theta=90°$) and at $\theta =88°$, away from the peak region, at 1.5 K and under 15 T, which are represented by solid and open circles, respectively. The difference in the radial distance for given ϕ corresponds to the peak height for each ϕ.
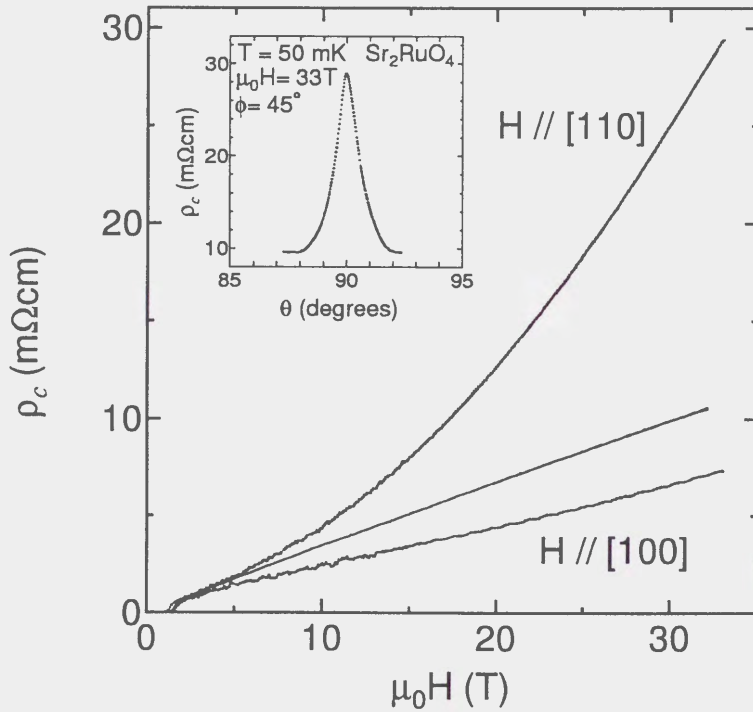
Figure 4.18: Field dependence of ρ_c of Sr_2RuO_4 at 50 mK for magnetic fields in the [110] and [100] direction and for a tilted field away from [110] direction by 5° ($\theta=85°$, $\phi=45°$) shown in the middle. The inset shows the polar-angle dependence of ρ_c near the parallel field orientation for $\phi=45°$ at 33 T and 50 mK. It is noted that the difference in the resistivity values between upper two curves nearly corresponds to the peak height.

crease in field was not a result of the confinement of orbital motion within the conducting plane [81] but that of the dynamics of metallic electrons.

As shown in Fig. 4.18, $\rho_c(H \parallel 100)$ was almost proportional to the field strength up to 33 T, while $\rho_c(H \parallel 110)$ showed superlinear dependence ($\sim H^{1.6}$) in the broad field region. It should be noted that $\rho_c(H \parallel 110)$ exhibited a sharp resistance peak centered in the parallel field direction ($\theta=90°$), as shown in the inset of Fig. 4.18, while $\rho_c(H \parallel 100)$ did not show such dependence. It is also noteworthy that ρ_c showed linear field dependence for the field slightly tilted from the [110] direction ($\theta=85°$), as shown by the middle curve in Fig. 4.18. The difference between $\rho_c(H \parallel 110)$ and $\rho_c(H \parallel 100)$ indicates that the field dependence of ρ_c at $\theta=90°$ strongly depends on whether or not the resistance peak exists.

4.4.3   Origin of the anisotropy in the resistance peak

As a probable origin of the resistance peak as shown in Fig. 4.16, a model that attempts to explain such peak structure on the basis of small closed orbits appearing at the side surface of a Q2D FS has been given by Hanasaki *et al.* [80]. They reproduced a resistance peak by numerical calculation of the conductivity tensor, in which an isotropically warped cylindrical FS represented by an energy dispersion $\epsilon(\boldsymbol{k})$ as

$$\epsilon(\boldsymbol{k}) = \frac{\hbar^2}{2m^*}(k_x^2 + k_y^2) - 2t_\perp \cos(dk_z) \tag{4.12}$$

was assumed, where m^* is the effective mass, $t_\perp$ is the inter-plane transfer integral, and d is the length that determines the modulation period of a Q2D FS in the k_z direction. The period d is equal to the inter-plane lattice parameter for a simple case, but is an integer multiple of the inter-layer distance $c/2=0.64$ nm for Sr_2RuO_4 as described in Section 4.1 because the unit cell contains two layers. Small closed orbits relevant to the resistance peak appear in a narrow angle region centered at $\theta=90°$ with the width $\Delta\theta$

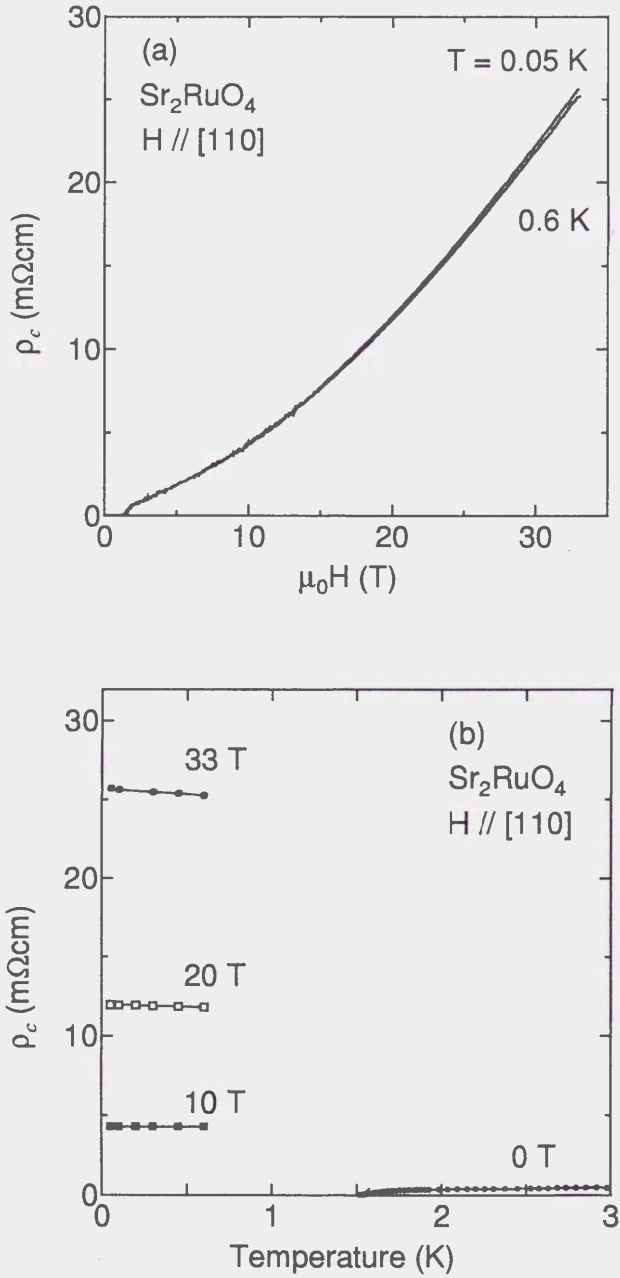Figure 4.19: (a) Field dependence of ρ_c of Sr_2RuO_4 for a magnetic field in the [110] direction at 0.05 K and 0.6 K. (b) Temperature dependence of ρ_c below 0.6 K under magnetic fields of 10, 20 and 33 T applied in the [110] direction. The temperature dependence in the absence of the magnetic field is shown as a reference.

as

$$\Delta\theta = \frac{4t_\perp d}{\hbar v_F}, \tag{4.13}$$

where v_F is the in-plane Fermi velocity. In this case, due to the isotropic energy dispersion within the conducting plane, the resistance peak is independent of the in-plane field orientation.

For Sr_2RuO_4, the peak characteristics change notably with ϕ, being inconsistent with the above-mentioned simple model. The anisotropic behavior can be partly ascribed to the squareness of the FS cross-section, but even if the FS is not a cylinder with a circular cross-section, small closed orbits can exist for magnetic fields applied in any direction within the conducting plane as long as $t_\perp$ is constant, and therefore, the resistance peak should appear in any in-plane direction. To explain the observed in-plane anisotropy, it is necessary to introduce an in-plane anisotropy in $t_\perp$, as described below.

When a magnetic field is applied precisely parallel to the conducting plane, most of the orbits become open, with the carriers oscillating back and forth in a direction normal to the conducting plane with the frequency [82] $\omega(k_x, k_y)$ as

$$\omega(k_x, k_y) = -\frac{eHd}{c_0\hbar}v_F(k_x, k_y)\sin\psi, \tag{4.14}$$

where $v_F(k_x, k_y)$ is the in-plane Fermi velocity at the FS specified by (k_x, k_y) within the conducting plane, and ψ is the angle between $\boldsymbol{H}$ and $\boldsymbol{v}_F(k_x, k_y)$. The carriers at the FS portion with $\psi \sim 90°$ are forced to move quickly along the cylindrical axis, and the time-averaged group velocity $\int_{-\infty}^{0} v_z(\boldsymbol{k}(t))e^{t/\tau}/\tau\, dt$ becomes small, contributing less dominantly to the inter-plane conductivity where $v_z = (1/\hbar)\partial\epsilon(\boldsymbol{k})/\partial k_z$ and τ is the scattering time. On the other hand, at the FS portion near $\psi \sim 0°$, in which $\omega(k_x, k_y)$ is significantly reduced, the carriers travel slowly in the k_z direction, and their group velocity has a finite value. The finite averaged value dominates the inter-plane conductivity within the limit of $\omega_c\tau \gg 1$. In other words, the magnetoresistance in the

high field applied parallel to the conducting plane is determined by the FS portion near $\psi \sim 0°$. Therefore, the anisotropic behavior of the inter-plane magnetoresistance at $\theta = 90°$ can be attributed to the local warping of the cylindrical FS, leading to the anisotropy of $t_\perp$.

Since there are three FS branches in Sr_2RuO_4, the question arises as to which FS branch is relevant to the resistance peak. Based upon the fact that the peak width is proportional to $t_\perp$ as represented by eq. (4.13), the estimated value of $t_\perp \sim 2$ K for the α branch [66] cannot explain the broad peak width of $\Delta\theta \sim 4°$ and the survival of the resistance peak even at 10 K, whereas the peak width corresponding to $t_\perp \sim 16$ K for the β branch is $\Delta\theta \sim 5°$, comparable to the observed peak width at $\phi = 45°$. Thus, we consider that the feature is dominated by the β branch, although minor contributions from the α branch cannot be ruled out.

The in-plane anisotropy of $t_\perp$ was previously proposed by Hill [83] to explain the cyclotron resonance in organic conductors by assuming $(d_{xx}+d_{yy})$-type symmetry. For Sr_2RuO_4, the prominent peak for the field in the [110] direction indicates that the β branch is most corrugated in this direction, while the absence of a resistance peak in the [100] direction is due to the absence of small closed orbits in this direction. This result is supported by dHvA effect by Bergemann et $al.$ [61]: they obtained a similar results with regard to the warping pattern of the β branch based on the angle dependence of the beat frequency. However, the anisotropy of $t_\perp$ should not be too prominent, otherwise AMRO pattern depends notably on ϕ in contrast to the observed one.

4.4.4 Field dependence of the inter-plane resistivity ρ_c

Concerning the inter-plane resistivity for a magnetic field along the conducting plane, a linear field dependence in a certain field region has been

proposed independently by Lebed *et al.* [84], Peschansky [85] and Schofield *et al.* [86]. They calculated the inter-plane resistivity of a Q2D metal under in-plane magnetic fields on the basis of the Bloch-Boltzmann equation. Due to open orbits, a linear field dependence in the intermediate field range $(1 < \omega_c \tau < \sqrt{\frac{\epsilon_F}{t_\perp}})$ followed by quadratic behavior in the high field limit $(\omega_c \tau > \sqrt{\frac{\epsilon_F}{t_\perp}})$ was found for a simple energy band represented by eq. (4.12). Note that the effect of small closed orbits were not taken into account in these calculations. A similar result has been obtained by Moses and McKenzie [87] for a weakly incoherent transport model, though a crossover to quadratic behavior was not shown.

Taking into account that $\omega_c \tau$ reaches ~ 4 at 33T and 50 mK while $\sqrt{\frac{\epsilon_F}{t_\perp}}$ is greater than than 10 for the β branch, the linear field dependence is expected to be up to 33 T for both $\rho_c(H \parallel 100)$ and $\rho_c(H \parallel 110)$. Indeed, $\rho_c(H \parallel 100)$ depends almost linearly on the field strength up to 33 T as recognized in Fig. 4.18, which is consistent with the above-mentioned models. Whereas, a superlinear field dependence was observed for $\rho_c(H \parallel 110)$, which showed the sharp resistance peak. It is not likely that this result reflects the high field behavior, since the condition $\sqrt{\frac{\epsilon_F}{t_\perp}} < \omega_c \tau$ showing a quadratic field dependence is not satisfied. The uncertainty in $t_\perp$ cannot reduce the value of $\sqrt{\frac{\epsilon_F}{t_\perp}}$ below that of $\omega_c \tau$ even if we take into account the anisotropy in $t_\perp$. Hence, the difference between $\rho_c(H \parallel 110)$ and $\rho_c(H \parallel 100)$ cannot be understood in the framework of the above theories [84, 85, 86], and another explanation is needed. It should be noted that $\rho_c(H \parallel 110)$ with the superlinear dependence showed a peak at $\theta=90°$, while $\rho_c(H \parallel 100)$ did not. A similar relation is also demonstrated by the difference between $\rho_c(H \parallel 110)$ and ρ_c for a tilted field from the [110] direction ($\theta = 85°$), as shown in Fig. 4.18. This implies that the resistance peak is essential for the superlinear dependence. This result is incompatible with the Peschansky model [88] in which a linear field

dependence at the resistance peak is expected. On the other hand, the contribution from small closed orbits relevant to the resistance peak may explain the deviation from the linear field dependence.

4.5 Shubnikov-de Haas oscillations with unusual angle dependence in κ-(BEDT-TTF)$_2$Cu$_2$(CN)$_3$

4.5.1 Introduction

The organic superconductors κ-(BEDT-TTF)$_2X$ have attracted much attention due to high superconducting transition temperature T_c. These compounds consists of alternating stacks of highly conducting layers of dimerized BEDT-TTF molecules and insulating layers of counter anion. Among them, κ-(BEDT-TTF)$_2$Cu$_2$(CN)$_3$ is worth noting since it is considered as a Mott insulator, similar to κ-(BEDT-TTF)$_2$Cu[N(CN)$_2$]Cl, the organic superconductors with the highest T_c. However, the electronic structure of κ-(BEDT-TTF)$_2$Cu$_2$(CN)$_3$ was not known so far, and therefore we carried out FS measurements under pressure.

Figures 4.20 illustrates the temperature dependence of the inter-plane resistance for κ-(BEDT-TTF)$_2$Cu$_2$(CN)$_3$ at several pressure values. The temperature dependence shows that κ-(BEDT-TTF)$_2$Cu$_2$(CN)$_3$ is semiconductor at ambient pressure with an activation energy of $\sim$50 meV in the temperature region above 100 K and $\sim$30 meV below 100 K. Under pressure, a nonmetal-metal transition undergoes, followed by a superconductivity transition. The T_c, the highest value of which was 3.9 K under $\sim$0.6 kbar, decreased with the applied pressure value with $-dT_c/dP \sim$2-3 K/kbar. A resistance hump was shifted to higher temperature region with increasing pressure but it was fully suppressed when the sample was pressurized to 7.0 kbar. The residual resistance ratio reached 10^3 under pressure, indicating high quality of the
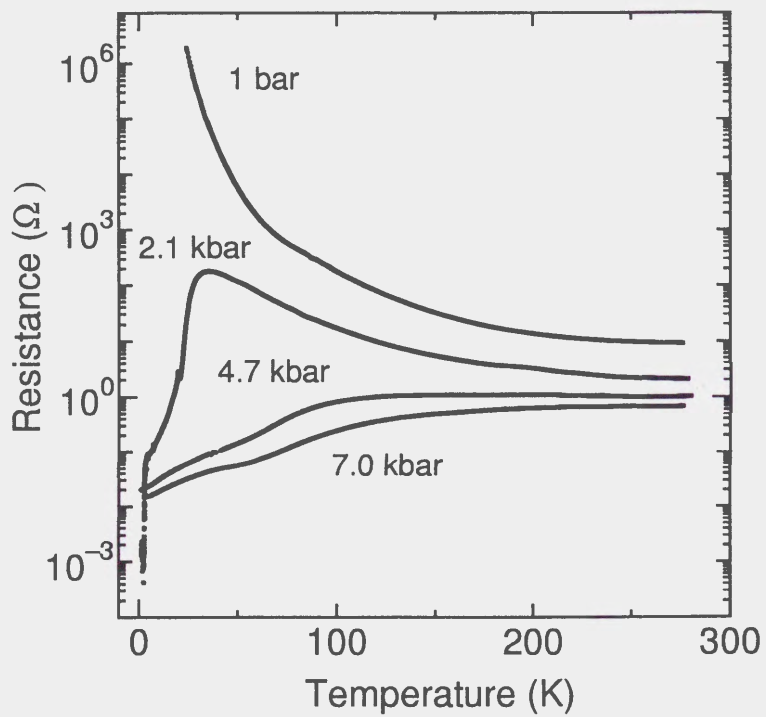
Figure 4.20: The temperature dependence of the inter-plane resistance for κ-(BEDT-TTF)$_2$Cu$_2$(CN)$_3$ at various pressure values.

used sample.

The electronic structure was investigated through the observation of AMRO under pressure [79]. The magnetoresistance showed clear oscillations as a function of the polar angle θ with $\tan\theta$ periodicity, and the observed FS, assigned to the β orbit, is rather consistent with the calculated [18] , as shown in Fig. 4.21.

Regarding SdH oscillations, however, new SdH oscillations with a small frequency of $\sim$120 T was observed in κ-(BEDT-TTF)$_2$Cu$_2$(CN)$_3$ under pressure in addition to the one consistent with the calculated FS [89]. The angle dependence of the frequency was inconsistent with that expected for a Q2D cylindrical FS. In this section, the anomalous behavior is discussed in relation to the origin of the slow quantum oscillations.

4.5.2   Results : Rapid and slow quantum oscillations

Figure 4.22 shows the magnetoresistance for the field perpendicular to the conducting plane under 7.6 kbar at 1.5 K. Two types of oscillations were distinguished: slow oscillations appearing above $\sim$8 T, and rapid oscillations superimposed on the slow one above $\sim$15 T. When the peak positions of these two oscillations were plotted in the scale of an inverse magnetic field, the linear relationship between them was found for respective oscillations. This fact indicates that these two oscillations can be identified as SdH oscillations. Fast Fourier transform (FFT) processing shows the oscillation frequencies of 120$\pm$20 T for the slow oscillations, and 3780$\pm$90 T for the rapid one as shown in Fig. 4.23. Any higher harmonic or linear combination of them was not observed. Another peak-like structure was found around $\sim$800 T in the FFT spectrum. We are tempted to assign the oscillatory component to the 2D hole-like α-orbit though the oscillation amplitude was rather weak and the frequency was slightly larger than the calculated value of 590 T.
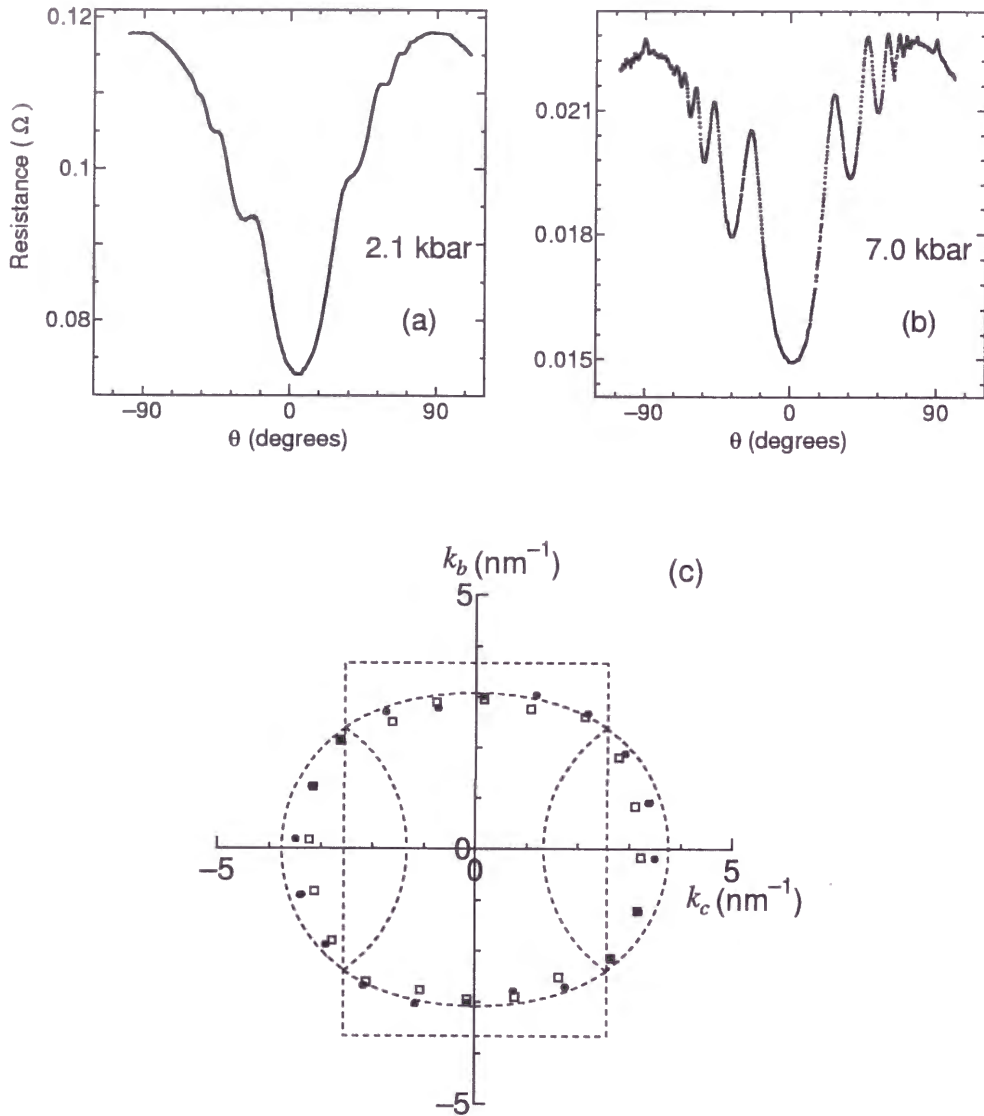
Figure 4.21: Polar-angle θ dependence of the magnetoresistance for κ-(BEDT-TTF)$_2$Cu$_2$(CN)$_3$ under (a) 7.0 kbar and (b) 2.1 kbar at 1.4 K under a magnetic field of 15 T. ϕ was set to be 195° for both pressure values. The broken lines displayed in (c) represent the first Brillouin zone and the FS contour calculated with room-temperature crystallographic data at ambient pressure. The solid circles and open squares denote the $k_H^{(max)}$ mapping determined by the AMRO periods under 7.0 and 2.1 kbar, respectively. (see text)
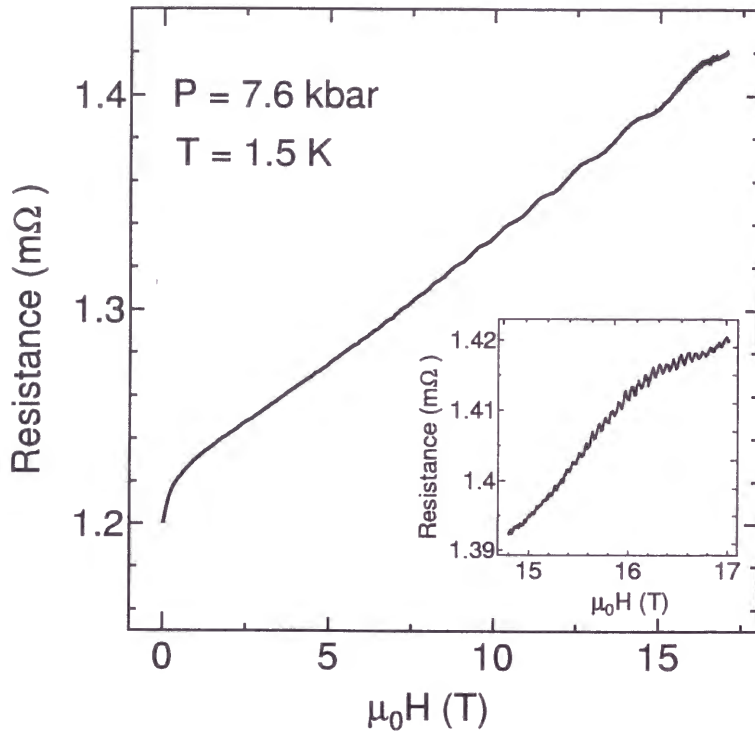
Figure 4.22: In-plane magnetoresistance of κ-(BEDT-TTF)$_2$Cu$_2$(CN)$_3$ at 1.5 K under 7.6 kbar. Magnetic field was applied perpendicular to the conducting plane. The inset shows the rapid oscillation observed in a high magnetic field range between 15 T and 17 T.
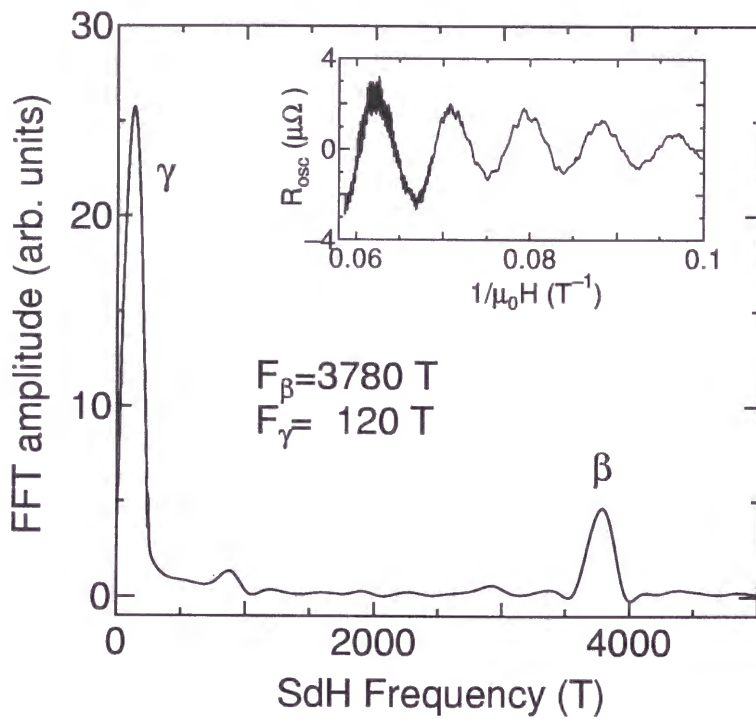
Figure 4.23: Fast Fourier transform (FFT) spectrum of the oscillatory component at 1.5 K under 7.6 kbar. The inset shows the oscillatory component obtained from Fig. 4.22 after subtraction of a smooth background.
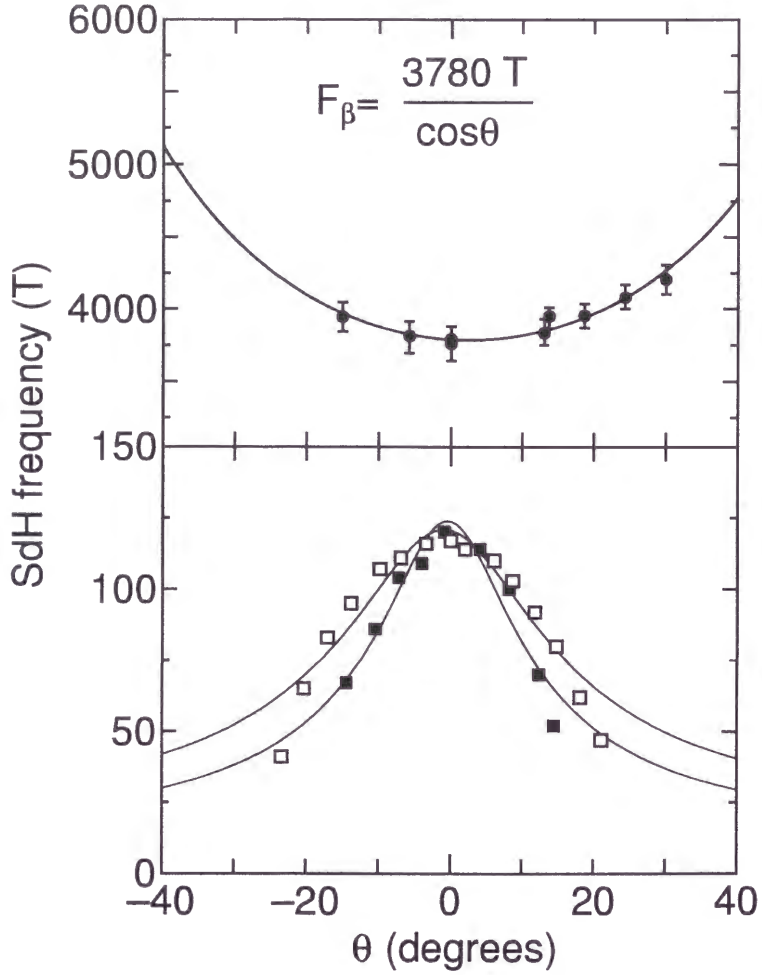
Figure 4.24: Polar-angle θ dependence of the SdH frequencies, F_β (upper case) and F_γ (lower case) observed under 7.6 kbar. A solid line for the upper case is represented by the denoted equation. In the lower case, solid and open rectangles denote the angle θ dependence for the azimuthal angles $\phi=150°$ and $90°$, respectively, and solid lines are the fit curve assuming an ellipsoidal FS (see text).

The oscillation frequencies varied with the polar angle θ as shown in Fig. 4.24. For a Q2D FS, the angle dependence of the frequency is given by

$$F(\theta) = \frac{F_0}{\cos\theta}, \tag{4.15}$$

where F_0 corresponds to the oscillation frequency at $\theta=0°$. For the rapid oscillations, the SdH signals observed in the angle region ranged from $-20°$ to $+30°$ obey the above $1/\cos\theta$ law. F_0 corresponds to 97% of the first Brillouin zone (BZ) area calculated by the room-temperature crystallographic parameters. The rapid oscillations correspond to the cylindrical FS called the β-orbit, realized by connecting the 1D and 2D parts. This result is in agreement with the FS obtained by AMRO at the same pressure.

In contrast to the rapid oscillations, the SdH frequency of the slow oscillations decreased with the magnetic field tilting from $\theta=0°$. Such behavior was confirmed for the field configurations with $\phi=0°$, $40°$, $90°$, and $150°$, where ϕ denotes the azimuthal angle measured from the c axis in the conducting plane. The slow oscillations for $|\theta|\geq20°$ were obscured due to the limited number of local maxima associated with the undulation as shown in Fig. 4.25. For instance, at $\theta=-23.4°$ ($\phi=90°$), its oscillation frequency was ~40 T and only three local maxima were observed. At higher angles with a smaller frequency, we cannot rule out the uncertainty in determining the field corresponding to the resistance peak, since the background magnetoresistance substantially changed with θ. It should be noted that the used magnetic field up to 17 T was not strong enough to cover the oscillations with a frequency of less than 30 T. The cross-sectional area corresponding to the slow oscillations at $\theta=0°$ was estimated to be 3.0% of the first BZ area, which is only one-fifth of that of the α-orbit. Hereafter the relevant orbit is designated as the γ-orbit.

From the temperature dependence of the oscillation amplitude, the effective mass can be derived according to $\ln(A/T)$ versus T relation [42] where
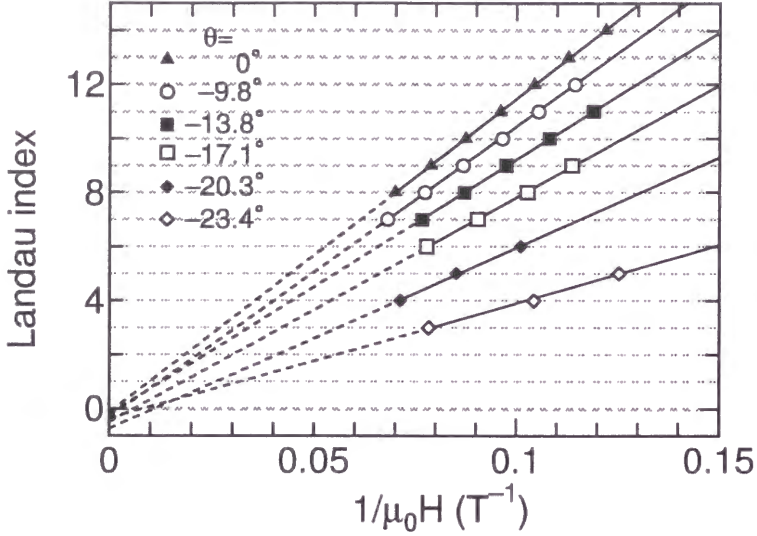
Figure 4.25: Landau index versus the inverse magnetic field giving a resistance peak for the slow oscillations at various polar angles θ for $\phi=90°$. The slope of the solid line provides the oscillation frequency.

A is the oscillation amplitude and T is temperature. The slow and rapid oscillations were observed up to $\sim$4 K and $\sim$2 K, respectively. The effective masses evaluated for the β- and γ- orbits at $\theta=0°$ were $m_\beta \simeq 4m_0$ and $m_\gamma \simeq 0.5m_0$, respectively, where m_0 represents the free electron mass.

4.5.3 Discussion

Similar slow oscillations with anomalous angle dependence were reported in β-(BEDT-TTF)$_2$IBr$_2$ [57]. The result was tried to be explained in terms of a multi-connected FS, where the cylindrical FSs were bridged with complicated thin channels [57]. In such a case, however, the azimuthal angle ϕ dependence should depend notably upon whether or not the plane formed by varying θ contains the bridging channels. Taking into account the relatively weak ϕ dependence and strong θ dependence, we can assume a flat ellipsoid with the shortest diameter along the normal to the conducting plane as a simple model. In this case, the angle dependence of the oscillation frequency, $F(\theta)$,

91

is represented as

$$\left(\frac{1}{F(\theta)}\right)^2 = \left(\frac{\cos\theta}{F_\perp}\right)^2 + \left(\frac{\sin\theta}{F_\parallel}\right)^2, \qquad (4.16)$$

where $F_\perp$ and $F_\parallel$ denote the oscillation frequency at angles $\theta=0°$ and $90°$, respectively. The ratio of $F_\perp/F_\parallel$ evaluated by the fitting are 6.4 and 4.7 for $\phi=150°$ and $90°$, respectively. The rapid decrease of the oscillation frequency is qualitatively explained based upon this simple model. However, a discrepancy of the experimental results cannot be neglected as shown in Fig. 4.24, indicating complexity of the FS. The presence of similar 3D FSs in θ-(BEDT-TTF)$_2$I$_3$ [90] was also reported.

Figure 4.26 shows the pressure dependence of the FS cross-sectional areas (S_γ, S_β) normalized by the value at 7.6 kbar for slow and rapid oscillations. The AMRO results giving the β-orbit are also displayed together. The pressure dependence for the β-orbit is rather consistent with the results for the other κ-type salts [91, 92]. On the other hand, the slow oscillations observed above 3.3 kbar shows the pressure dependence represented by $d \ln(S_\gamma)/dP=(4.5\pm0.9)\times10^{-2}$/kbar, several times larger than that for the β-orbit. This coefficient is rather large even if we take into account of an empirical tendency that the FS with a smaller cross-sectional area is more sensitive to the applied pressure. Then we consider that the strong pressure dependence is due to the difference in the origin between the γ-orbit and the β-orbit based upon the following fact. From the X-ray analysis, we found that there exist shorter contacts between a sulfur atom of BEDT-TTF molecule and a carbon or nitrogen atom in the anion layer than the sum of each van der Waals radius [93]. This suggests that if the energy levels of HOMO or LUMO of the atoms are close to the Fermi energy, a small but finite transfer matrix element between sulfur and carbon or nitrogen may result and form a small FS which is not predicted by the band calculation neglecting the inter-plane interaction. Such inter-plane interaction via the
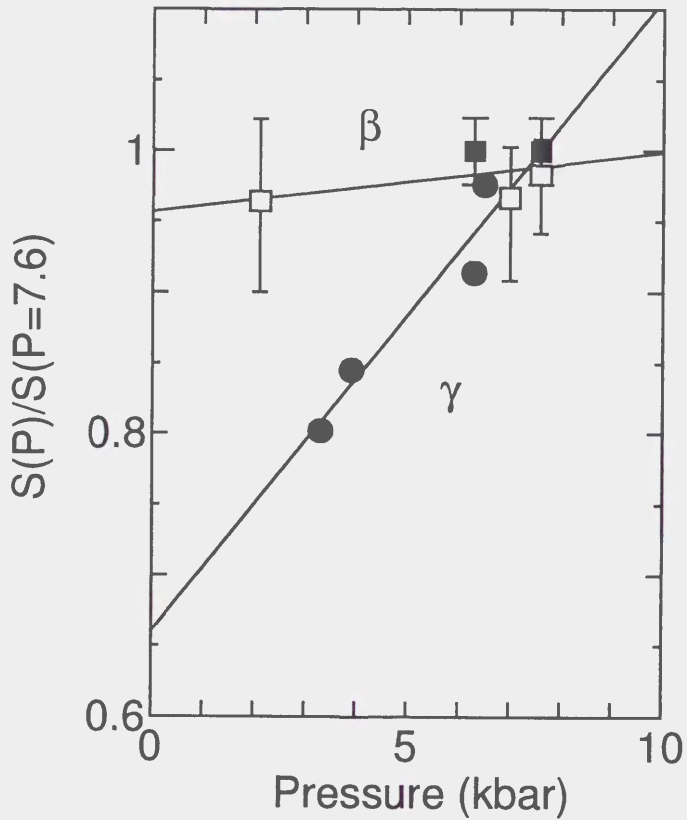
Figure 4.26: Pressure dependence of the cross-sectional areas normalized by the value at 7.6 kbar, which are obtained from the SdH oscillations corresponding to the β-orbit (solid rectangle) and the γ-orbit (solid circle), and from the AMRO measurement yielding the β-orbit (open rectangle). Solid lines show the result of least-square fitting.

anion layer can modify the energy dispersion in the inter-plane direction. The strong pressure dependence of the cross-sectional area of the γ-orbit may be understood in terms of the drastic enhancement of transfer integral due to the reduction of inter-plane spacing by pressure.

4.6 Conclusion of Chapter 4

We have demonstrated in Section 4.1 that AMRO can be observed in the layered oxide superconductor Sr_2RuO_4 as well as in organic conductors and the derived FS is found to be fairly consistent with the band calculation. In contrast to organic conductors, however, some ambiguity in the assignment are left due to the existence of independent three FS branches. Besides, the oscillation pattern of AMRO in the higher angle region deviates from the calculation based upon a simple energy band [41], although that in organic conductors looks very similar.

In addition to the AMRO, a sharp resistance peak exhibiting a notable dependence on ϕ was observed at $\theta=90°$ in Sr_2RuO_4, as presented in Section 4.3. To explain such anisotropic peak behavior, which is incompatible with the model based on a simple energy band, we point out that the anisotropy of $t_\perp$ should be included. This inclusion is supported by the fact that the magnetoresistance at $\theta \sim 90°$ will be strongly affected by the local shape of the FS. The most prominent peak at $\phi=45°$ suggests that the strongest corrugation of the β branch exists in the [110] direction. Moreover, the field dependence at the resistance peak was found to be different from that outside of the peak, suggesting a different origin of the magnetoresistance at the peak position from that at the background. In addition, these features imply that the anisotropy within the conducting plane cannot be neglected at all for a thorough understanding of Sr_2RuO_4.

Concerning quantum oscillations in Sr_2RuO_4, in Section 4.2 we reported

new oscillatory components with the sum and difference frequencies in the narrow angle region near the Yamaji angle satisfying the condition for the α and β branches to behave as almost 2D systems. Taking into account that such sum and difference frequencies have been theoretically pointed out in pure 2D systems, the angle dependence of those oscillation frequencies can be explained as a result of dimensional crossover from Q2D to 2D by angle inclination. Based upon the temperature dependence of the amplitude of the oscillations, the evaluated effective masses are not simple sum of respective effective massed, but are less than the summed value. Therefore, we conclude that the sum and difference oscillatory components appear as result of the CPO effect rather than the MI effect. The emergence of those frequencies implies that standard Lifshitz-Kosevich formula assuming a constant chemical potential μ breaks down and that physically strict treatment of the system assuming constant electron number becomes significant at such angles.

In Section 4.4 we presented a new type of slow quantum oscillations found in κ-(BEDT-TTF)$_2$Cu$_2$(CN)$_3$ under pressure. The angle dependence of the slow oscillations is anomalous in the sense that it has a sharp maximum at $\theta=0°$ regardless of the azimuthal angle ϕ, indicating that the relevant FS is not 2D but 3D. It is also noteworthy that the cross-sectional area corresponding to the slow oscillations is much more sensitive to pressure than the 2D cylindrical one. Taking account of the detailed X-ray experiments, these results imply that the electronic role of the anion layers cannot be neglected even if the fraction is not large. This requires that the paradigm of the conventional FS based upon the two-dimensionally aligned π-electron donor molecules should be extended to include the electronic contribution from the anion molecules.

Chapter 5

Two-Dimensional Superconductors under In-Plane Magnetic Fields

5.1 Upper critical field of κ-(BEDT-TTF)$_4$Hg$_{2.89}$Br$_8$ under in-plane magnetic fields

5.1.1 Introduction

The organic superconductor κ-(BEDT-TTF)$_4$Hg$_{2.89}$Br$_8$ is of a layered structure consisting of alternate stacking of the layers of BEDT-TTF molecules and those of Hg$_{2.89}$Br$_8$ anion. The π-electrons at the central part of BEDT-TTF molecules serve for the electrical conduction, while the insulating Hg$_{2.89}$Br$_8$ layers separate the conducting layers [16]. The spacing between the conducting sheets reaches 1.8 nm, resulting in pronounced two-dimensionality in the normal and superconducting states. The ratio of the in-plane coherence

	$\xi_\perp$ (nm)	$\xi_\parallel$ (nm)	$\xi_\parallel/\xi_\perp$
κ-(BEDT-TTF)$_4$Hg$_{2.89}$Br$_8$ [94]	0.8	17	21.3
κ-(BEDT-TTF)$_2$I$_3$ [95]	1.1	41	37
κ-(BEDT-TTF)$_2$Cu(NCS)$_2$ [96]	0.31	2.9	9.4
κ-(BEDT-TTF)$_2$Cu[N(CN)$_2$]Br [96]	0.58	2.3	4.0

Table 5.1: The in-plane ($\xi_\parallel$) and inter-plane ($\xi_\perp$) coherence length for κ-type BEDT-TTF salts.

length $\xi_\parallel$ to the inter-plane coherence length $\xi_\perp$ is presented in Table 5.1.

For BCS superconductors with singlet paring, superconductivity is suppressed by an excess of the spin polarization energy over the condensation energy. The boundary is known as the Chandrasekhar-Clogston limit or Pauli paramagnetic limit H_P [2, 3]. With regard to the organic superconductor κ-(BEDT-TTF)$_4$Hg$_{2.89}$Br$_8$, it was found that the upper critical field H_{c2} along the conducting plane exceeded the Pauli limit value calculated for a weak-coupling BCS model by more than two times as far as measurements were carried out in the magnetic field less than 15 T and in the temperature region higher than 1.5 K [94, 97], as shown in Fig. 5.1. In such field orientation, the orbital depairing effect is suppressed due to the heavy effective mass in the inter-plane direction, while the spin effect starts to play a key role in H_{c2}. The above interesting result urges to know the H_{c2} behavior at lower temperatures, that is, whether it exhibits either positive or negative curvature against the temperature variation, in relation to the Fulde-Ferrell-Larkin-Ovchinikov (FFLO) sate. In this section, we present a detailed H_{c2} study under magnetic fields applied parallel to the conducting plane and discuss possible mechanisms of the enhancement of H_{c2} in κ-(BEDT-TTF)$_4$Hg$_{2.89}$Br$_8$.

5.1.2   Results : Superconducting transition in magnetic fields

The temperature dependence of the in-plane resistance is shown in Fig. 5.2. During the measurement of the temperature dependence, resistance jumps were frequently observed upon cooling. In order to suppress such jumps we applied weak pressure to the sample by coating with grease, which may provide the pressure of $\sim$300 bar. The in-plane resistance decreased rather monotonically but the curvature varied slightly from sample to sample, presumably due to different cooling rates. The broadness in the transition to
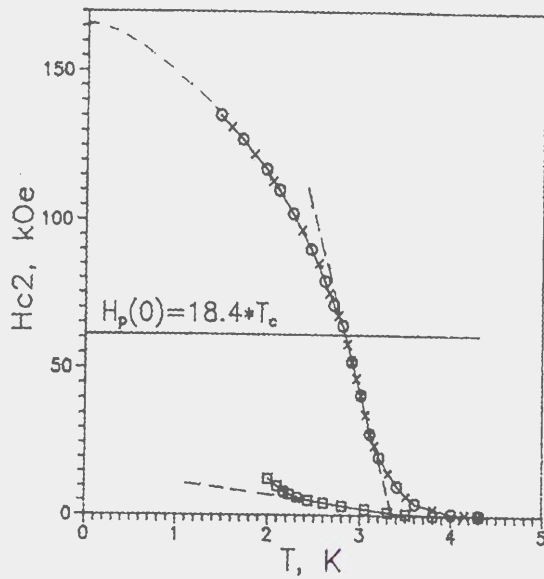
Figure 5.1: Temperature dependence of H_{c2} parallel to the conducting plane in κ-(BEDT-TTF)$_4$Hg$_{2.89}$Br$_8$ reported by Lyubovskii *et al.* [97].

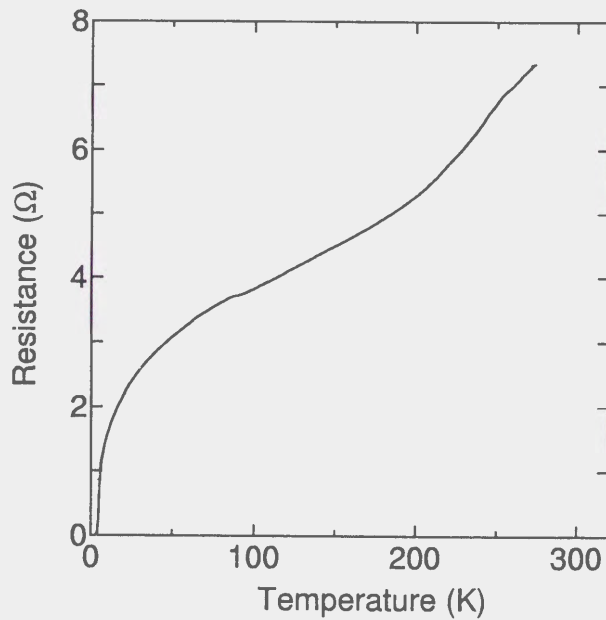Figure 5.2: The temperature dependence of the in-plane resistance of κ-(BEDT-TTF)$_4$Hg$_{2.89}$Br$_8$. The sample was coated with grease so as to suppress resistance jumps.

the superconducting state was somewhat varied depending on samples.

The two-dimensionality is demonstrated by the angle dependence of the in-plane resistance under a magnetic field as shown in Fig. 5.3. The superconductivity was suppressed for the magnetic field of 15 T applied perpendicularly to the superconducting plane but it revived in a wide angle region centered at $\theta=90°$.

Figure 5.4 shows the temperature dependence of the in-plane resistance in the transition region under magnetic fields applied parallel to the conducting plane with an accuracy of $\pm0.1°$. The results were obtained for the field direction along the b (short-diagonal) axis within the conducting plane and for the direction deflected by 45° from the b axis. In the absence of a magnetic field, the transition curve was rather broad and the transition width reached 2 K centered at 5.0 K. Presumably this is due to a superconducting fluctuation effect characteristic for low-dimensional superconductors and/or inhomogeniety of the samples. It is notable that the transition behavior shifted to the low temperature side almost parallel with increasing the magnetic field up to 15 T. We confirmed that a similar magnetic field dependence was observed for the field orientation along the a (long-diagonal) axis.

When a magnetic field was applied perpendicularly to the superconducting plane, the transition behavior became too dull to determine the characteristic temperature as shown in Fig. 5.5, as has been widely found in highly 2D systems due to the thermal fluctuation effect. Therefore it is misleading to determine the characteristic transition temperature for this field orientation. However, it should be noted that superconductivity was completely suppressed under the magnetic field of 15 T.

It is quite interesting to find up to how high field the superconductivity survives. For this purpose we carried out resistance measurements at 0.5 K
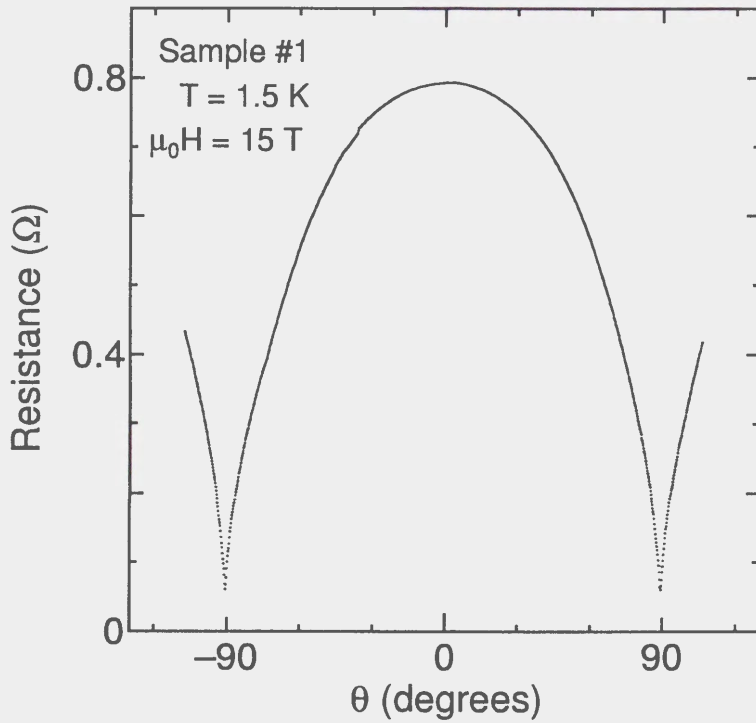
99

Figure 5.3: The angle dependence of the in-plane resistance under the magnetic field of 15 T measured at 1.5 K for sample #1. $\theta = 0°$ corresponds to the direction perpendicular to the layer plane while $\theta = 90°$ corresponds to the direction parallel to the plane along the b axis.
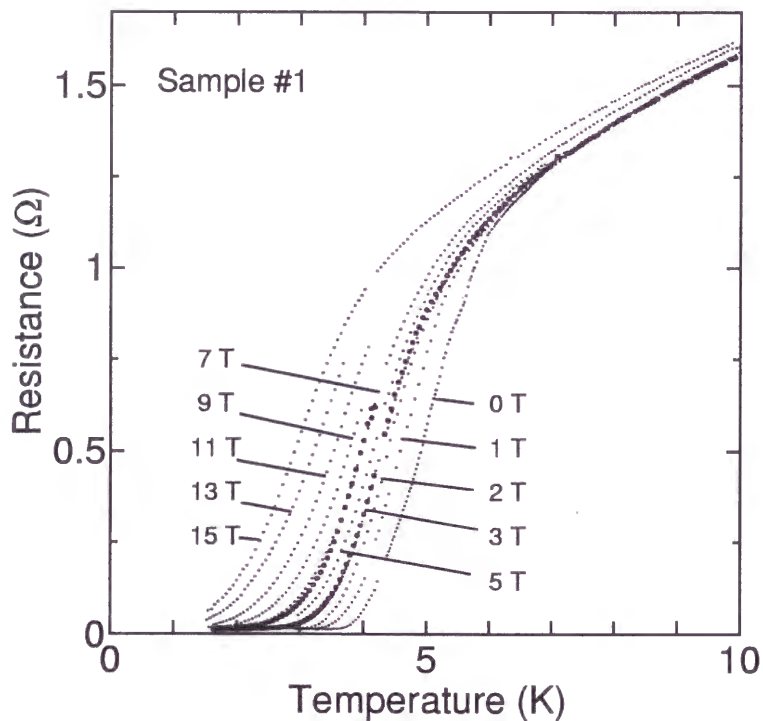
Figure 5.4: The temperature dependence of the in-plane resistance in the superconducting transition region for sample #1. The magnetic field up to 15 T was applied parallel to the conducting plane along the direction of the b (short-diagonal) axis of the sample (denoted by dots) and that along the direction deflected by 45° from the b axis (closed circles).
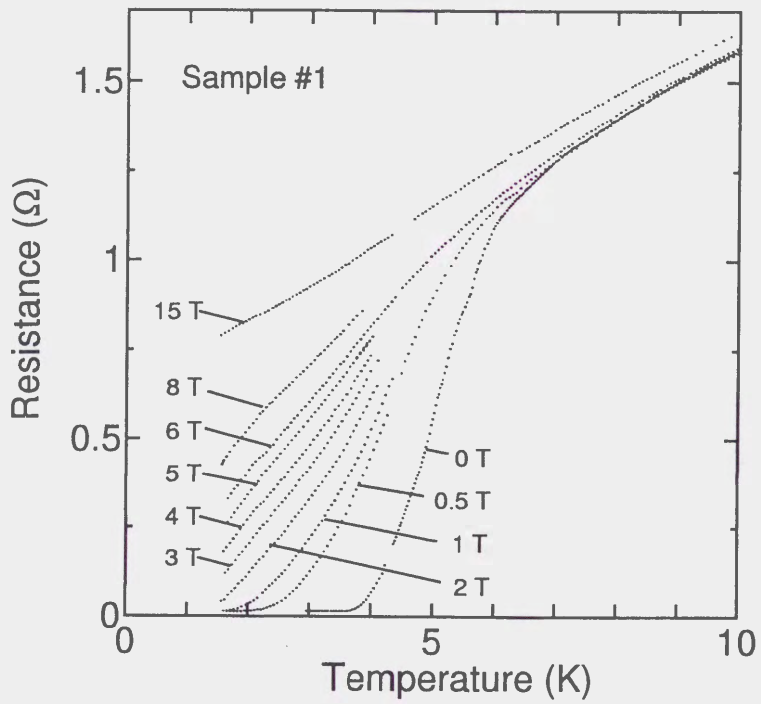
Figure 5.5: The temperature dependence of the in-plane resistance in the superconducting transition region for sample #1. The magnetic field up to 15 T was applied perpendicular to the conducting plane.

with use of a 27-T magnet at the High Magnetic Field Laboratory, Institute for Material Research at Tohuku University. Figure 5.6 shows one of the results exhibiting the angle dependence of the resistance in the magnetic field of 20 T and 24 T at 0.5 K. It showed a broad resistance dip centered at $\theta=90°$ even at 24 T, which was ascribable to superconductivity. The result demonstrates that the resistance drop at $\theta=90°$ under 20 T and 24 T was almost 50% and 10% of the value at $\theta=0°$, respectively.

The temperature dependence of H_{c2} under in-plane magnetic fields is summarized in Fig. 5.7. The H_{c2} values were evaluated in two ways: one is the value at the midpoint of the resistive transition and the other is the value at 90 % of the resistivity in the normal state. The results for the field parallel to the a axis are presented together with those for the field along the b axis. The H_{c2} evaluated at 0.5 K indicates a tendency of saturation rather than negative curvature.

5.1.3   Discussion

First, we compare the H_{c2} behavior with that of other organic superconductors. It is remarkable that the H_{c2} of κ-(BEDT-TTF)$_4$Hg$_{2.89}$Br$_8$ grew rapidly with decreasing temperature, but was strongly suppressed below 3 K, as shown in Fig 5.8. The initial slope $-d(\mu_0 H_{c2})/dT)_{T=T_c}$ of ~10 T/K is three times larger than that for the compounds with a similar T_c. This result indicates strong suppression of the orbital depairing effect in this compound. It is also interesting to note the correlation between T_c and the initial slope in these organic superconductors, irrespective of the type of the crystal structure: organic superconductors with higher T_c have a tendency to exhibit a larger value of the initial slope near T_c. The characteristics of the H_{c2} behavior are summarized in Table 5.2.

As demonstrated in Section 1.4, the effect of orbital motion is substan-
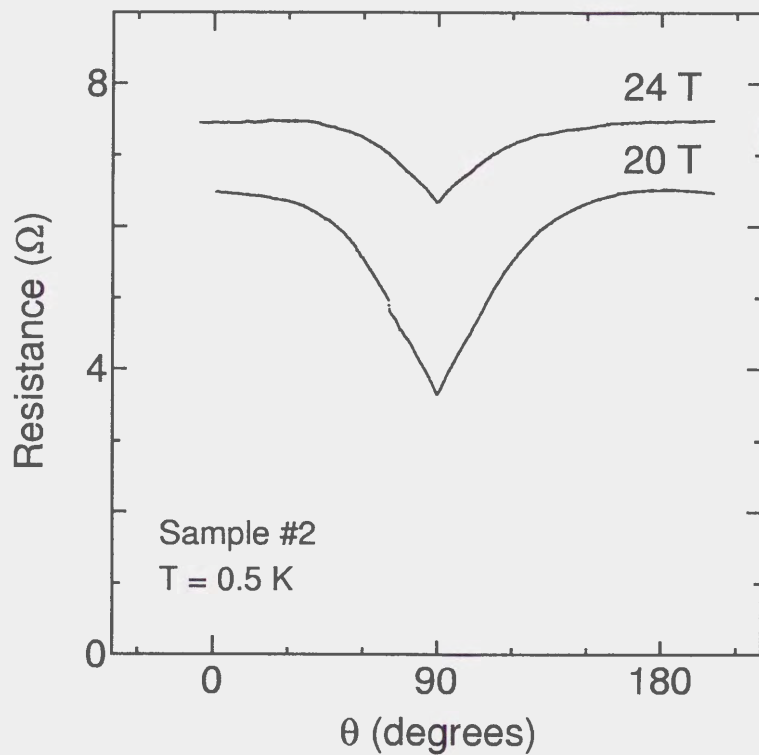
Figure 5.6: The angle dependence of the resistance under the magnetic field of 20 T and 24 T and at 0.5 K for sample #2.
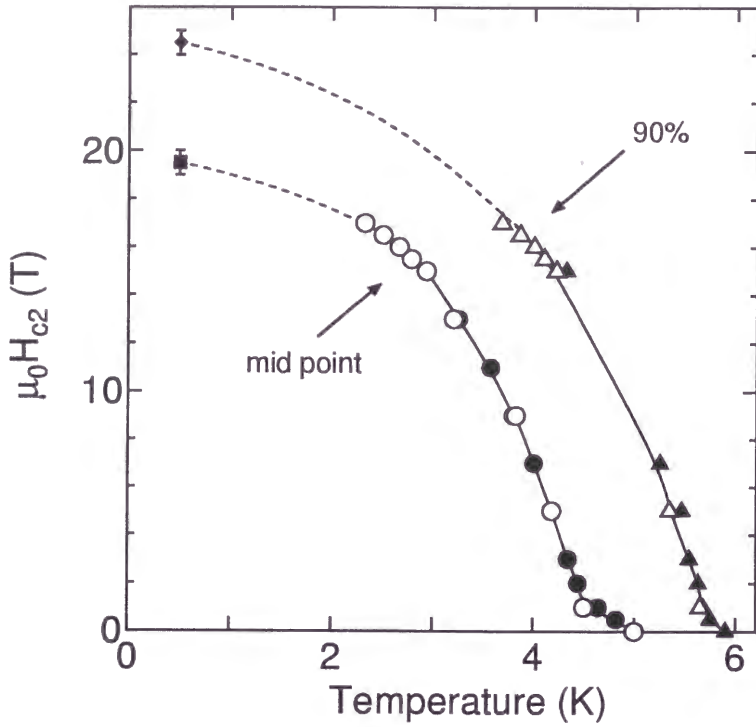
Figure 5.7: The temperature dependence of the H_{c2} determined at the mid-point of the resistive transition ($\bigcirc$ for sample #1 and $\square$ for #2) and that determined at the 10 % decrease ($\triangle$ for #1 and $\diamondsuit$ for #2) from the normal resistance under the in-plane magnetic field. The open marks denote the data obtained for the field along the a axis, while the closed marks denote those along the b axis.
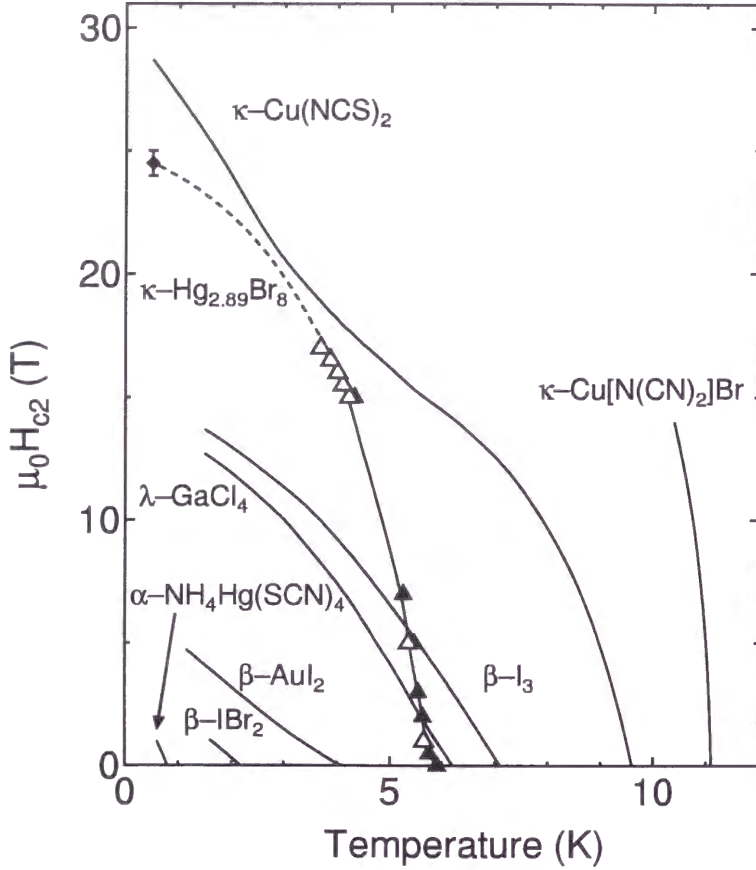
Figure 5.8: Curves of the temperature dependence of H_{c2} under in-plane magnetic fields for X-(BEDT-TTF)$_2Y$ salts (X-Y = κ-Cu[N(CN)$_2$]Br, κ-Cu(NCS)$_2$, α-NH$_4$Hg(SCN)$_4$, β-IBr$_2$, β-I$_3$, β-AuI$_2$) and λ-(BETS)$_2$GaCl$_4$ together with the present results shown in Fig. 5.7. Data are taken from Refs. [98]-[105].

	$-d(\mu_0 H_{c2})/dT$ (T/K)	$\mu_0 H_{c2}(0)$ (T)	T_c (K)
β-(ET)$_2$I$_3$ [98]	3.2	15	7.1
β-(ET)$_2$IBr$_2$ [99]	1.4	-	2.3
β-(ET)$_2$AuI$_2$ [100]	1.7	-	4.0
κ-(ET)$_4$Hg$_{2.89}$Br$_8$ [101]	10	24.5	5.8
κ-(ET)$_2$Cu(NCS)$_2$ [102]	8	30	9.5
κ-(ET)$_2$Cu[N(CN)$_2$]Br [103]	14	>14	11.0
α-(ET)$_2$NH$_4$Hg(SCN)$_4$ [104]	8	-	0.76
λ-(BETS)$_2$GaCl$_4$ [105]	3.6	13.5	6.0

Table 5.2: $H_{c2}(0)$ and $-d(\mu_0 H_{c2})/dT$ near T_c under in-plane magnetic fields for several types of organic superconductors.

tially reduced in this configuration and the effect of spin polarization works to determine the H_{c2} in the low temperature region. Then the results can be compared to a simple expression of $H_P(0)$ (H_P at zero temperature) based upon the weak-coupling BCS model, which is given by the following equation,

$$\mu_0 H_P(0) = 1.84 \ T_c, \tag{5.1}$$

where $\mu_0 H_P$ and T_c are given in a unit of Tesla and Kelvin, respectively. The evaluated $\mu_0 H_P$ becomes 9.2 T with $T_c = 5.0$ K determined at the midpoint of the resistive transition. The observed $\mu_0 H_{c2}$ of 19.5 T at 0.5 K as displayed in Fig. 5.7 indicates that $\mu_0 H_{c2}$ reaches 2.1 times of $\mu_0 H_P$. On the other hand, when we focus on the onset point, the observed value of $\mu_0 H_{c2}$=24.6 T is also 2.1 times of the evaluated $\mu_0 H_P = 11.4$ T with T_c=6 K.

To account for the enhancement of the observed H_{c2} over H_P, an appearance of the superconducting phase called the FFLO state has been considered in low-dimensional superconductors in the high field region close to H_{c2} [106, 107, 108]. In the FFLO state, Cooper pairs are formed between (k, ↑) and ($-k+q$, ↓) on FSs displaced by the Zeeman energy, with a spatially modulated order parameter $\Delta(r)$ being proportional to $\exp(iq \cdot r)$. In fact, an experimental data ascribable to such mechanism has been reported in κ-(BEDT-TTF)$_2$Cu(NCS)$_2$ [109] according to magnetization measurements. Anomalous behavior of κ-(BEDT-TTF)$_2$Cu(NCS)$_2$ shown in Fig 5.8 is also thought to be a result of the new superconducting state. In the present result of κ-(BEDT-TTF)$_4$Hg$_{2.89}$Br$_8$, however, H_{c2} did not show negative curvature down to 0.5 K, indicating the absence of the FFLO state.

As a possible reason, we can point out that the FFLO state expected for clean type-II superconductors is violated by defects or randomness. The present material is considered to contain randomness originating from the incommensurate Hg concentration and internal strain. This view seems to be supported by the absence of quantum oscillations in magnetic fields up to

27 T at 0.5 K. A possibility of a triplet superconductor is also unlikely due to a similar reason that unconventional superconductivity is dramatically suppressed by nonmagnetic impurities or disorders.

With respect to the estimation of H_P it is pointed out that eq. (5.1) is based upon the weak-coupling BCS model. Hence, H_P can be large in the BEDT-TTF salts for which the sign of strong coupling has been reported [110] according to scanning tunneling spectroscopy.

On the other hand, H_{c2} can be substantially enhanced by strong spin-orbit coupling [111]. In such situation, $H_{c2}(0)$ is replaced with the value multiplied by $0.602(\tau_{so}T_c)^{-1/2}$ where τ_{so} is the relaxation time of spin-orbit scattering. The effect of strong spin-orbit scattering was reported for the 2D superconductor $TaS_2(pyridine)_{1/2}$ [112] where the TaS_2 layer works as the superconducting plane and the pyridine layer serves as the insulating layer. Hence, Ta atoms efficiently behave as a spin-orbit scattering center. On the other hand, τ_{so} value is evaluated to be $\sim 1 \times 10^{-13}$ seconds in the present case. This value seems to be short to account for the observed H_{c2} since the π electrons serve the conduction stays in far position from Hg atoms, which can be a center of spin-orbit scattering, although the possibility cannot be ruled out. Therefore, more experiments are needed to establish a conclusive view on the enhancement of H_{c2} in κ-(BEDT-TTF)$_4$Hg$_{2.89}$Br$_8$.

5.2 Search for superconductivity recurrence in Sr_2RuO_4

5.2.1 Introduction

An increasing number of experiments have revealed that Sr_2RuO_4 is a p-wave superconductor with total spin moment of $S=1$, which has been theoretically proposed first by Rice and Sigrist [113]. Strong suppression of T_c by non-magnetic impurity of Aluminum [30, 38] has shown its unconventional superconductivity. Knight shift [36] is invariant both in the superconducting state and in the normal state, indicating triplet pairing of Cooper pairs. Moreover, broken time reversal symmetry of the superconducting gap [39] has been suggested by μSR experiments. Other experiments [114, 115] also appear to support triplet pairing of Sr_2RuO_4.

Recently, Lebed and Yamaji [8] have developed a theory for superconductivity recurrence under high magnetic fields applied parallel to the conducting plane especially for the p-wave superconductor Sr_2RuO_4 and much attention has been paid to this new superconducting state realized by the localization effect of Cooper pairs within the conducting sheet. On the other hand, to verify this prediction experimentally, it is found that very low temperatures and high magnetic fields are needed according to the theoretically proposed phase diagram. In addition, it is essential to align the magnetic field so that the perpendicular component of the field does not exceed the critical field of the superconductivity. For example, 0.1°-inclination of a field of 30 T off the conducting plane corresponds to perpendicular component of 0.05 T, which is comparable to the upper critical field of 0.075 T [116] for a field in the inter-plane direction. Therefore, precise control of the field orientation with an angle resolution of $\sim$0.01° in high magnetic fields is needed.

Bearing the above points in mind, we carried out resistance measurements

of the in-plane resistivity ρ_{ab} in magnetic fields up to 33 T at 50 mK at the National High Magnetic Field Laboratory (NHMFL), USA for the purpose of searching for the superconductivity recurrence in Sr_2RuO_4. From an experimental point of view, the search by measuring ρ_c seems to be technically easier, since the inter-plane resistance value is by one or two orders of magnitude larger than the in-plane resistance at low temperatures. However, we focused the search for superconductivity recurrence on ρ_{ab}, since the parallel-field-current configuration for the longitudinal ρ_{ab} measurements allowed us to exclude the additional dissipation due to the motion of Josephson-like vortices.

5.2.2 Results : study in high fields up to 33 T

The field dependence of ρ_{ab} in the field parallel to the [110] direction, $\rho_{ab}(H \parallel 110)$, of Sr_2RuO_4 at 50 mK is shown in Fig. 5.9. We obtained the result through setting the orientation by finding a dip under 1.5 T, as shown in Fig. 5.10, and then sweeping the field up to 33 T. The noise found in the low field region was due to the resistive magnet (note that ρ_{ab} was measured at the level of sub-$\mu\Omega$ and was hence more susceptible to noise than ρ_c). The magnetoresistance measured through the use of a superconducting magnet was superposed in Fig. 5.9, and this magnetoresistance was consistent with the results obtained from measurements with the resistive magnet. $\rho_{ab}(H \parallel 110)$ depended weakly on the field below 10 T, but it grew notably above 15 T without exhibiting saturation up to 33 T. It should be noted that the current direction in this case was almost parallel to the [110] direction, and hence the configuration was that for the longitudinal magnetoresistance.

Since an accidental inclination of the sample during the field sweep could not be ruled out, the sample was inclined by $\pm 10°$ in θ at 33 T as shown in the inset of Fig. 5.9 to examine whether a resistive decrease due to su-

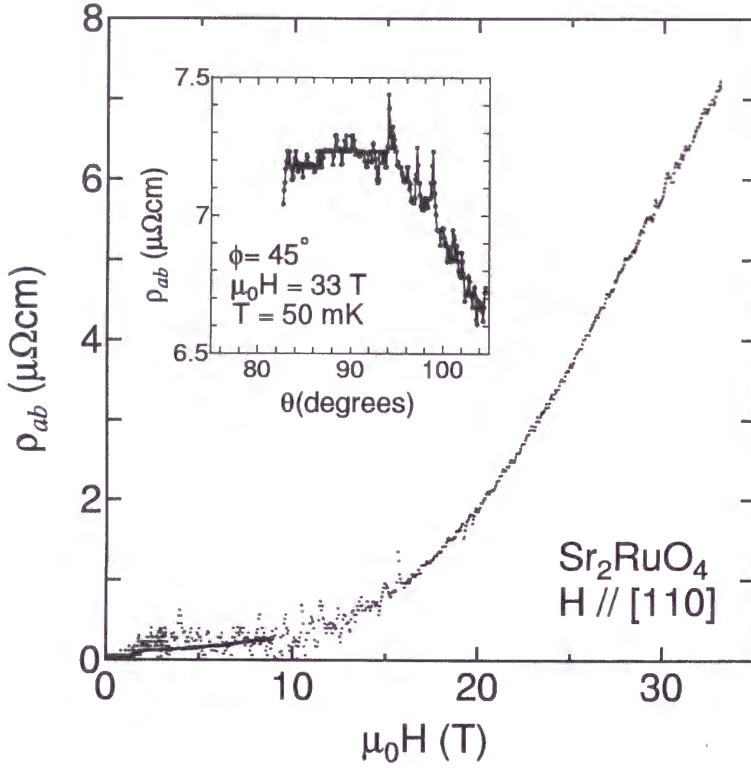Figure 5.9: Field dependence of ρ_{ab} of Sr_2RuO_4 at 50 mK for a magnetic field in the [110] direction. The data taken in a different run in a field up to 9 T with use of a superconducting magnet is also represented by the solid curve. The inset shows the polar-angle dependence of ρ_{ab} near the parallel field orientation for ϕ=45° at 33 T and 50 mK. The scattering of the data points represents the noise level.

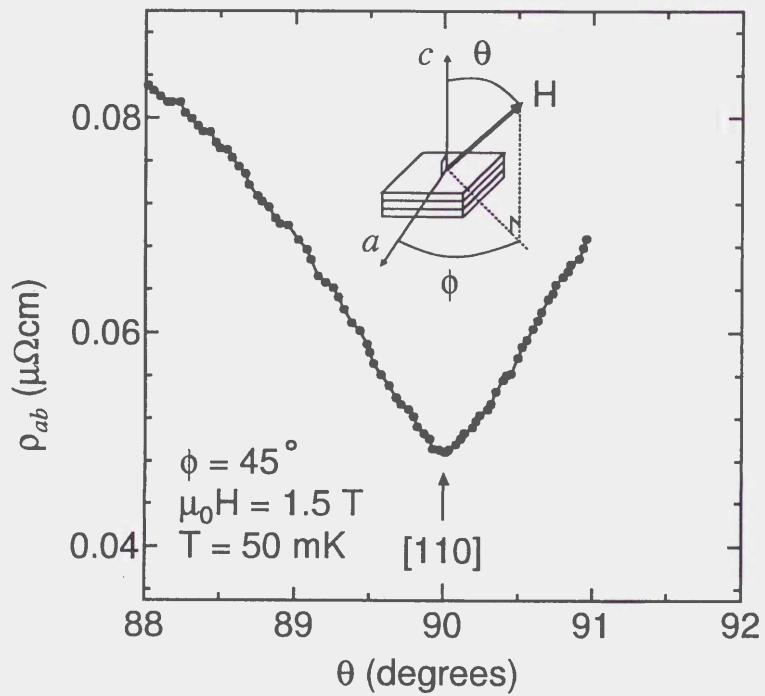Figure 5.10: Dip in ρ_{ab} of Sr_2RuO_4 at 50 mK under 1.5 T due to superconductivity by inclination of the field direction near the conducting plane. The field orientation is defined by the polar angle θ and the azimuthal angle ϕ as shown in the inset.
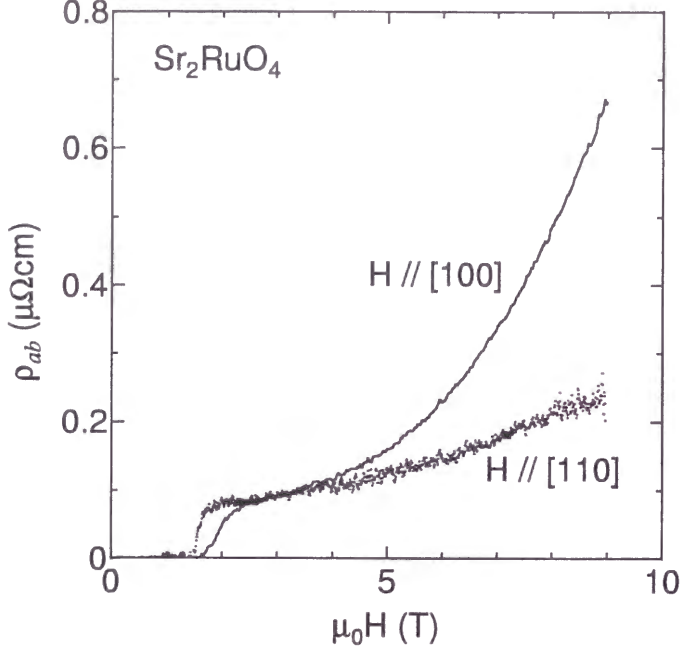
Figure 5.11: Field dependence of ρ_{ab} of Sr_2RuO_4 for magnetic fields in the [100] and [110] directions at 50 mK.

perconductivity recurrence could be found. The θ dependence of ρ_{ab} near the parallel field direction was found to be weak; the value remained almost unchanged within the inclination of $\pm 5°$ and no resistance drop was observed at $\theta = 90°$.

With regard to $\rho_{ab}(H \parallel 100)$, the measurement with the 33-T resistive magnet was not successful due to a poor signal-to-noise ratio, presumably due to the lead wire arrangement. We show the results up to 9 T in Fig. 5.11. $\rho_{ab}(H \parallel 100)$ started to increase more strongly at lower fields than $\rho_{ab}(H \parallel 110)$.

5.2.3   Discussion

Recently, superconductivity recurrence in high magnetic fields for Q2D superconductors has been theoretically proposed by Lebed and Yamaji [8]. Similar effects for Q1D and Q2D superconductors have been proposed by
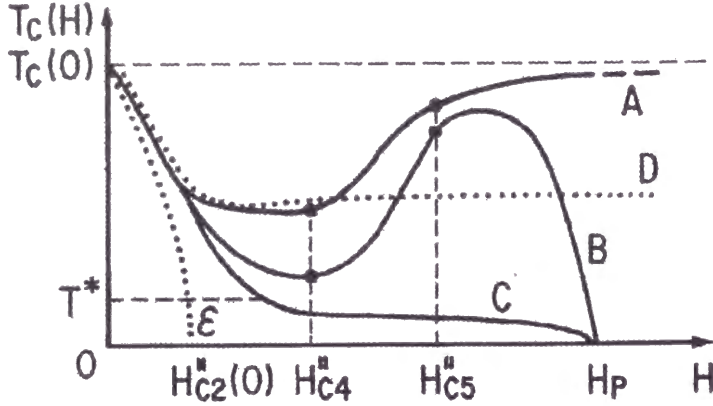
Figure 5.12: Possible magnetic field dependences of T_c proposed by Lebed *et al.* [8]. Curve A corresponds to the case of triplet pairing, while curves B and C correspond to the case of singlet pairing. Dotted curve D stands for the results of the Lawrence-Doniach model, whereas dotted curve E stands for the Ginzburg-Landau-Abrikosov-Gor'kov theory.

several authors [117, 118, 119, 120, 121]. Indeed, a trace ascribable to such a mechanism has been found in the Q1D organic superconductors, (TMTSF)X (X= ClO$_4$, PF$_6$) [122]. Lebed and Yamaji have extended their results for the Q1D case [117] to the Q2D case and have proposed a possible phase diagram for both singlet and triplet superconductors under magnetic fields applied parallel to the conducting plane, as shown in Fig. 5.12. For the triplet case, H_{c2} increases upon cooling, followed by a slope change in dH_{c2}/dT at a certain temperature T^*. In higher magnetic fields, T_c starts to increase again with sign change in dH_{c2}/dT, and the initial T_c may be restored in the high field limit due to the absence of a paramagnetic effect. For the singlet case, similar enhancement of H_{c2} is also expected although whether or not a sign change in dH_{c2}/dT occurs depends on parameters such as $t_\perp$. Distinct difference between the singlet and triplet cases is the existence of the Pauli limit H_P : T_c must be zero at $H=H_P$ for the singlet case in contrast to the triplet case. Therefore, triplet superconductors are more favorable to the observation.

114

Such recurrence is induced by quantum effects on Cooper pairs, which has not been taken in the quasiclassical approach of H_{c2} so far. As a result of shrinkage of orbital motion under in-plane magnetic fields, electron wave functions are localized within the 2D plane in high magnetic fields. Therefore, diamagnetic currents no longer destroy two-dimensionalized Cooper pair.

For Sr_2RuO_4, the absence of the paramagnetc effect in magnetic fields applied parallel to the conducting plane has been shown by the invariance of Knight shift [36]. Hence, superconductivity can recur in high magnetic fields even if the superconductivity is destroyed by quasiclassical H_{c2}. The critical field H_c^* corresponding to the superconductivity recurrence is analytically given by

$$H_c^* = \begin{cases} 8.0\xi_\perp^2(0)H_{c2}^\parallel(0)/d^2, & \xi_\perp(0) \gg d, \\ 3.2\xi_\perp(0)H_{c2}^\parallel(0)/d, & \xi_\perp(0) \ll d, \end{cases} \tag{5.2}$$

where $\xi_\perp(0)$ is the inter-plane coherence length at zero temperature and $H_{c2}^\parallel(0)$ is the quasiclassical upper critical field along the conducting plane at zero temperature. For Sr_2RuO_4, $\xi_\perp(0)$ and $\mu_0 H_{c2}^\parallel(0)$ were evaluated to be $\simeq 3.3$ nm and $\simeq 1.5$ T, respectively [116]. With more realistic calculation for a certain $\xi_c(0)/d$ value, the $\mu_0 H_c^*$ value is estimated to be 30-140 T [123] depending on band parameters such as $t_\perp$ and hence the relevance of the superconductivity to the α, β, and γ branches.

Agterberg et $al.$ have recently proposed a possible mechanism for the superconductivity of Sr_2RuO_4 based upon orbital-dependent superconductivity [124]. According to them, the superconducting properties are explained principally by the γ branch on which 60% of the density of states resides. This hypothesis seems to be partly supported by the measurement of the specific heat [115] and the penetration depth [125]. Provided that this scenario is correct, the pairing interaction is stronger for quasiparticles on the γ branch, and the superconductivity in high magnetic fields should be controlled by the γ branch as well.

The measured $\rho_{ab}(H \parallel 110)$ indicates that the superconductivity recurrence is absent at least up to 33 T at 50 mK. Note that the quality of the sample was high, as evidenced by a T_c of 1.41 K and the residual resistance ratio $\rho_{300K}/\rho_{1.5K}$ reaching $\sim 10^3$. These results imply that the critical field for the recurrence, if it exists, should be higher than 33 T.

For further attempts in the future, higher magnetic fields such as a 45-T resistive magnet which is now under construction and will be useful in the near future at NHMFL are desired. Measurements with use of a pulse magnet is also worthwhile. Concerning measuring methods, resistivity measurements are not enough since a certain change in the resistivity cannot be directly connected to superconducting signals, and therefore, measurements of thermodynamic properties are needed together. For example, magnetization measurements with a torquemeter, whose signal-to-noise ratio is much better than the resistivity measurements, are useful: the angle-dependent torque, if the recurrence occurs, will exhibit a kink due to superconductivity in the direction parallel to the conducting plane. Besides, an inductive method used for usual magnetization measurements is also considered to be useful.

Chapter 6

Summary

In this thesis, the experimental results on the phenomena induced by oriented magnetic fields have been presented. High quality samples enabled us to study these effects in the normal and superconducting states of Q2D superconductors.

In Chapter 4, the normal state of Q2D superconductors have been studied through the measurements of angle-dependent galvanomagnetic effects and quantum oscillations, paying attention to the interplay between the cylindrical FS and magnetic fields.

In Section 4.1 and 4.3, the results of AMRO and a resistance peak in Sr_2RuO_4 were presented as the first example of these effects in oxide superconductors. Since the normal state properties of Sr_2RuO_4 had been extensively studied, more detailed analysis was possible compared to organic superconductors. According to the AMRO results yielding the in-plane energy dispersion, we have shown that the observed FS contour is rather consistent with the calculated one, although ambiguity of the assignment is left. At present stage, it seems to be more likely that the β branch dominates the AMRO behavior, taking into account of the contribution of each FS branch to the inter-plane conductivity. On the other hand, the resistance peak at $\theta=90°$ yielding the inter-plane dispersion showed notable dependence on the in-plane direction, incompatible with that expected for a simple energy dis-

persion. This indicates that the anisotropy in $t_\perp$ should be taken into account in the analysis of experiments. In fact, the observed behavior of the inter-plane transverse magnetoresistance, showing different power low dependence between at and outside the resistance peak, cannot be explained by a simple FS model at all. We pointed out the essential role of the anisotropy in $t_\perp$ for the behavior. Through the results of these measurements, more significant role of the in-plane anisotropy in Sr_2RuO_4 has been revealed than in organic superconductors.

In Section 4.2, we have revealed the close relevance between the dimensionality of the system and the oscillatory behavior of the quantum oscillations. The observed sum and difference frequencies of the α and β branches were enhanced at the so-called Yamaji angle, where the system can be regarded as pure 2D. We have shown that the coincidence of the Yamaji angle for the α and β branches is essential for the observation, and pointed out that the theoretical assumption of constant chemical potential is not satisfied at such angles and that theoretically strict treatment of the system with constant electron number should be taken. The sum and difference frequencies are well explained as a result of carrier exchange between relevant two bands, leading to modulation of the density of states. The independent three FS branches, very similar to theoretical models, enabled us to come to this clear interpretation, compared to the case for organic superconductor forming a magnetic breakdown system in the high field region.

In Section 4.4, we have shown the existence of a small 3D FS in the Q2D organic superconductor κ-$(BEDT\text{-}TTF)_2Cu_2(CN)_3$, through the measurements of angle dependence of the quantum oscillations. The sensitivity of the FS cross-sectional area to pressure is distinct from the observed FS consistent with the band calculation, indicating the different origin of the FSs. Based upon the structural consideration, we pointed out that the small

118

FS originates from the interaction between BEDT-TTF molecules and the anion layers, which has been neglected in the conventional band calculation. The strong pressure dependence can be understood by dramatic enhancement of the inter-plane transfer due to the reduction of the layer spacing by pressure.

In Chapter 5, the superconducting state of Q2D superconductors have been studied through the resistance measurements in magnetic fields applied parallel to the conducting plane, paying attention to the suppression of the orbital depairing effect.

In Section 5.1, we have presented the H_{c2} results in the organic superconductor κ-(BEDT-TTF)$_4$Hg$_{2.89}$Br$_8$, obtained by the resistance measurements down to 0.5 K. Compared to other organic superconductors with a similar T_c, the initial slope of the H_{c2} curve near T_c was by a factor of 3 greater, indicating that the orbital depairing effect is strongly suppressed in this field configuration. We have shown that H_{c2} of κ-(BEDT-TTF)$_4$Hg$_{2.89}$Br$_8$ is by a factor of almost 2 greater than H_P along the conducting plane, expected for a weak-coupling BCS model, although a slope change in the high field region, ascribable to new superconducting states such as the FFLO state, was not detected. As one of the reasons for the absence, the inhomogeniety or internal strain inherent to the incommensurate crystal structure is pointed out. The origin of the enhancement of H_{c2} may be ascribed to strong-coupling superconductor or large spin-orbit coupling but further experimental study is needed to obtain a conclusive view.

In Section 5.2, we have presented the experimental results of the search for superconductivity recurrence, which have been proposed for the p-wave superconductor Sr$_2$RuO$_4$ in strong magnetic fields along the conducting plane. We carried out measurements of the in-plane resistivity by controlling the field orientation with angle resolution of 0.01°. However, we could not find

any trace of the superconductivity recurrence as far as the measurements were carried out in the magnetic field reaching 33 T and at 50 mK. Since the superconductivity recurrence depends on band parameters such as $t_\perp$, the required field for the observation can be higher than 33 T. It is worthwhile to carry out experiments in higher magnetic fields using a pulsed magnet. It should be also noted that the in-plane resistivity exhibited huge longitudinal magnetoresistance reaching $\Delta\rho_{ab}/\rho_{ab0} \sim 70$ at 33 T, even though the filed was applied almost parallel to the current. The origin should be clarified in the future.

Chapter 7

Acknowledgements

Bibliography

[1] For a text, see *e.g.* J. M. Ziman, *Principles of the Theory of Solids, 2nd ed.* (Cambridge University Press, Cambridge, 1972).

[2] B. S. Chandrasekhar, Appl. Phys. Lett. **1**, 7 (1962).

[3] A. M. Clogston, Phys. Rev. Lett. **9**, 199 (1962).

[4] M. V. Kartsovnik, P. A. Kononovich, V. N. Laukhin, and I. F. Schegolev, JETP Lett. **48**, 541 (1988).

[5] K. Kajita, Y. Nishio, T. Takahashi, W. Sasaki, R. Kato, H. Kobayashi, A. Kobayashi, and Y. Iye, Solid State Commun. **70**, 1189 (1989).

[6] P. Fulde and R. A. Ferrell, Phys. Rev. **135**, A550 (1964).

[7] A. I. Larkin and Yu. N. Ovchinikov, JETP **20**, 762 (1965).

[8] A. G. Lebed and K. Yamaji, Phys. Rev. Lett. **80**, 2697 (1998).

[9] For a text, T. Ishiguro, K. Yamaji, and G. Saito, *Organic Superconductors, 2nd ed.* (Springer-Verlag, Berlin, 1998).

[10] For a text, see *e.g.* J. M. Williams, J. R. Ferraro, R. J. Thorn, K. D. Carlson, U. Geiser, H. H. Wang, A. M. Kini, and M. -H. Whangbo, *Organic Superconductors (Including Fullerens)-Synthesis Structure, Properties, and Theory* (Prentice Hall, Englewood Cliffs, 1992).

[11] U. Geiser, H. H. Wang, K. D. Carlson, J. M. Williams, H. A. Charlier Jr., J. E. Heindl, G. A. Yaconi, B. H. Love, M. W. Lathrop, J. E. Schirber, D. L. Overmyer, J. Ren, and M. -H. Whangbo, Inorg. Chem. **30**, 2586 (1991).

[12] T. Komatsu, T. Nakamura, N. Matsukawa, H. Yamochi, G. Saito, H. Ito, T. Ishiguro, M. Kusunoki, and K. Sakaguchi, Solid State Commun. **80**, 843 (1991).

[13] H. Urayama, H. Yamochi, G. Saito, K. Nozawa, T. Sugano, M. Kinoshita, S. Saito, K. Ohshima, A. Kawamoto, and J. Tanaka, Chem. Lett. **1988**, 55 (1988).

[14] R. N. Lyubovskaya, E. A. Zhilyaeva, A. V. Zvarykina, V. N. Laukhin, R. B. Lyubovskii, and S. I. Pesotskii, JETP Lett. **45**, 530 (1987).

[15] H. Urayama, H. Yamochi, G. Saito, S. Sato, A. Kawamoto, J. Tanaka, T. Mori, Y. Maruyama, and H. Inokuchi, Chem Lett. **1988**, 463 (1988).

[16] R. N. Lyubovskaya, E. A. Zhilyaeva, S. I. Pesotskii, R. B. Lyubovskii, L. O. Atovmyan, O. A. D'yachenko, and T. G. Takhirov, JETP Lett. **46**, 188 (1987).

[17] For a review, J. Wosnitza, *Fermi surfaces of Low-Dimensional Organic Metals and Superconductors* (Springer-Verlag, Berlin, 1996).

[18] T. Komatsu, N. Matsukawa, T. Inoue, and G. Saito, J. Phys. Soc. Jpn. **65**, 1340 (1996).

[19] K. Ohshima, T. Mori, H. Inokuchi, H. Urayama, H. Yamochi, and G. Saito, Phys. Rev. B **38**, 938 (1988).

[20] M. -H. Whangbo, J. J. Novoa, D. Jung, J. M. Williams, A. M. Kini, H. H. Wang, U. Geiser, M. A. Beno, and K. D. Carlson, in *Organic Superconductivity*, ed. V. Z. Kresin and W. A. Little (Plenum, New York, 1990), p243.

[21] K. Ohshima, H. Urayama, H. Yamochi, and G, Saito, Physica C **153-155**, 1148 (1988).

[22] H. Urayama, H. Yamochi, G. Saito, S. Sato, T. Sugano, M. Kinoshita, A. Kawamoto, J. Tanaka, T. Inabe, T. Mori, Y. Maruyama, H. Inokuchi, and K. Oshima, Synth. Met. **27**, A393 (1988).

[23] J. E. Shirber, D. L. Overmyer, E. I. Venturini, H. H. Wang, K. D. Carlson, W. K. Kwok, S. Kleinjan, and J. M. Williams, Physica C **161**, 412 (1989).

[24] K. Murata, Y. Honda, H. Anzai, M. Tokumoto, K. Takahashi, N. Kinoshita, and T. Ishiguro, Synth. Met. **27**, A263 (1989).

[25] J. E. Shirber, E. L. Venturini, A. M. Kini, H. H. Wang, J. R. Whiworth, and J. M. Williams, Physica C **152**, 157 (1988).

[26] Y. Maeno, H. Hashimoto, K. Yoshida, S. Nishizaki, T. Fujita, J. G. Bednorz, and F. Lichtenberg, Nature (London) **372**, 532 (1994).

[27] M. Braden, A. H. Moudden, S. Nishizaki, Y. Maeno, and T. Fujita, Physica C **273**, 248 (1997).

[28] T. Oguchi, Phys. Rev. B **51**, 1385 (1995).

[29] D. J. Singh, Phys. Rev. B **52**, 1358 (1995).

[30] A. P. Mackenzie, S. R. Julian, A. J. Diver, G. J. McMullan, M. P. Ray, G. G. Lonzarich, Y. Maeno, S. Nishizaki, and T. Fujita, Phys. Rev. Lett. **76**, 3786 (1996).

[31] Y. Yoshida, R. Settai, Y. Ōnuki, H. Takei, K. Betsuyaku, and H. Harima, J. Phys. Soc. Jpn. **67**, 1677 (1998).

[32] E. Ohmichi, Y. Maeno, and T. Ishiguro, J. Phys. Soc. Jpn. **68**, 24 (1999).

[33] S. Nakatsuji, S. Ikeda, and Y. Maeno, J. Phys. Soc. Jpn. **66**, 1868 (1997).

[34] G. Cao, S. McCall, M. Shepard, J. E. Crow, and R. P. Guertin, Phys. Rev. B **56**, R2916 (1997).

[35] Y. Maeno, K. Yoshida, H. Hashimoto, S. Nishizaki, S. Ikeda, M. Nohara, T. Fujita, A. P. Mackenzie, N. E. Hussey, J. G. Bednorz, and F. Lichtenberg, J. Phys. Soc. Jpn. **66**, 1405 (1997).

[36] K. Ishida, H. Mukuda, Y. Kitaoka, K. Asayama, Z. Q. Mao, Y. Mori, and Y. Maeno, Nature (London) **396**, 658 (1998).

[37] A. P. Mackenzie, R. K. W. Haselwimmer, A. W. Tyler, G. G. Lonzarich, Y. Mori, S. Nishizaki, and Y. Maeno, Phys. Rev. Lett. **80**, 161 (1998).

[38] Z. Q. Mao, Y. Mori, and Y. Maeno, Phys. Rev. B **60**, 610 (1999).

[39] G. M. Luke, Y. Fudamoto, K. M. Kojima, M. I. Larkin, J. Merrin, B. Nachumi, Y. J. Uemura, Y. Maeno, Z. Q. Mao, Y. Mori, H. Nakamura, and M. Sigrist, Nature (London) **394**, 558 (1998).

[40] K. Yamaji, J. Phys. Soc. Jpn. **58**, 1520 (1989).

[41] R. Yagi, Y. Iye, T. Osada, and S. Kagoshima, J. Phys. Soc. Jpn. **59**, 3069 (1990).

[42] For a text, see *e.g.* D. Shoenberg, *Magnetic Oscillations in Metals* (Cambridge University Press, Cambridge, 1984).

[43] L. Onsager, Phil. Mag. **43**, 1006 (1952).

[44] L. Landau, Z. Phys. **64**, 629 (1930).

[45] L. F. Lifshitz and A. M. Kosevich, Pis'ma Zh. Eksp. Fiz. **29**, 730 (1955).

[46] R. B. Dingle, Proc. Roy. Soc. **A211**, 517 (1952).

[47] R. N. Lyubovskaya, M. Z. Aldoshina, L. M. Goldenberg, and E. A. Zhilyaeva, Synth. Met. **41-43**, 2143 (1991).

[48] R. Settai, M. Chida, S. Yanagiba, and T. Goto, Jpn. J. Appl. Phys. **31**, 3736 (1992).

[49] M. V. Kartsovnik, P. A. Kononovich, V. N. Laukhin, S. I. Pesotskii, and I. F. Schegolev, JETP **70** 735 (1990).

[50] N. Shirakawa, K. Murata, Y. Nishihara, S. Nishizaki, Y. Maeno, T. Fujita, J. G. Bednorz, F. Lichtenberg, and N. Hamada, J. Phys. Soc. Jpn. **64**, 1072 (1995).

[51] A. P. Mackenzie, N. E. Hussey, A. J. Diver, S. R. Julian, Y. Maeno, S. Nishizaki, and T. Fujita, Phys. Rev. B **54**, 7425 (1996).

[52] A. P. Mackenzie, S. R. Julian, A. J. Diver, G. G. Lonzarich, N. E. Hussey, Y. Maeno, S. Nishizaki, and T. Fujita, Physica C **263**, 510 (1996).

[53] T. Yokoya, A. Chainani, T. Takahashi, H. Katayama-Yoshida, M. Kasai, and Y. Tokura, Phys. Rev. Lett. **76**, 3009 (1996).

[54] D. H. Lu, M. Schmidt, T. R. Cummins, S. Schuppler, F. Lichtenberg, and J. G. Bednorz, Phys. Rev. Lett. **76**, 4845 (1996).

[55] T. Yokoya, A. Chainani, T. Takahashi, H. Ding, J. C. Campuzano, H. Katayama-Yoshida, M. Kasai, and Y. Tokura, Phys. Rev. B **54**, 13311 (1996).

[56] A. P. Mackenzie, S. Ikeda, Y. Maeno, T. Fujita, S. R. Julian, and G. G. Lonzarich, J. Phys. Soc. Jpn. **67**, 385 (1998).

[57] M. V. Kartsovnik, V. N. Laukhin, S. I. Pesotskii, I. F. Schegolev, and V. M. Yakovenko, J. Phys. I **2**, 89 (1991).

[58] T. Oguchi (unpublished).

[59] F. Ishii and T. Oguchi, in Proceedings of the LI-st Yamada Conference on Strongly Correlated Electron Systems (SCES99), Nagano, August, 1999 (unpublished).

[60] E. Ohmichi, H. Adachi, Y. Mori, Y. Maeno, T. Ishiguro, and T. Oguchi, Phys. Rev. B **59**, 7263 (1999).

[61] C. Bergemann, S. R. Julian, A. P. Mackenzie, S. Nishizaki, and Y. Maeno, cond-mat/9909027 (To appear in Phys. Rev. Lett. **84**).

[62] Y. Yoshida, A. Mukai, R. Settai, Y. Ōnuki and H. Takei, J. Phys. Soc. Jpn. **67**, 2551 (1998).

[63] A. S. Alexandrov and A. M. Bratkovsky, Phys. Rev. Lett. **76**, 1308 (1996).

[64] M. Nakano, J. Phys. Soc. Jpn. **66**, 19 (1997).

[65] L. M. Falicov and H. Stachowiak, Phys. Rev. **147**, 505 (1966).

[66] K. Yoshida, Y. Maeno, S. Nishizaki, S. Ikeda and T. Fujita, J. Low Temp. Phys. **105**, 1593 (1996).

[67] M. Nakano, J. Phys. Soc. Jpn **68**, 1801 (1999).

[68] F. A. Meyer, E. Steep, W. Biberacher, P. Christ, A. Lerf, A. G. M. Jansen, W. Joss, P. Wyder, and K. Andres, Europhys. Lett. **32**, 681 (1995).

[69] S. Uji, M. Chaparala, S. Hill, P. S. Sandhu, J. Qualls, L. Seger, and J. S. Brooks, Synth. Met. **85**, 1573 (1997).

[70] T. Sasaki, H. Sato, and N. Toyota, Solid State Commun. **76**, 507 (1990).

[71] J. Caulfield, J. Singleton, F. L. Pratt, M. Doporto, W. Lubczynski, W. Hayes, M. Kurmoo, P. Day, P. T. J. Hendriks, and J. A. A. J. Perenboom, Synth. Met. **61**, 63 (1993).

[72] N. Harrison, J. Caulfield, J. Singleton, P. H. P. Reinders, F. Herlach, W. Hayes, M. Kurmoo, and P. Day, J. Phys. **8**, 5415 (1996).

[73] M. M. Honold, N. Harrison, M. -S. Nam, J. Singleton, C. H. Mielke, M. Kurmoo, and P. Day, Phys. Rev. B **58**, 7560 (1998).

[74] R. W. Stark and R. Reifenberger, J. Low Temp. Phys. **26**, 763 (1977).

[75] K. Machida, K. Kishigi, and Y. Hori, Phys. Rev. B **51**, 8946 (1995).

[76] K. Kishigi, M. Nakano, K. Machida, and Y. Hori, J. Phys. Soc. Jpn. **64**, 3043 (1995).

[77] P. S. Sandhu, Ju H. Kim, and J. S. Brooks, Phys. Rev. B **56**, 11566 (1997).

[78] S. -Y. Han, Ju H. Kim, J. S. Brooks, and P. S. Sandhu, Synth. Met. **103**, 2084 (1999).

[79] E. Ohmichi, H. Ito, T. Ishiguro, T. Komatsu, and G. Saito, J. Phys. Soc. Jpn. **66**, 310 (1997).

[80] N. Hanasaki, S. Kagoshima, T. Hasegawa, T. Osada, and N. Miura, Phys. Rev. B **57**, 1336 (1998).

[81] D. G. Clarke and S. P. Strong, Adv. Phys. **46**, 545 (1997).

[82] T. Nakada, T. Ishiguro, T. Miura, Y. Misaki, T. Yamabe, and T. Mori, J. Phys. Soc. Jpn. **67**, 355 (1998).

[83] S. Hill, Phys. Rev. B **55**, 4931 (1997).

[84] A. G. Lebed and N. N. Bagmet, Phys. Rev. B **55**, R8654 (1997).

[85] V. G. Peschansky, JETP **85**, 337 (1997).
V. G. Peschansky, Sov. J. Low Temp. Phys. **23**, 35 (1997).

[86] A. J. Schofield, J. R. Cooper, and J. M. Wheatley, cond-mat/9709167.

[87] P. Moses and R. H. McKenzie, Phys. Rev. B **60**, 7998 (1999).

[88] V. G. Peschansky and M. V. Kartsovnik, Phys. Rev. B **60**, 11207 (1999).

[89] E. Ohmichi, H. Ito, T. Ishiguro, G. Saito, and T. Komatsu, Phys. Rev. B **57**, 7481 (1998).

[90] T. Terashima, S. Uji, H. Aoki, M. Tamura, M. Kinoshita and M. Tokumoto, Solid State Commun. **91**, 595 (1994).

[91] A. J. Schultz, H. H. Wang, J. M. Williams, L. W. Finger, R. M. Hazen, C. Rovira, and M.-H. Whangbo, Physica C **234**, 300 (1994).

[92] D. Chasseau, J. Gaultier, M. Rahal, L. Ducasse, M. kurmoo, and P. Day, Synth. Met. **41-43** 2039 (1991).

[93] T. Komatsu (unpublished).

[94] R. N. Lyubovskaya, R. B. Lyubovskii, M. K. Makova, and S. I. Pesotskii, JETP Lett. **51**, 361 (1990).

[95] S. Wanka, D. Beckmann, J. Wosnitza, E. Balthes, D. Schweitzer, W. Strunz, and H. J. Keller, Phys. Rev. B **53**, 9301 (1996).

[96] H. Ito, Y. Nogami, T. Ishiguro, T. Komatsu, G. Saito, and N. Hosoito, Jpn. J. Appl. Phys. **7**, 419 (1992).

[97] R. B. Lyubovskii, R. N. Lyubovskaya, and O. A. D'yachenko, J. Phys. I **6**, 1609 (1996).

[98] V. N. Laukhin, S. I. Pesotskii, and E. B. Yagbuskii, JETP Lett. **45**, 501 (1987).

[99] M. Tokumoto, H. Anzai, H. Bando, G. Saito, N. Kinoshita, K. Kajimura, and T. Ishiguro, J. Phys. Soc. Jpn. **54**, 1669 (1985).

[100] H. Schwenk, S. S. P. Parkin, V. Y. Lee, and R. L. Greene, Phys. Rev. B **34**, 3156 (1986).

[101] E. Ohmichi, T. Ishiguro, T. Sakon, T. Sasaki, M. Motokawa, R. B. Lyubovskii, and R. N. Lyubovskaya, J. Supercond. **12**, 505 (1999).

[102] M. -S. Nam, J. A. Symington, J. Singleton, S. J. Blundell, A. Ardavan, M. Kurmoo, and P. Day, J. Phys. **11**, L477 (1999).

[103] A. Kovalev (Specific heat data, unpublished).

[104] A. Kovalev (Specific heat data, unpublished).

[105] M. A. Tanatar, T. Ishiguro, H. Tanaka, A. Kobayashi, and H. Kobayashi, J. Supercond. **12**, 511 (1999).

[106] H. Shimahara, J. Phys. Soc. Jpn. **66**, 541 (1997).

[107] H. Shimahara and D. Rainer, J. Phys. Soc. Jpn. **66**, 3591 (1997).

[108] H. Shimahara, J. Phys. Soc. Jpn. **68**, 3069 (1999).

[109] J. A. Symington, J. Singleton, M. -S. Nam, A. Ardavan, W. Hayes, M. Kurmoo, and P. Day, a preprint.

[110] M.E. Howley, K.E Gray, B. D. Terris, H. H. Wang, K. D. Karlson, and J. M. Williams, Phys. Rev. Lett. **57**, 629 (1986).

[111] R. A. Klemm, A. Luther, and M. R. Beasley, Phys. Rev. B **12**, 877 (1975).

[112] D. E. Prober, R. E. Schwall, and M. R. Beasley, Phys. Rev. B **21**, 2717 (1980).

[113] T. M. Rice and M. Sigrist, J. Phys. **7**, L643 (1995).

[114] R. Jin, Yu. Zadorozhny, Y. Liu, D. G. Schlom, Y. Mori, and Y. Maeno, Phys. Rev. B **59**, 4433 (1999).

[115] S. Nishizaki, Y. Maeno, and Z. Q. Mao, in Proceedings of the International Conference on Physics and Chemistry of Molecular and Oxide Superconductors (MOS99), Stockholm, July 1999 (unpublished).

[116] T. Akima, S. Nishizaki, and Y. Maeno, J. Phys. Soc. Jpn. **68**, 694 (1999).

[117] A. G. Lebed, JETP Lett. **44**, 114 (1986).

[118] L. I. Burlachkov, L. P. Gor'kov, and A. G. Lebed, Europhys. Lett. **4**, 941 (1987).

[119] N. Dupuis, G. Montambaux, and C. A. R. Sa de Melo, Phys. Rev. Lett. **70**, 2613 (1993).

N. Dupuis and G. Montambaux, Phys. Rev. B **49**, 8993 (1994).

C. A. R. Sa de Melo, Physica C **260**, 224 (1996).

[120] Y. Hasegawa and M. Mayazaki, J. Phys. Soc. Jpn **65**, 1028 (1996).

M. Miyazaki and Y. Hasegawa, J. Phys. Soc. Jpn **65**, 3283 (1996).

[121] M. Miyazaki, K. Kishigi, and Y. Hasegawa, J. Phys. Soc. Jpn. **68**, 2344 (1999).

[122] I. J. Lee, M. J. Naughton, G. M. Danner, and P. M. Chaikin, Phys. Rev. Lett. 78, 3555 (1997).

M. J. Naughton, I. J. Lee, G. M. Danner, and P. M. Chaikin, Synth. Met. **85**, 1481 (1997).

I. J. Lee, A. P. Hope, M. J. Leone, and M. J. Naughton, Synth. Met. **70**, 747 (1995).

[123] A. G. Lebed (unpublished).

[124] D. F. Agterberg, T. M. Rice, and M. Sigrist, Phys. Rev. Lett. **78**, 3374 (1997).

[125] E. M. Forgan, A. P. Mackenzie, and Y. Maeno, in Proceedings of the International Conference on Physics and Chemistry of Molecular and Oxide Superconductors (MOS99), Stockholm, July 1999 (unpublished).